Imperial College of Science, Technology and Medicine
Department of Physics

Experiments with LISA Pathfinder: Cosmic Rays and Fundamental Physics

Jonathon Baird

Thesis submitted for the Degree of Doctor of Philosophy to
Imperial College London
March 2018

Acknowledgements

I would like to first acknowledge and thank my supervisor Tim. I have loved every moment of this PhD and cannot express enough how thankful I am to have had this opportunity. I would also like to thank the postdocs I worked with here at Imperial, Daniel and Peter. Without your patience, understanding and immense knowledge of the experiment this PhD would not have been possible. In addition, I would like to thank the LISA Pathfinder collaboration for all the help and experiences in the last three and a half years.

Working across several disciplines has meant I have had the opportunity to talk with academics from several fields, which has been invaluable in the shaping of this thesis. I hope I have done these topics some justice, and thank you for all your help.

The postgrads in the HEP, Astro and Theory groups here at Imperial have provided a constant source of support that has made the difficult times less daunting. Thanks in particular to the Lux-Zeplin group across the hall for putting up with me when I needed a break.

Finally, thank you to my family and partner for being so supportive. You helped me through in so many ways and I cannot thank you enough.

Declaration and Copyright

This thesis is my own work, except where explicitly indicated in the text.

Abstract

The Laser Interferometer Space Antenna (LISA) Pathfinder experiment successfully demonstrated that a future gravitational wave detector in space is possible with current technology. Results from a selection of the many experiments performed by this state of the art gravity gradiometer are presented in this thesis.

In the first half, groundwork for projection of test mass charging to the LISA mission will be provided by an analysis of the Pathfinder radiation monitor data. To do this, an existing GEANT4 model for the monitor is developed and a new component representing the on board processing of signal hits added.

The second half of this thesis relates to fundamental physics with gravity gradiometers, with an emphasis on measuring the gravitational constant in space. The measurements will be presented with arguments for a number of improvements so that future gradiometers can improve on the results outlined in this work.

Contents

List of Figures

Chapter 1

Gravitational Wave Astronomy

1.1 Introduction

The practice of Astronomy as a tool to study the universe beyond our immediate planet is thought to have existed throughout the history of the human race. From neolithic relics determining solar position in the year to modern telescopes observing distant astrophysical objects, human beings have found many ways to gaze at the stars and contemplate the dynamics governing their motion and the mechanisms enabling their existence. Beginning as a method to predict the seasons for harvests, astronomy has flourished in tandem with sociological, geographical and religious movements in history.

By watching celestial bodies move through the sky, astronomers have developed the concept of gravitation from a simplistic model to a more concrete description of the mechanics of the solar system and at cosmological scales. More recently, these laws have been united with advances in geometry to form the General Theory of Relativity (GR) [48][49], and with this theory came the prediction of a new kind of radiation: gravitational waves (GWs). Over a century on, technology has advanced enough to reach the signals from these waves, heralding the beginning of gravitational wave astronomy.

Humans have gazed at the universe with a variety of instruments all designed to collect electro-

magnetic radiation. Propagating as minute ripples in the fabric of space-time itself, GWs allow an observer to now 'listen' to the universe, adding an extra dimension of information gleaned from astrophysical objects. Many detectors have been proposed to measure this radiation, each targeting a different frequency range arising from a variety of sources. Some of these sources have electromagnetic counterparts, which presents yet another dimension to be explored in which information relating to the gravitational universe can be linked to electromagnetic phenomena.

Gravitational radiation was one of the final cornerstone predictions of GR to be measured. Following the results of aLIGO in 2016 [5], verifying their existence constituted a major success for GR and the beginning of a vast and rich new field through which the universe can be observed.

1.2 Gravitational Waves

Although GWs were first formally predicted by GR, they were alluded to before the theory was introduced. Comparisons were drawn between the inverse-square law in both gravitation and electromagnetism [69][101], leading to the idea of an accelerating mass producing gravitational radiation, in the same way that an accelerating charge will produce electromagnetic waves. It would seem that moving from inertial to non-inertial motion would be the key to emitting GWs.

In his 1915 and 1916 articles, A. Einstein introduced the concept of using a manifold, a collection of points in a set, to describe four dimensional space-time. This revolutionized the way gravity was thought about as now space and time stood with equal weight instead of the previous '3+1' approach of classical mechanics. Arguably the most important idea was that time is not absolute but relative to the observer; it is another coordinate indicating position in the manifold.

GR stipulates that space-time can be fully and uniquely described by a four dimensional, pseudo-Riemannian manifold that is minimally coupled to the stress-energy tensor. That is to say, a manifold in which distances between points, angles between vectors, etc., are described by

a metric $g_{\mu\nu}$, where $\mu, \nu \in \{0, 1, 2, 3\}$ – corresponding to time and to three spatial coordinates, respectively – for each point in the manifold. In the Einstein Field Equations 1.1, curvature of the space-time, encoded in $g_{\mu\nu}$, couples to matter to first order via the curvature (Ricci) tensor $R_{\mu\nu}$ together with the curvature (Ricci) scalar $R = R(g_{\mu,\nu})$, where $R = g^{\mu\nu}R_{\mu\nu}$ and $g^{\mu\nu}$ is the contravariant (dual) metric tensor of the space-time. This leads to the connection between mass and the curvature of space-time stated in the Einstein field equations

$$G_{\mu\nu} = R_{\mu\nu} - \frac{1}{2}Rg_{\mu\nu} = \frac{8\pi G}{c^4}T_{\mu\nu} \tag{1.1}$$

where c is the speed of light, G is the Newtonian constant of gravity ($= 6.674(1) \times 10^{-11}$ $\mathrm{m^3kg^{-1}s^{-2}}$), and $R_{\mu\nu}$ is a function of the metric. $T_{\mu\nu}$ is the stress-energy tensor, which describes the distribution of matter as its components are related to density and pressure.

Einstein showed that GWs naturally follow when considering the metric far from a massive source that warps the space-time around it in a particular way. He linearized the metric, indicating a large distance far away from a very massive body, and found that the signal strength and shape $h_{\mu\nu}$ depends on a quadrupole tensor $I_{\mu\nu}$ of the source. This link demands that the source dynamics be non-symmetric orbital motion in order to produce this radiation, for example a pair of co-orbiting black holes or an asymmetric spinning neutron star. Once emitted, the radiation propagates to the observer in the form of a small, wave-like perturbation to the flat background space-time with Minkowski metric $\eta_{\mu\nu}$. Putting these together, and denoting the distance between the source and observer by r, and spatial indices using roman letters $j, k, l, m \in \{1, 2, 3\}$, the equations describing the radiation become

$$g_{\mu\nu} = \eta_{\mu\nu} + h_{\mu\nu}, \qquad h_{jk} = \frac{4G}{rc^4}(\ddot{I}_{jk} - \frac{1}{3}\delta_{jk}\delta^{lm}\ddot{I}_{lm}); \qquad I_{jk} = \frac{1}{c^2}\int d^3y\, T_{00}y_jy_k. \tag{1.2}$$

Here, h_{jk} is the time-dependent strain of space, and $\ddot{I}_{jk} - \frac{1}{3}\delta_{jk}\delta^{lm}\ddot{I}_{lm}$ is the second derivative with respect to coordinate time t of the *mass quadrupole tensor* of the source of gravitational waves: this tensor vanishes if the source possesses spherical symmetry. $I_{jk} = \frac{1}{c^2}\int d^3y\, T_{00}y_jy_k$ is the time-dependent moment of inertia tensor of the source, where $T_{00}(y, t)$ is the time-time component of the source's stress-energy tensor in equation 1.1, and d^3y is an element of the

source's volume.

Therefore, $T_{00}(y,t)$ is the mass-energy density (i.e. energy per unit volume) of the source, such that $d^3y\,T_{00}(y,t)/c^2$ is a mass element of the source with coordinates (y_j, y_k) local to the source and measured from its centre of mass. Thus, $d^3y\,T_{00}(y,t)y_jy_k/c^2$ is the second-moment of that mass element about the source's centre of mass; and so the diagonal tensorial components $I_{jj} = \int d^3y\,T_{00}(y,t)(y_j)^2/c^2$ are the (time-dependent) 'moment of inertia' components of the source's tensor of inertia, while the $I_{jk} = \int d^3y\,T_{00}(y,t)y_jy_k/c^2$ $(j \neq k)$ are its (time-dependent) 'product of inertial' components. Equation 1.2 shows that h_{jk} has components that decrease in amplitude very slowly with distance r – as $1/r$ in fact. Therefore, gravitational radiation is long-range and vary with the retarded time $t - r/c$.

The importance of equation 1.2 is that anything that changes both periodically and asymmetrically in time will produce radiation, which will be experienced by a distant observer as strain $h = \frac{\delta l}{l}$ on a distance l. Radiated energy will propagate at a frequency that depends on the features of the source dynamics, and as a feature of the space-time itself, un-obscured by foreground sources. In this way it is a much cleaner source of information compared to electromagnetic radiation, although typical strains can be as low as 10^{-22}. This makes detecting GWs much more difficult than observing light from distant astrophysical objects.

As the weak field wave passes through a ring of test particles, disturbances occur in unique polarizations. Practically speaking, there are two polarizations of the detected gravitational waves, as illustrated in Figure 1.1 taken from ref [70].

There are two transverse polarizations in GR, shown above and below the time axis in Figure 1.1. These are usually denoted by h_+ and $h_\times$, with the received radiation always being some linear superposition of the two. For example, GWs emitted along the rotation axis of a binary Neutron Star (or Black Hole) system are polarized both h_+ and $h_\times$, with equal amplitude and phases separated by 90°, so that the resulting radiation is circularly polarized. On the other hand, GWs emitted in the orbital plane of such a system are linearly polarized (h_+, say). These modes cause the ring of particles in a plane perpendicular to the direction of travel to modulate back-and-forth in a plus and cross fashion, as illustrated in the drawings.

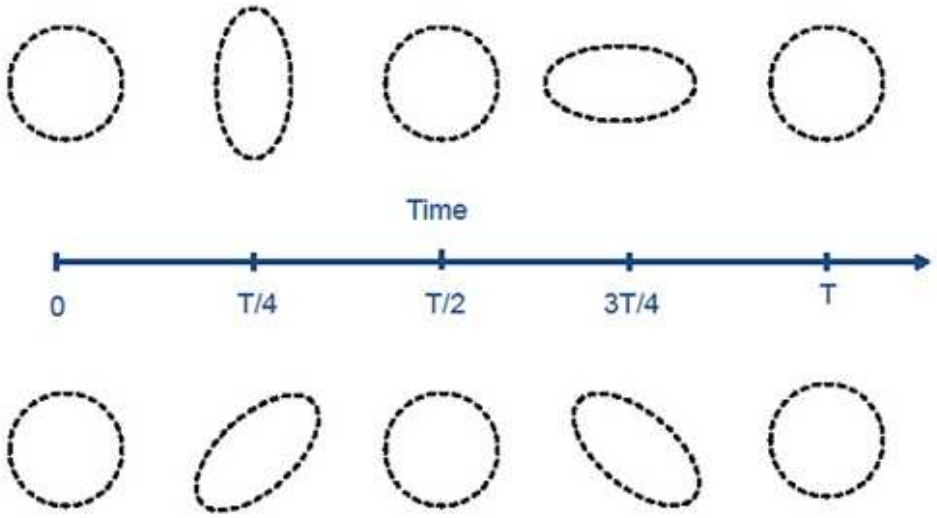

Figure 1.1: Einstein's GR predicts two possible polarization states of gravitational radiation, as shown above and below the time axis and denoted by h_+ and $h_\times$ respectively. These polarizations have been detected [4, 6, 7, 8, 3, 9]. When passing perpendicularly through a ring of test masses, they cause the transverse deformations shown with period T. Figure taken from ref [70].

The general waveform observed can be complicated to solve for, but encodes information about the source that can otherwise not be found using electromagnetic telescopes. This is invaluable when considering cases where no electromagnetic radiation is emitted, for example with binary black holes.

1.3 Sources of Gravitational Radiation

The full GW spectrum reaches from periods of the age of the universe to around hundredths of a second, where limitations of astrophysics impede faster rotations. Between these limits exists a diverse zoo of potential sources encoding a variety of information about astrophysics and cosmology.

The lowest energy sources are cosmic microwave B-modes. These arise from quantum fluctuations in the early universe. Many orders of magnitude above this, around the 10^{-8} Hz level, are longer waves from extremely massive compact objects, such as supermassive black hole binaries found in the center of galaxies.

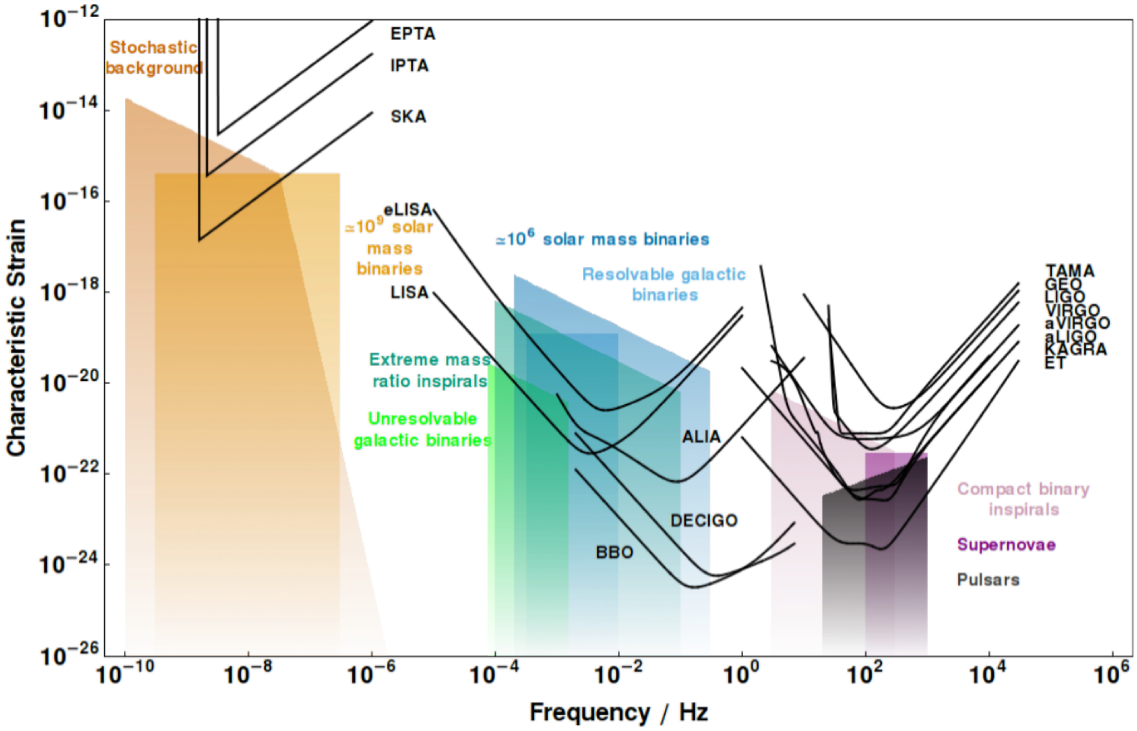

Figure 1.2: Strains expected from a sample of sources and sensitivity curves for a selection of experiments [95]. For descriptions of each source and experiment see text.

Extreme mass ratio inspirals (EMRIs), where a stellar mass compact object orbits a super massive black hole, populate the 10^{-3} Hz region. Much faster sources, such as pulsars with imperfections, a-symmetric supernovae and binary compact objects, radiate at 10-10^3 Hz.

Figure 1.2 illustrates the characteristic strain amplitudes for these sources and a selection of experiments targeting various frequency bands. Each source has a separate motivation for its detection. Merging black hole and neutron star binaries are characterized by a 'ringdown' and 'chirp' of the strain signal during coalescence, which can be related to the gravitational luminosity distance so that they act as 'standard sirens' (the GW equivalent of 'standard candles') for the determination of actual source distances – the 'holy grail' of astronomy [125] [9]. The stochastic background could probe relic gravitational waves from the early universe [30]. Asymmetric supernovae explosions and pulsars could help to develop the theories behind such phenomena and the equations of state for these objects. EMRIs are useful for various reasons [17], one of which is that they are slightly easier systems to solve the field equations for, and so can be used to constrain modifications to GR [131]. Resolvable galactic binaries include verification sources that can be used to calibrate a space based experiment.

Characteristic strains as low as those listed in the example plot illustrate the level of technology required to measure them. Einstein himself deemed the signals too small to ever be within experimental reach. A century on, modern physics has exploded in advances, making precise measurements of distances and times within the requirement to hear these signals.

1.4 Detectors

From the 1950's to the 1970's, many advances were made in analytic solutions for the Einstein field equations. Coordinate systems were developed that removed singularities that had rendered one of the first solutions by Schwarzschild inconsequential to contemporary astronomers [84] [112]. Explanations for the existence of compact objects emerged [39][55], and soon the first pulsar was observed [72][98]. As the field of GR grew, so too did the desire to measure gravitational radiation.

1.4.1 Resonant Bar Detectors

Through the late 50's and early 60's, J. Weber developed an idea to use energy deposited by GWs to excite the normal modes of a cylindrical bar. In essence, a resonant reaction to the passing radiation [128].

He argued that the excitation would be connected to the Riemann curvature tensor, which encoded the effects of the passing GW. Although he was never successful, despite several claims that he had been, these detectors still exist today. A more modern example is the NAUTILUS experiment operating at below 1 K, and searching for 10^3 Hz GWs [16].

Although there have been several generations of this experiment, it has largely diminished in popularity. State-of-the-art equipment was applied to the original design but sensitivities below $h \sim 10^{-19}$ were never reached.

1.4.2 Pulsar Timing Arrays

At the other end of the GW spectrum are pulsar timing arrays (PTAs), indicated in Figure 1.2, such as EPTA [83] (European Pulsar Timing Array), IPTA [73] (International Pulsar Timing Array which includes EPTA), and SKA [42] (Square Kilometer Array, planned for 2018-2030) for the three generations of arrays. The long periods of waves detectable by these arrays belong to relic GWs from the early universe in a stochastic background, and supermassive black hole binaries thought to populate the centres of galaxies.

As these long transient waves make their way through the universe, they disturb binary pulsars in quasi-random, correlated patterns giving rise to a lighthouse effect. As pulsars rotate highly regularly their radio loud jets periodically come in and out of contact with the Earth. PTAs timing these 'blips' from thousands of light-years away are sensitive to disturbances, say from a passing GW, in the regular signals received.

One of the most famous examples of Pulsar timing is the Hulse-Taylor binary. Timed since the 70's, the orbital decay of this source has been found to agree to a remarkable level with the predictions set by GR [114].

1.4.3 Ground Based Interferometers

In general, interferometers measure changes in the time it takes a laser to travel a given distance. Using the universality of the speed of light, any deviation in the time of flight would indicate a change in the distance travelled. Periodic deviations would therefore indicate a passing wave, extending and contracting the length sinusoidally.

Changes in time of flight are measured using a Fabry-Pérot interferometry method, where a laser beam is split, and then sent to two distant mirrors before returning. If there is any difference in arm length travelled by the two parts of the split beam, then their phases will be different on recombination. The resulting beam therefore has a power relative to the initial beam that is a function of relative changes in the detector arm lengths.

Given the polarizations of passing GW radiation, a wave passing normally to the plane containing the detector arms will disturb the arm lengths out of phase to one another. This then causes the recombined laser power output to modulate at a frequency equal to that of the passing wave, allowing a detection to be made.

Ground based detectors are fairly limited in size by area available. Most extend several kilometers, with several passes of an arm length to extend the effective arm length and amplify signals. Current ground based detectors include GEO600 [87], Virgo [35], and aLIGO [85] (previously LIGO). In order to localize a source on the sky, it is necessary to have more than one detector to triangulate a signal, including the use of time delays between detectors at different locations. As a result, detectors listed here work together as a larger collaboration.

Recent results from these experiments include the first detection of a GW signal from a Black Hole-Black Hole ring-down and merger, designated GW150914 [5]; and, more recently, four further strong GW signals from Black Hole-Black Hole mergers: GW151226, GW170104, GW170608, and GW170814 (plus one further, probable, but weaker, signal: LVT151012) [3] [4] [6] [7] [8]. Moreover, on 17th August 2017, a signal from a much more local source was observed: a corporeal Neutron Star-Neutron Star ring-down and merger (GW170817), which was accompanied by an electromagnetic (gamma-ray) pulse detected by the Burst Monitor on the Fermi Gamma-ray Space Telescope (formerly GLAST). This gamma-ray pulse arrived just 1.7 s after the GW merger signal following a passage through the cosmos of 130 million years. Indeed this merger event was observed subsequently across the electromagnetic spectrum, opening the way for true multi-messenger astronomy. This event has shown that the speed of gravitational waves is equal to the speed of light – as predicted by Einstein's GR – to within 5 parts in 10^{16} [9]. All of the GW sources above varied in their final merged masses from $2.7\,M_\odot$ to $62\,M_\odot$, where $M_\odot$ is the mass of the Sun. Future ground based interferometers, such as KAGRA [106] (which will incorporate lessons learned from the decommissioned experiment TAMA [10] and cryogenic mirrors) and LIGO India [75], will join this collaboration in the next few decades, increasing the localization statistics and overall sensitivity.

As first generation detectors move to their evolved, second generation updates, for example

LIGO to aLIGO, interest has also been shown in developing a third generation of detectors. The Einstein telescope (ET) [102], which would extend much further to 10 km arms and boast cryogenically cooled mirrors, would enjoy a substantially enhanced sensitivity. This is thanks in part to an additional arm and isolation from various noise sources by placing the detector underground.

1.4.4 Space Based Interferometers

As ground detections accumulate, population statistics for stellar mass binary compact objects are moving to the higher end of *a priori* predictions. This has substantial knock on effects as attention is refocused on the statistics of other sources. As the source frequency is lowered from tens of Hz to Hz and even mHz, wavelengths increase accordingly. Reaching as far as millions of kilometers in the case of LISA targets, it is essential to correspondingly increase the arm length of these detectors. The only way to provide enough space is to move outside the confines of the Earth, and perform interferometry between pairs of satellites rather than suspended mirrors. Fortunately, the added advantage of moving to space is isolation from spurious gravitational disturbances on the Earth such as seismic activity.

Unlike the signals for ground based detectors lasting fractions of a second, sources for space based detectors have longer periods reaching up to hours. Long-term monitoring of signals entering and leaving the sensitive axis as the detector orbits around the Earth and/or Sun then enables localizations to be made.

Currently there are no operational detectors in space, but plans are well underway with some detectors already adopted by various space agencies around the globe. The example detectors listed in the middle region on Figure 1.2 include LISA [43] (previously eLISA), ALIA [64], and proposed second generation experiments like DECIGO and the Big Bang Observatory [132]. Not shown in this diagram is TianQin [88], a planned observatory targeting 10^{-1}-10^{0} Hz in an Earth orbit with similar experimental set up to LISA.

Second generation space detectors aim to increase the number of detectors operating with cor-

related signals. As more interferometers join the measurement, sources from ground based detectors are captured by the broadened sensitivity band. Proposed experimental improvements deepen the bands, allowing the detection of relic waves from the early universe. These observatories are many decades away though, and present many technological challenges to be met in the years to come.

1.4.5 Laser Interferometer Space Antenna

The Laser Interferometer Space Antenna, or LISA for short, is a joint European Space Agency (ESA) and NASA space based detector. Its three arms extend 1-5 $\times$ 10^6 km depending on design in an equilateral triangle, and allow two interferometric measurements to be made simultaneously, improving signal fits.

Each spacecraft will house a pair of test masses belonging to different measurement arms. The typical strains h that LISA will target is of the order 10^{-18}-10^{-20}, meaning it will be sensitive to disturbances around 10^{-9}-10^{-12} m. In contrast to ground based detectors that measure changes in absolute distance travelled by light, LISA will measure disturbances to geodetic motion between pairs of identical test masses.

Figure 1.3 shows the proposed LISA orbit according to the recent proposal document to the European Space Agency for the third large scale mission selection [1]. The spacecraft constellation will follow an Earth trailing trajectory, moving along a geodesic that allows a large portion of the sky to be scanned over the course of a year.

The arm length sets the base wavelength accessible to the detector. Sitting in the mHz region of the GW spectrum, a host of sources are within range for LISA. Included in the proposal was an account of the various sources available and the science that can be done with them. Figure 1.4 shows the plot used in the document to illustrate how these sources evolve in time.

The inspiral, chirp and ringdown of massive black hole Binaries (MBHB) are shown by the yellow-red lines, where colour coding indicates frequency migration through the merger event. Resolvable stellar mass binaries, denoted by the violet points, include known sources in the

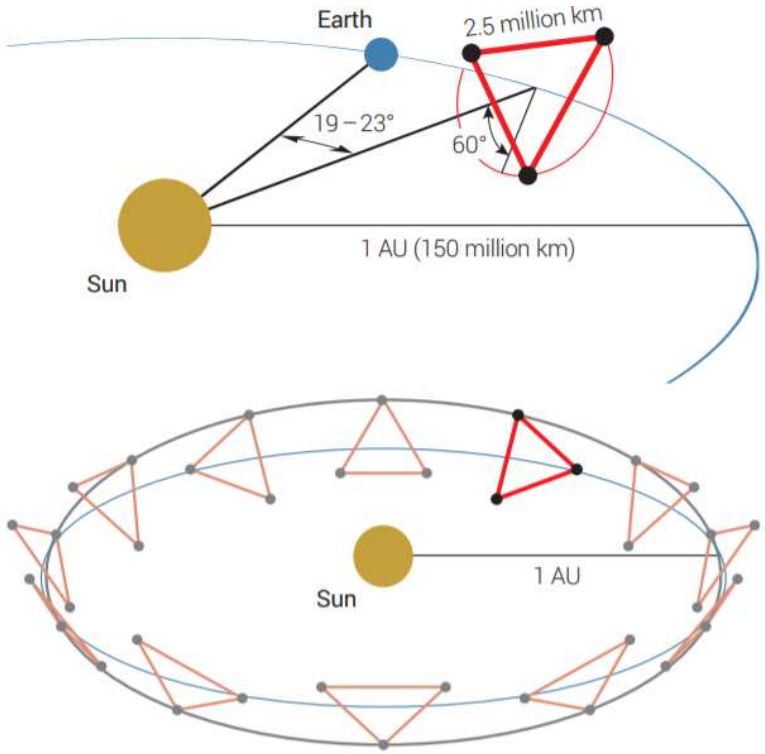

Figure 1.3: Proposed orbit for LISA [1].

galaxy giving rise to 'verification binaries'. The green line indicates the sensitivity of the experiment, while the black dashed line is the sum of the detector base sensitivity and the unresolvable binaries that make the galactic background noise. Typical EMRI signals are shown as red lines that indicate the harmonics of the pulsing signal. As the much lighter (around stellar mass) compact object orbits a supermassive black hole, it moves on an eccentric, precessing orbit resembling a roulette curve in three dimensions to a distant observer. Due to this complicated orbit, the GW signal occupies a region of frequencies and beats back and forth, rather than an accelerating migration from one region of the spectrum to the next.

Also included in Figure 1.4 are typical sources detectable by ground based detectors such as LIGO. These lighter compact object binaries originate in the LISA band and migrate to higher frequencies where their chirp is detected. This poses an interesting opportunity to study wave signals, for example from the back prediction of the first detected event in September 2015 (blue, solid line), across multiple detectors.

LISA sources can be used in a variety of ways to provide astronomy with new information about the Universe. Merger events detail the history and evolution of black holes in the uni-

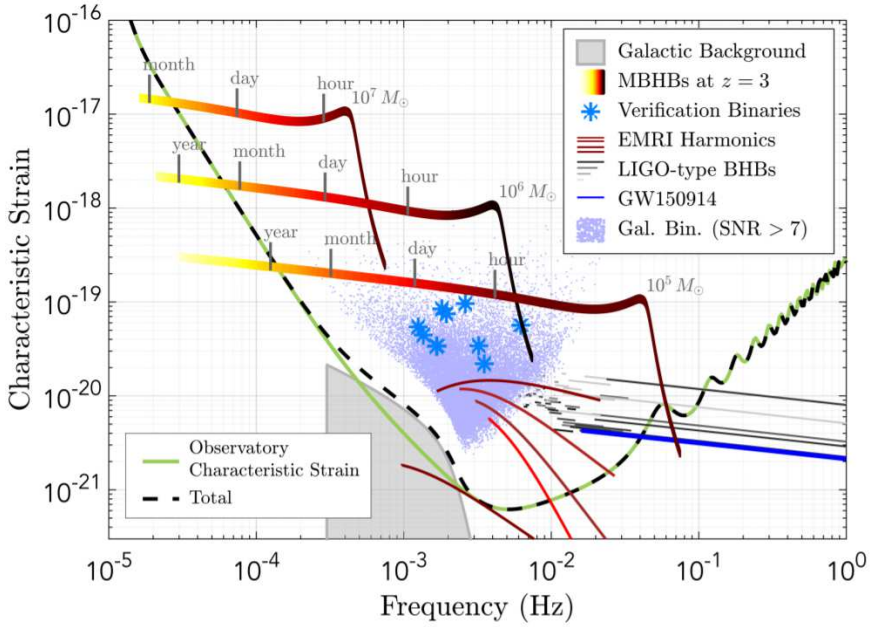

Figure 1.4: Example sources measurable by LISA [1].

verse, which can also be linked to galaxy formation as supermassive black holes are thought to populate the centres of galaxies. EMRIs provide a high energy laboratory for tests of gravitation, with orbiting stellar mass compact objects tracing out the gravitational regime they move in. LISA can provide cosmological information too, providing insights to gravitational luminosity distances which can shed light on curvature. The possibilities indeed seem endless as continued research on this experiment uncovers more applications of LISA detections.

1.5 LISA Pathfinder

The sensitivity required to achieve a LISA mission posed a challenge to modern physics. In order to reach the typical strains of LISA sources, two test masses (TMs) per interferometer arm would need to be in drag free acceleration with noise disturbances lower than parts in 10^{15} $\mathrm{ms}^{-2}\mathrm{Hz}^{-1/2}$ in the mHz region. In other words, the spacecrafts would need to follow the test masses, which would in turn need to move independently of the spacecrafts in the sensitive axes.

In order to test that available technology is capable of achieving this, the European Space Agency proposed a smaller scale, proof of concept mission: LISA Pathfinder [126]. This exper-

iment, launched in December 2015 and decommissioned in July 2017, demonstrated free-fall in one direction at fms^{-2}, over two orders of magnitude better than some of the preceding experiments. Each source of noise jittering the TMs at mHz frequencies was characterized by dedicated experiments.

Within the LISA Technology Package (LTP), the science payload on Pathfinder schematically shown in Figure 1.5, two $5 \times 5 \times 5$ cm^3 gold platinum alloy TMs weighing around 2 kg each were enclosed in individual housing structures, and separated by 36.7 cm with an optical bench in between. The whole LTP was attached to the spacecraft, and supported by struts. Optical windows, one on each housing pointing towards the optical bench, allowed a laser to pass between the two test masses for the interferometry measurements.

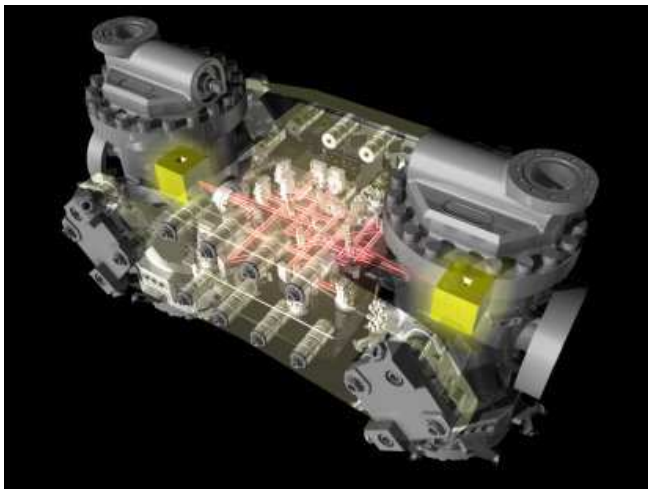

Figure 1.5: Schematic diagram of the LISA Technology Package, the science payload for Pathfinder. Taken from ref [51].

Mercury lamps illuminating both TMs and housings allowed charges to be moved between the TMs and spacecraft for discharging and experiments [65]. Sensing and actuation electrodes in the housing walls applied audio frequency capacitive forces to the TMs to suspend and measure their positions in six degrees of freedom per TM.

Thermal sensors and heaters throughout the LTP performed thermal experiments [60], and coils placed near the TMs induced magnetic fields for experiments that estimated TM magnetic properties and disturbances to the magnetic environment [46]. Every component mounted on the structure was carefully weighed, and a compensation mass placed to balance the gravitational

forces at each TM to within requirements.

Following several burns and an injection into its quasi-stable, Lissajous orbit, the spacecraft took six months to orbit the first Lagrange point (L1), located between the Earth and Sun with solar orbital period of one year. Micro-Newton thrusters on the outside of the spacecraft continually compensated for radiation pressure from the Sun which would otherwise move the spacecraft off orbit. Figure 1.6 shows a cartoon of the manoeuvre, injection and final orbit around L1.

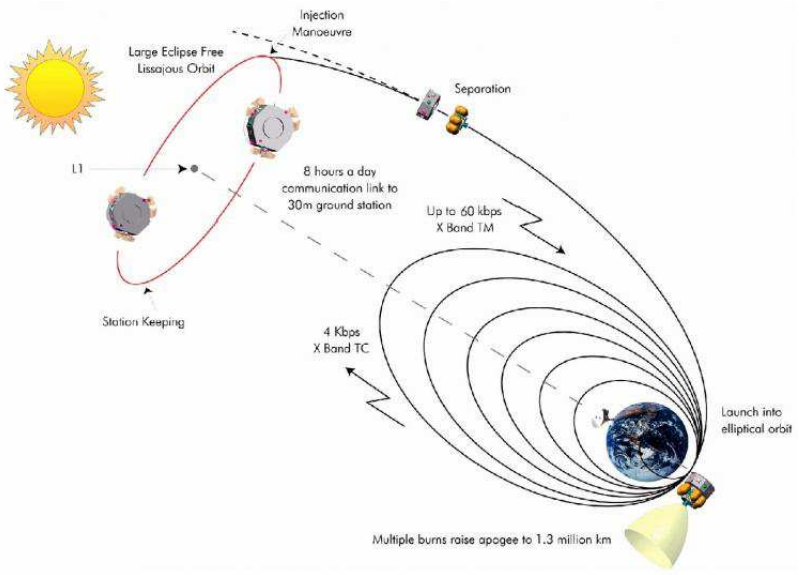

Figure 1.6: LISA Pathfinder orbit following a Lissajous trajectory around the first Lagrange point where the orbital period around the Sun exactly matches the orbital period of the Earth around the Sun. Notice the 'slingshot' manoeuvres around the Earth to minimize fuel consumption. Taken from ref [50].

Through the mission, noise runs were performed that measured the differential acceleration between the TMs along the TM-TM axis. One of the TMs, labeled TM1, was used to control the satellite drag free system while the second, labelled TM2, was effectively 'nudged' along to follow the geodesic of TM1. Reducing the noise of the relative acceleration, Δg_x, to below 10^{-15} ms^{-2} at 1 mHz was the main science goal of the mission. Doing this would mean that if achieved in LISA, the sensitivity curve in Figure 1.4 would be reached.

In February 2018 a final, end of mission performance was reported by the collaboration [14]. The model for the noise accounted for by individual experiment campaigns was reported to

follow the relation

$$\Delta g(t) = \Delta\ddot{x}(t) + \omega_2^2 \Delta x(t) + \Delta\omega_{12}^2 x_1(t) - g_c(t) - g_\Omega(t) + \delta_y L\dot{\Omega}_y - \delta_z L\dot{\Omega}_z \tag{1.3}$$

where $\Delta g_x(t)$ is the primary science signal from LPF – the differential force per unit mass. $\Delta x(t) = x_2(t) - x_1(t)$, and x_1, are the differential displacement of TM2 relative to TM1 as measured by a dedicated heterodyne laser, and TM1 relative to the spacecraft, respectively. $g_c(t)$ is the known time-series, controlling force per unit mass applied electrostatically to TM2, in order to slave it to follow TM1 via a slow controller with unity gain around 1 mHz. The spacecraft also follows TM1, by monitoring $x_1(t)$, leaving TM1 drag free as no forces are applied to it in the TM-TM axis. In practice, $\Delta\ddot{x}(t)$ in equation 1.3 was calculated from the measured values of $\Delta x(t)$. g_Ω is the centrifugal force picked up by the TMs due to a noisy spacecraft angular velocity Ω. The restoring force per unit mass, or stiffness, parameters $-\omega_1^2$ and $-\omega_2^2$ apply to TM1 and TM2 respectively, where ω_1 and ω_2 are the respective natural resonant angular frequencies about their centred positions. $\Delta\omega_{12}^2 = \omega_2^2 - \omega_1^2$ in equation 1.3 is therefore a differential stiffness that couples spacecraft motion into Δg_x. The sum of the last two terms in equation 1.3 represents the x component of the Euler force per unit mass due to a noisy Ω, where L is the total distance between the test mass centres of mass, and $\delta_{y,z}$ are fractional displacements of the TM away from the alignment with the sensitive x axis (in the TM-TM direction), but measured along the alternate axis: $\delta_y \equiv (\Delta z/L)$ and $\delta_z \equiv (\Delta y/L)$. Note that dots refer to numerical time derivatives of the time series data.

System identification experiments were run at each actuation force configuration, ranging from ultra ultra ridiculously low (UURLA) with 50 pN actuation amplitude to 'Big' with 5 nN amplitude, to measure the stiffness parameters from the response of the feedback system to injected electrostatic forces on top of the actuation. The star tracker monitored the relative movement of distant stars to give the spacecraft angular velocity, while optical metrology readouts gave the relative displacements of TM1 to TM2 and TM1 to the spacecraft.

As detailed in the first results article, there are additional parameters that must be investigated and fit for [13]. An example of this was the gain on the electrostatic forces applied to each TM,

which were slightly different to the requested forces by a factor just over (under) 1 for TM1 (TM2). Details of these fits and a more in depth model used can be found in the article.

Figure 1.7 shows a plot of residual relative TM-TM acceleration ASD, $\Delta S_{\Delta g}^{1/2}$, from the article indicating the success of the instrument. Not only did it exceed its requirements (darker grey shaded region), but also the requirements for LISA (lighter grey shaded region) to be able to detects its target sources. The two curves show a noise run from April 2016 (blue), and another from February 2017 (red) highlighting the improvements made in this time.

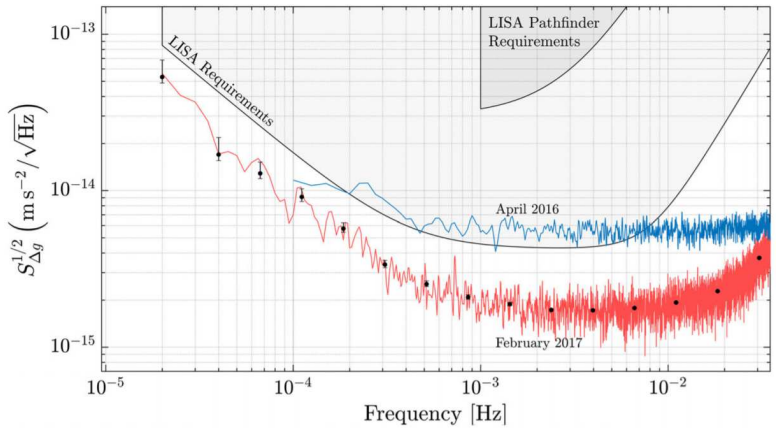

Figure 1.7: Noise performance of Pathfinder from mid-way and end of mission, along with the pre-flight requirements and sensitivity for LISA for comparison. Taken from ref [14].

Pathfinder has demonstrated that the concept of a LISA mission is within the scope of technology available today. However, there are additional difficulties to consider when moving from Pathfinder to a full LISA mission. For example, the layout of each spacecraft as the TMs are now skewed relative to one another rather than in line. As LISA moves through phase A of production, these difficulties will be addressed in tandem with outstanding questions and lessons learned from Pathfinder.

The analyses presented in this thesis have used the LISA Technology Package Data Analysis (LTPDA) toolbox in Matlab to process data. All plots have been produced using the plotting functions there. Unless explicitly outlined, all fitting algorithms have been done using various pipeline steps in the toolbox that were developed pre-flight for operations.

This thesis presents work done for several experiments performed on Pathfinder. Chapters 2 and 3 relate to the radiation environment that Pathfinder experienced at L1, detailing how work

on this can be incorporated into continued research on TM charging. Chapters 4 and 5 explore the lessons that can be learned from Pathfinder in the context of designing future experiments targeting fundamental physics in space.

Chapter 2

Outlining the Radiation Monitor Model

2.1 Introduction

One source of acceleration noise on LISA Pathfinder is stray electrostatic forces between the faces of the test masses and the electrode housings. The capacitances between the surfaces cause additional parasitic forces to arise as a test mass becomes charged due to incident energetic particles. The contribution of TM charging the electrostatic forces varies proportionally with the TM potential due to the charge accumulated, and contributes roughly as a $1/f$ function in frequency space with the amplitude proportional to the total TM charge. A dedicated experiment with exaggerated TM potential of 1 V significantly increased the noise below around 5×10^{-4} Hz in Figure 1.7, even during nominal science runs a TM potential never more than $0.2-0.3$ V produced a visible change in the low frequency noise. It is essential then to be able to accurately measure charge, and the rate at which charge accumulates, while also understanding the processes that cause charging to happen. This will then allow an accurate projection of this source of noise to LISA.

Sources of energetic particles that can cause charging to occur include solar energetic particles (SEPs) and Galactic Cosmic Rays (GCRs). SEPs, ranging in kinetic energy from a few keV

to several GeV, originate as a result of solar flares and coronal mass ejections. SEPs are, for the most part, not energetic enough to penetrate the spacecraft and reach the test masses as the majority of SEP protons have kinetic energy in the few MeV range [122]. Conversely, GCRs are a ubiquitous source of energetic particles originating outside of the galaxy, likely as a result of acceleration by supernovae and other shock mechanisms [22][23]. The flux of GCRs presents a source of continuous charging at a variable rate depending on the activity of the Sun's magnetic field, as the majority of GCR particles have kinetic energy above hundreds to thousands of MeV.

During the Pathfinder mission, test mass charging rates were measured at a variety of test mass potentials and suspension forces using a method detailed in section 2.7. In order to project the rates for LISA over different times of the solar cycle and evaluate the associated acceleration noise, it is important to understand the processes that cause TM charging, and how they relate to changes in GCR flux. This can be accounted for by correlating measured charging rates with GCR flux over the Pathfinder mission, which requires accurate measurements of the flux through the mission.

Energetic particles from GCRs pass through the SC and interact in several ways to deposit charge. This can be through ionization of electrons to or from the SC or TMs, or through nuclear interactions that cause secondary particles to shower onto or off of the TMs which also deposit charge. Furthermore, the stopping distance for a proton with kinetic energy around 100 MeV is comparable with the thickness of the TMs, allowing positive charges to also be deposited directly. Variations in the charging rate are directly linked to variations in the Sun's magnetic field, which can modulate the lower energy GCRs entering the heliosphere.

The Sun is a spectral class G, main sequence star with an interior comprising of three main layers [113]. The central core reaches from the center of the star to a quarter of the interior radius. This is where the Sun generates the majority of radiation through thermonuclear fusion of protons to fully ionized helium, and heavier elements via the carbon-nitrogen-oxygen cycle. The next layer, reaching out to around 70% of the interior radius, is the radiative zone where photons transport energy by absorption and re-emission. The outer region of the Sun is a

convective layer where the Sun's magnetic field is generated by the dynamo process [40]. These processes create small areas of magnetic over-densities which suppress radiation leaving the Sun's interior, giving rise to surface features like sun spots. These features therefore indicate regions where the magnetic field emerges and submerges as the field lines connect to form open and closed loops. The creation of these magnetically induced features rests in differential rotation and cellular-like motion of the plasma in the convective layer, in contrast to the near perfect solid body rotation of the core and radiative layer [77].

The overall consequence of the dynamo process is an 11 year solar cycle due to the 'rolling' and 'rotating' flux tubes that source the Suns magnetic field in the convective layer. Most notably, this periodic movement of tubules gives rise to the 'butterfly' diagram that gives the latitudinal dependence of sun spots as a function of time [90]. This diagram illustrates the correlation between solar surface activity and the underlying process creating the magnetic field.

From the surface of the Sun, the magnetic field threads the solar atmosphere, which is comprised of four main layers. The first is the photosphere, where the surface features of the Sun are observed [77]. These include Sun spots as well as solar faculae and granules, which are linked by closed magnetic loops originating in the convective layer below [76]. Other magnetic field lines extend through the chromosphere, transition layer and out through the large corona to meet the magnetic field of the local galaxy, forming open field lines. The polarity of the magnetic field generated within the convective layer causes these open fields to asymptotically approach one another at a surface defined as the heliospheric current sheet. As particles leave the surface of the Sun, they form a wind that extends out through the solar atmosphere. Fast and slow streams occur depending on the latitude of the sun and the surface features that alter the temperature, magnetic field and composition of the wind.

The solar wind dilutes in density as it propagates outward until it has a comparable momentum per unit volume as the radiation from the galactic centre. This defines a topological boundary called the heliopause, and marks the limits of the heliosphere. It is at this layer that the open field lines join the galactic magnetic field lines. This layer therefore also defines the limit of the region around the Sun where the solar magnetic variables dominate the attenuation of incoming

GCRs from outside the heliosphere. Outside this dynamic limit, GCR flux is assumed to be constant. As particles enter the heliosphere they are attenuated by the magnetic field in several ways that disproportionately affect lower energy particles compared to those of higher energy.

High energy GCRs are unaffected by changes in the solar magnetic field. In contrast, lower energy GCRs are scattered by features in the field. Their mean free path through the solar system is decreased, causing them to attenuate in flux before they reach 1AU. Connecting the flux with solar activity means solar minima correspond to GCR flux maxima and vice versa. At the time of the Pathfinder mission, the Sun was entering the end of the current solar cycle, corresponding to higher fluxes of lower energy GCR particles.

An additional complexity to consider is the Sun's rotation of around 27 days. As it rotated, the heliospheric current sheet propagated out in a spiral pattern, causing Pathfinder to cross it many times through the mission and experience a change in polarity of the magnetic field, which attenuated the solar wind slightly differently. The overall effect is a periodic change in the net measured GCR flux on a harmonic period of the Suns rotation, superimposed on the background flux with a gradual rise as the solar minimum is approached.

The origins of GCRs are thought to be linked to supernovae and possibly active galactic nuclei. Their composition has been measured both on ground and in space, and found to primarily be composed of protons (around 90%), helium nuclei (9%) and helium^3 nuclei [2]. Other components contributing almost 1% include electrons, nuclei of heavier elements and a very small proportion of simple, stable antimatter particles like positrons and anti-protons. Each component has a different flux spectrum characterized by a peak at several tens to hundreds of MeV, depending on the time of the solar cycle, and a tail asymptotically approaching zero at higher energies. In the case of Pathfinder, there is a hard cutoff in the dynamic range of energetic particles able to reach the TMs at around 70 MeV mainly due to shielding by the inertial sensor and vacuum chamber. Mass constraints on the satellite meant that no more shielding could be applied.

In order to correlate this activity with the measured TM charging rates, it is important to find a parameterization for the GCR flux. Fits can then be performed, and are reported in

chapter 3, to estimate the flux at different times based on *in situ* measurements of radiation on Pathfinder. This chapter outlines the model used to take the measured deposited energy spectra and convert them to an estimate of the GCR flux. Although the origins of GCRs and their attenuation in the heliosphere are complex and not well defined, it turns out there is a relatively simple way to model the flux using just one parameter and an assumption about the interstellar flux beyond the heliopause.

2.2 Solar Attenuation Parameter ϕ

The solar attenuation parameter ϕ was originally formulated by Gleeson and Axford [63] while considering the transport of particles in magneto-hydrodynamic systems. This was based on the work by Parker in 1965 [97] which aimed to solve the transport equations for the diffusion of charged energetic particles in a flow threaded with a magnetic field, where discontinuities carried by convection scattered the incoming particles.

This parameter is now used as a proxy for solar magnetic features attenuating GCR particles as they propagate through the solar wind. The model assumes a constant flux outside the heliosphere called the local interstellar spectrum (LIS). Burger *et al.* [33] hypothesized a form for the LIS based on a simulation of mono-energetic particles through a slab with turbulent magnetic field by Bieber *et al.* [26].

A more up-to-date outline of the parametrization, along with monthly values for ϕ since 1936, are reported by Usoskin *et al.* [123] A more detailed outline of the method is given by Usoskin *et al.* [124], which explains that, with some simplifying assumptions, Parker's transport equation can be solved to find an estimate for the LIS. In essence, this becomes an integration from the measured spectrum at 1AU out to the heliopause.

As the Voyager spacecraft pass the outer reaches of the heliosphere, the LIS of cosmic rays is now being refined [27]. The most up to date version of the LIS, in units of $\mathrm{m^{-2}s^{-2}sr^{-1}(GeV/nucleon)^{-1}}$,

for protons and helium nuclei (including isotopes) with kinetic energy E, in GeV/nucleon, are

$$J_{LIS,P}(E) = 3719.0\frac{1}{\beta^2}E^{1.03}\left(\frac{E^{1.21}+0.77^{1.21}}{1+0.77^{1.21}}\right)^{-3.18}$$
$$J_{LIS,He}(E) = 195.4\frac{1}{\beta^2}E^{1.02}\left(\frac{E^{1.19}+0.60^{1.19}}{1+0.60^{1.19}}\right)^{-3.15} \quad (2.1)$$

Including this in the solutions for the transport equation, and labelling for a species i of cosmic ray particle, the flux at 1AU can be written in terms of the modulation parameter ϕ as

$$J_i(E,\Phi_i) = J_{LIS,i}(E)\frac{E(E+2E_r)}{(E+\Phi_i)(E+\Phi_i+2E_r)} \quad (2.2)$$

where $\Phi_i = (eZ_i/A_i)\phi$ and $E_r = 0.938$ GeV/nuc.

Taking the high energy limit of equation 2.2 where $E >> (E_r, \Phi_i)$, then $J_i(E,\Phi_i) \approx J_{LIS,i}$, and $J_{LIS,i} \approx \frac{21208.8}{\beta^2}E^{-2.82}$, which is a straight line in $\log - \log$ space. In the low energy limit $E << (E_r, \Phi_i)$, and assuming $\phi \geq\sim 100$ MV, the flux becomes $J_i(E,\Phi_i) \approx 81859.2\frac{2E_r}{\Phi_i(\Phi_i+2E_r)}E^{2.03}$, another straight line in log-log space with an additive constant that is a function of the attenuation parameter. This demonstrates that E_r is a transition energy between the low and high energy dynamics of the flux. ϕ changes both the transition energy and the flux of low energy particles, while leaving the high energy region unchanged. This is expected given the high energy particles will be negligibly affected by changes in the magnetic field. For the low energy behaviour of the LIS, taking $\phi = 0$ before the limit, the flux becomes $J_i(E,0) \approx J_{LIS,i} \sim E/\beta^2 \sim const.$

Figure 2.1 shows some example fluxes with the LIS for both Protons and Helium nuclei. This work uses units of MeV for kinetic energy and cm^{-2} for flux as the properties of the apparatus match more closely to these units. Each spectrum is taken for a day at a time in order to improve the statistics in each bin. The high and low energy limits of Figure 2.1 clearly show the straight line behaviour in log-log space, with a turning point in between dependent on the attenuation of the flux and the species in consideration.

Using this model offers a way to link the count rates measured to the flux of particles. Since there is only one free dynamic variable, linking the space weather at the first Lagrange point to the

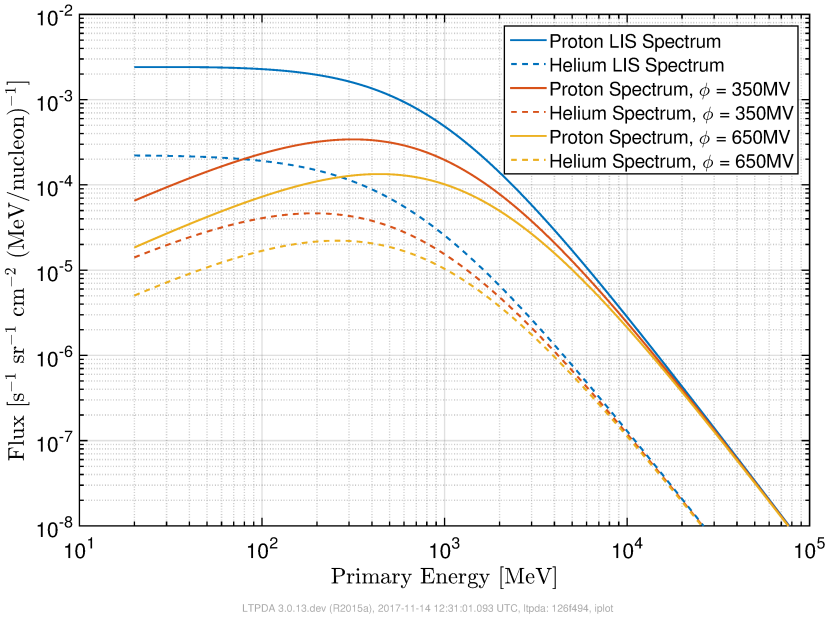

Figure 2.1: Example fluxes using the model from Usoskin *et al.* and Bisschoff *et al.* [123] [27] Solid lines indicate proton flux while dashed lines show helium nuclei (including isotopes). Blue shows the local interstellar spectra according to the most recent update to the model by Usoskin *et al.*

charging rates is simplified greatly. It should be noted that comparisons between measurements of ϕ from different experiments can only be done when the same LIS is used. Otherwise, comparisons can only be made qualitatively with the plotted curves.

2.3 Silicon Diode Detection of Cosmic Rays

When measuring the energy of a particle in space, there is a complex relationship between that particles initial energy and the energy it deposits in a detector. Described by interactions between the electrostatic fields inside the detector material and the charge and velocity of the particle traveling through the material, the relationship becomes stochastic if it follows the quantum nature of high energy interactions with solid state materials.

As can be expected, the energy deposited by a particle depends on the particle's kinetic energy. To see this, consider a single particle with velocity v and atomic number z passing through a thin layer of silicon with atomic number Z, density ρ and mass number A. The primary mechanism

for the passing particle to deposit energy in the material is through electron ionization, where the charged particle's electric field does work when approaching the clouds of electrons in the outer layers of the atom. Since energy is conserved, the work done is converted to mechanical energy knocking electrons into the conducting band of the silicon.

It can be inferred that the exact form for the energy required to stop a charged particle in a material will be proportional to the number of charges, the electric field and some function of the energy of the particle. The original derivation by Bethe and Bloch took into account relativistic effects, showing the formula as

$$-\frac{dE}{dx} = \left(\frac{ze^2}{4\pi\epsilon_0}\right)^2 \frac{4\pi Z\rho N_A}{Am_e v^2}\left[\ln\left(\frac{2m_e v^2}{I}\right) - \ln\left(1-\beta^2\right) - \beta^2\right] \tag{2.3}$$

where the velocity fraction $\beta = v/c$, and $\gamma = (1-\beta^2)^{-1/2}$, while m_e, ϵ_0 and α are the electron mass, permittivity of free space and the fine structure constant respectively. I is the average ionization potential for the material and N_A is Avogadro's number for the atoms per mole of a material. Lilley gives a good description of the terms in the book 'Nuclear Physics Principles and Applications' [86]. Figure 2.2 shows the differential energy equation evaluated for a proton travelling through silicon. In section 2.2, it was shown that typically protons have a kinetic energy in the MeV range, which, according to the example plot, is the region that most efficiently deposits energy in silicon.

An impulse is passed to the particle as it passes through the material that is governed by the square of the transit time and the square of the electromagnetic force it experiences ($\propto 1/v^2$ and $\propto (ze^2/4\pi\epsilon_0)^2$ respectively). It is also proportional to $1/m$, where m is the mass of the particle, and the density of electrons in the material $Z\rho N_A/A$. The derivation, as explained by Lilley, integrates over impact parameters of the charged particle to atoms/ions in the material, with a minimum impact parameter governed by the extent of the particle and the atoms themselves. These components can be seen in the form of the Bethe-Bloch formula, and so holistically the form can be reasoned.

This expression gives the average energy loss per unit length as a particle travels through a

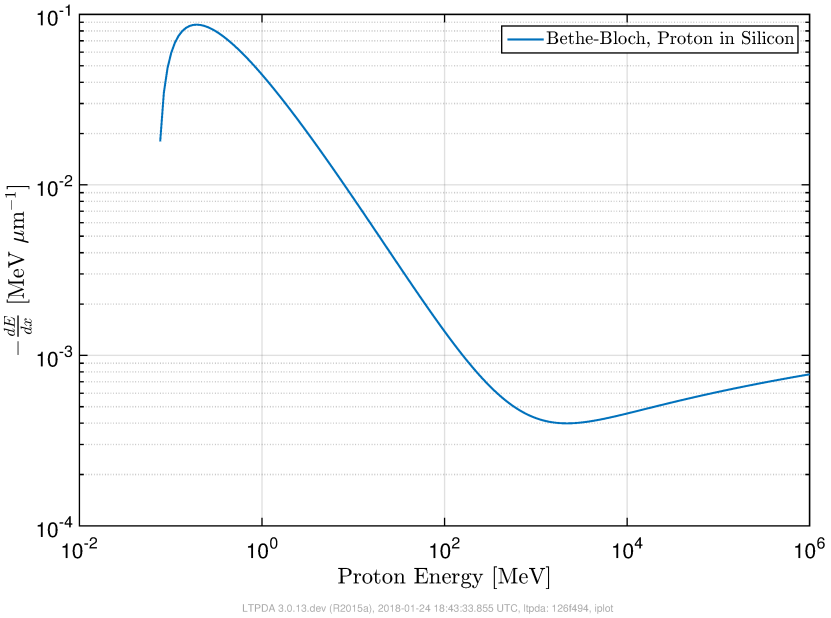

Figure 2.2: Example of the Bethe-Bloch formula for stopping power of a proton travelling through silicon.

material, such as a galactic cosmic ray particle traveling through a silicon diode detector. It should be noted that this is often used to calculate the distance a particle travels before it is completely stopped by the energy lost to the surrounding material. In reality there is a variation around this average value according to a Landau distribution

$$P(\lambda) = \frac{1}{\sqrt{2\pi}} e^{-\frac{1}{2}\left(\lambda + e^{-\lambda}\right)} \tag{2.4}$$

with parameter $\lambda = \frac{\Delta E - \Delta E^{B-B}}{\xi}$, where ξ is the width of the distribution and a function of particle energy, ΔE is the energy deposited and ΔE^{B-B} is the average energy deposited according to the Bethe-Bloch formula.

In the case of the radiation monitor on LISA Pathfinder, the process is a stochastic version of this exact formula as particles are neither monoenergetic nor uniform in energy distribution [12] [127]. Furthermore, the detector is of a set, thin thickness relative to the typical stopping distances for protons above several tens of MeV. This means that both electromagnetic and hadronic showering become important as particles pass through and interact to create lower energy particles that then deposit in the second diode.

These factors suggest that the deposited energy measured by the Pathfinder radiation monitor does not follow the exact shape of the Bethe-Bloch formula, but instead samples the regions around it. This creates a spread of deposited energy and a probabilistic relationship between primary energy and deposited energy in the detector. Implications of this include a more complex interplay between cosmic ray energy and test mass charging rates, and therefore an added difficulty to the task of projecting charging rates to LISA.

In order to capture these complexities, simulations of these interactions are stochastic in nature. The sampling process is a Monte Carlo method in GEANT4 that takes into account the particle energy and trajectory in the probability for an interaction to occur. Furthermore, the species of particle in consideration is accounted for in the physics list that introduces various interactions and secondary interactions within the shielding around the detector and the material of the detector itself.

2.4 Radiation Monitor

In order to correlate charging rates with the radiation incident on the test masses, Pathfinder includes a Radiation Monitor (RM) that aims to estimate the dose of GCR radiation received by a test mass, and detect any abrupt changes in the radiation environment if a SEP event occurs. It aims to count the number of energetic particles passing through its sensitive regions, whose shielding is similar to that around the test masses.

Energetic particles excite electrons into the conduction band of the silicon in the active area of two Hamamatsu dual PIN photo diodes (S8576-01), as shown in Figure 2.3a, where each electron-hole pair requires 3.55 eV to create. Conduction band electrons are then swept out of the diodes and into the circuitry, see Figure 2.3b, by a 70 V bias applied across each diode. This creates a current pulse, which is used to estimate the deposited energy from the primary particle. Many particles then create a deposited energy spectrum that is dependent on, but not equal to, the GCR flux energy distribution.

An early design document from 2006 details the dimensions and full circuitry used by the

(a) Production photograph of a single PIN diode recycled from the Fermi Gamma Ray Telescope for use in the Pathfinder radiation monitor. Two of these are stacked in a telescopic arrangement with a small translational offset in overlay. Only the larger area is operational for Pathfinder.

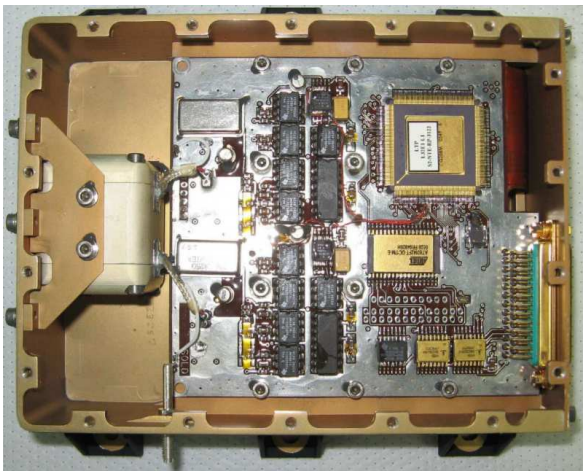

(b) Photograph of the electronics used to convert a small burst in current from a hit within a diode to a measured energy. Both a singles count and coincident count are measured where a hit is recorded in one or two diodes respectively.

Figure 2.3: LISA Pathfinder Radiation Monitor photographed before flight.

RM [29]. Figure 2.4, taken from this document, shows the schematic layout of one of the Hamamatsu dual PIN photo diodes. Note the two silicon regions, each 320 $\pm$ 10 μm thick, denoted by PIN diode A and B. For the Pathfinder RM, only the B diode (larger area) is active and connected to the circuitry. However, diode A is included in the simulations here as interactions may produce secondaries that are measurable in Diode B. Each diode is covered in an epoxy resin to protect the silicon wafer embedded in the ceramic carrier. The full RM includes two of these PIN photo diodes, mounted in a telescopic arrangement, inside a copper shielding box. The monitor is then encased inside an aluminium container, and mounted to the inside of the spacecraft.

The design document cites two main electronic noise contributions. The signal processing adds a dark current and capacitive noise to the estimated deposited energy. This is assumed to follow a Gaussian distribution with a standard deviation $\sigma_E \approx 3.46$ keV and an offset energy μ_E associated with the discriminator that is less than 2.5 keV, according to pre-flight lab tests.

Figure 2.5 shows a flow chart for the circuitry used in the radiation monitor. This takes a

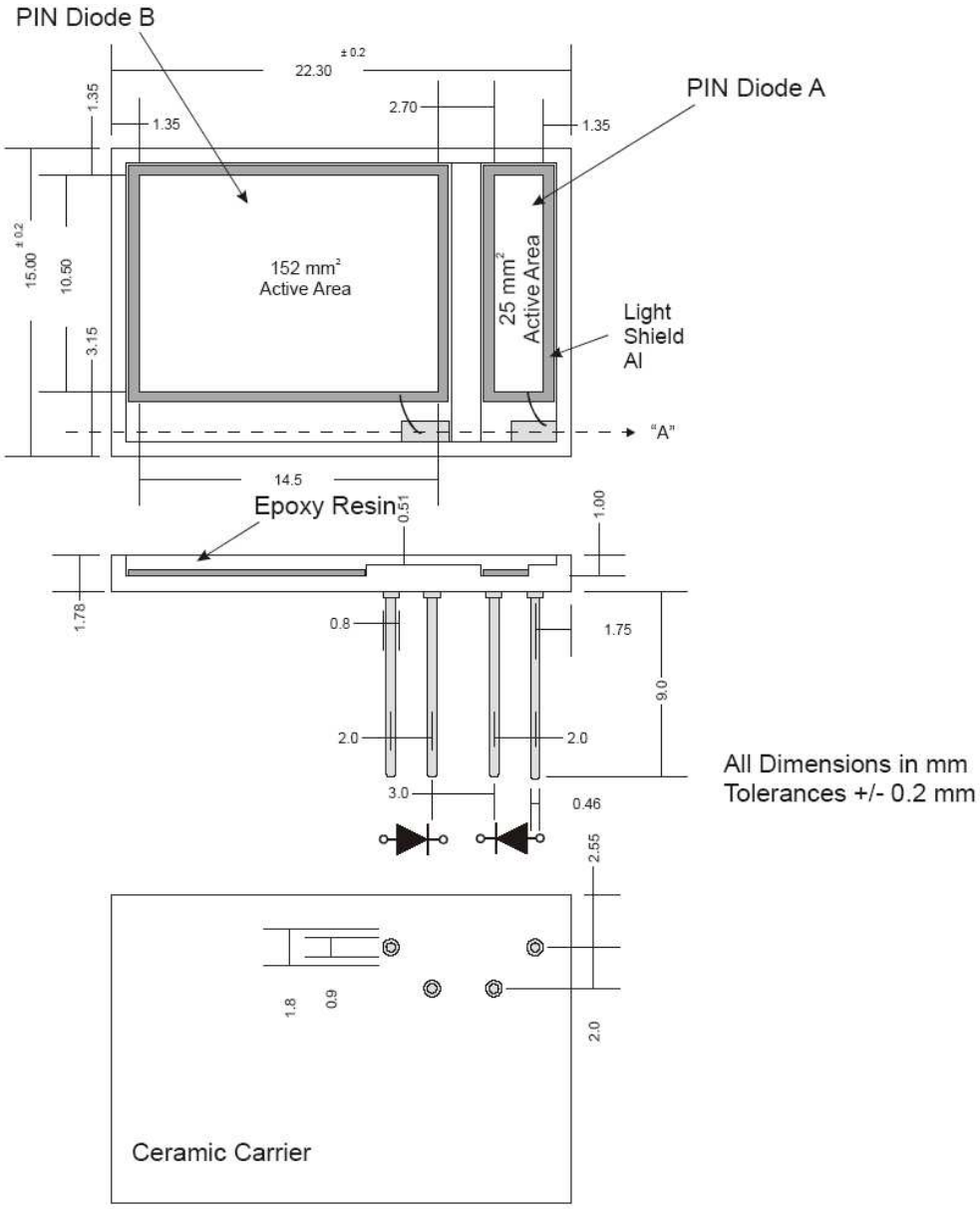

Figure 2.4: Detailed diagram, including dimensions, of a PIN photo diode. As used on the Gamma-ray Large Area Space Telescope (GLAST), two of these diodes were selected for use on the Pathfinder radiation monitor. Only the PIN diode B active area is used for the radiation monitor, with the A diode inactive. Taken from the LISA Pathfinder design document for the RM [29].

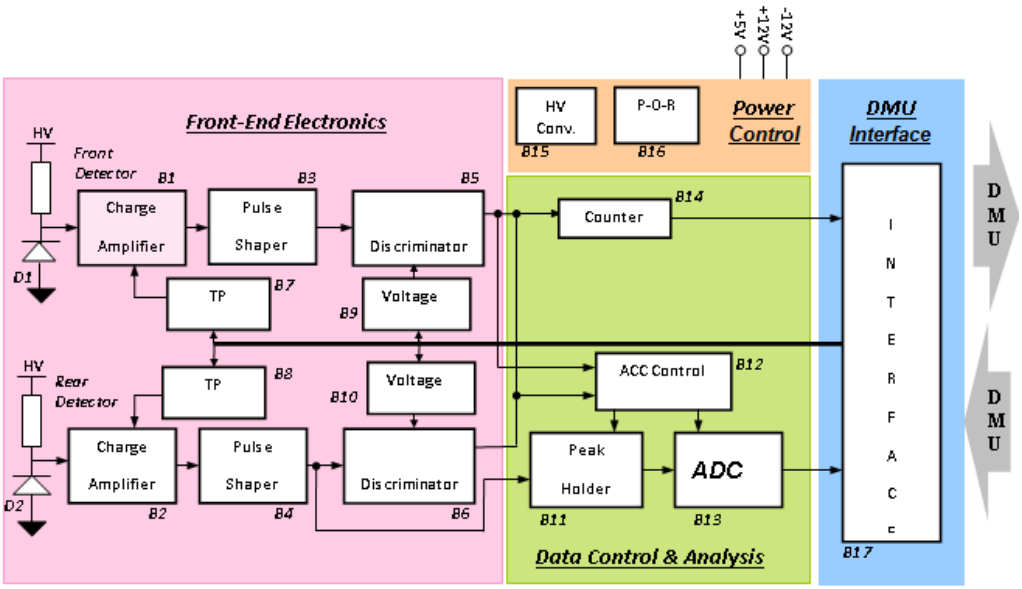

Figure 2.5: Flow chart showing the logic from photo diode to data management unit (DMU). It is estimated that the whole circuitry adds a total rms charge noise of around 1195e, corresponding to a deposited energy rms noise of around $\sigma_E \approx 4.24$ keV, using the average electron-hole pair creation energy of around $E_{Silicon} \approx 3.55$eV. It is also noted that there is an offset energy associated with the discriminator of less that 2.5 keV, which follows fabricant specifications. Diagram and approximate numbers taken from the LISA Pathfinder design document for the RM [29]

short signal from the diode and pre-amplifies, shapes, to typically 5μs, and then boosts the voltage. Only when the rising edge of the signal from B3 or B4 reaches a re-programmed threshold voltage, stored in B9 and B10, does the counter B14 register a hit from one of the discriminators B5 or B6 using a logical step into the counter (not displayed in the flow diagram). When this happens, the peak-holder B11 takes note of the active signal maximum voltage reached through the time the pulse travels through the circuitry. The reset circuitry then uses a capacitor to discharge the components, and resets the voltages in approximately 2μs.

When a signal passes this circuitry and is counted as a hit in both diodes, the energy deposited in the back diode is recorded using the voltage output from B6, and called a 'coincident' event. If only one diode registers a hit, the event is counted as a 'single' event in the counter B14, and the singles count is incremented by one. Coincident events are usually due to either secondary particles showering onto the second diode within a pre-determined window after the first diode registers its hit, or a primary particle passing through the RM with the correct angle to hit

both diodes. Singles events are stored as a time series sampled every fifteen seconds, while coincident events are stored as a two dimensional histogram of time and energy deposited in the 'back' diode every ten minutes.

Using the outline above, it is now possible to begin construction of a model for the on board processing. This will allow the conversion of a deposited energy spectrum to an estimate for the GCR flux on the test masses. The important parameters are the level of the electronic noise at the time of flight and the structure of the threshold setting process. These are important factors to take into account in the model as they will change the counts registered both in energy and number.

2.5 Modelling Deposited Energy Spectrum

This section develops a two stage model for the simulation of cosmic rays interacting with the radiation monitor, and the subsequent processing and vetting of hits. The first stage involves a GEANT4 simulation of the detector geometry and cosmic ray interactions with the surrounding material. The second models the on-board processing of count energy data using Matlab, and accounts for the effects of electronic noise and threshold noise.

2.5.1 GEANT4 for GCR Interactions in the Detector

The GEANT4 model randomly draws primary particles from a given GCR differential energy spectrum. Each sampled particle is stepped through the geometry of the monitor with a cross-section for an interaction according to a 'physics list'. Each cross section is based on the particle species and local detector material. This process is repeated until the number of sample particles requested is reached.

The detector geometry used is shown in Figure 2.6, where a 1.42 mm thick aluminium sphere centered on the monitor has been added to simulate the shielding from the surrounding spacecraft, as detailed by the General Design and Interface Requirements Specification [115]. Due to

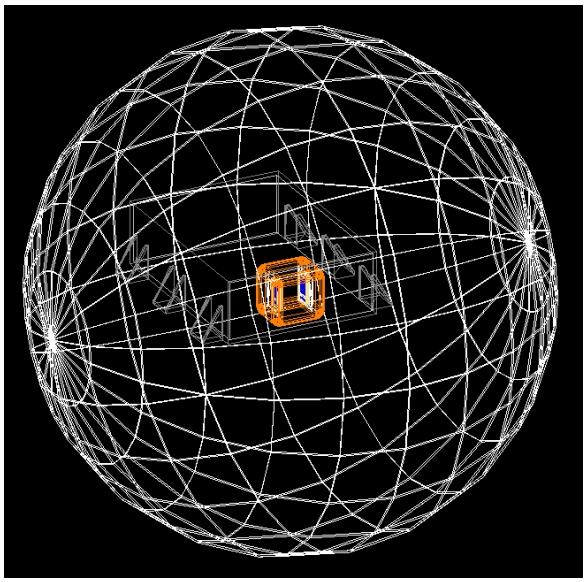

(a) Whole geometry used, including a large aluminium sphere centred around the radiation monitor to model the shielding by the surrounding spacecraft material. Also shown in grey is the aluminium box and feet that join the instrument to the surrounding spacecraft.

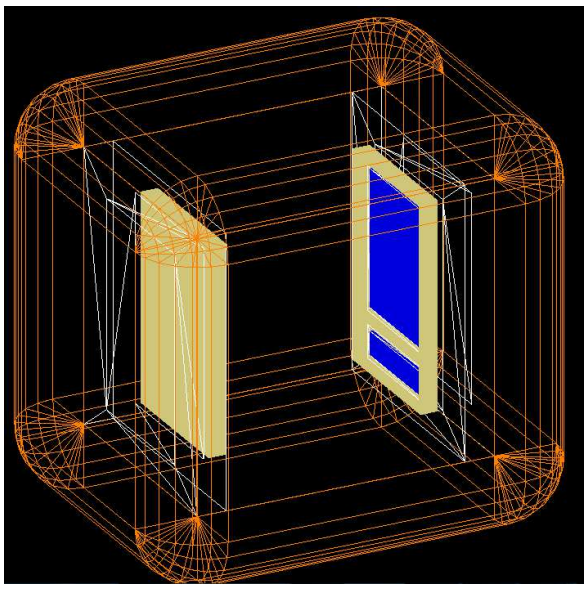

(b) Close up of the copper shielding around the two dual PIN diodes in a telescopic arrangement. The solid blue shows the two active areas used in the GLAST experiment, with only the larger area on each PIN diode active in the Pathfinder radiation monitor.

Figure 2.6: Radiation monitor geometric model used for the GEANT4 simulations of galactic cosmic ray radiation on spacecraft.

the sensitive regions of the diodes not being centred on their substrates (Figures 2.3 and 2.4) there is is a small lateral offset in the telescopic configuration which is also accounted for in the simulation. Also shown is the copper shielding around the diodes, located within a larger aluminium box mounted on the inside wall of the spacecraft. The image on the right shows a close up of the monitor, where the active regions are shown in blue and the ceramic substrate is shown in cream. Only the larger blue area is active which mirrors the flight RM.

When an interaction occurs in either of the two larger sensitive regions, GEANT4 records the energy of the primary particle sampled and the deposited energy in each diode. The detection regions are 152 mm^2 in area and 320 μm thick.

Once the simulation has been run for a particular GCR flux, the GEANT4 data are stored as a list of primary energy and deposited energies in both diodes. This then allows a two dimensional histogram to be made for the coincident events and primary energy, for example in Figure 2.7. Scaling each bin of deposited energy by the ratio of a proposed flux, parameterized

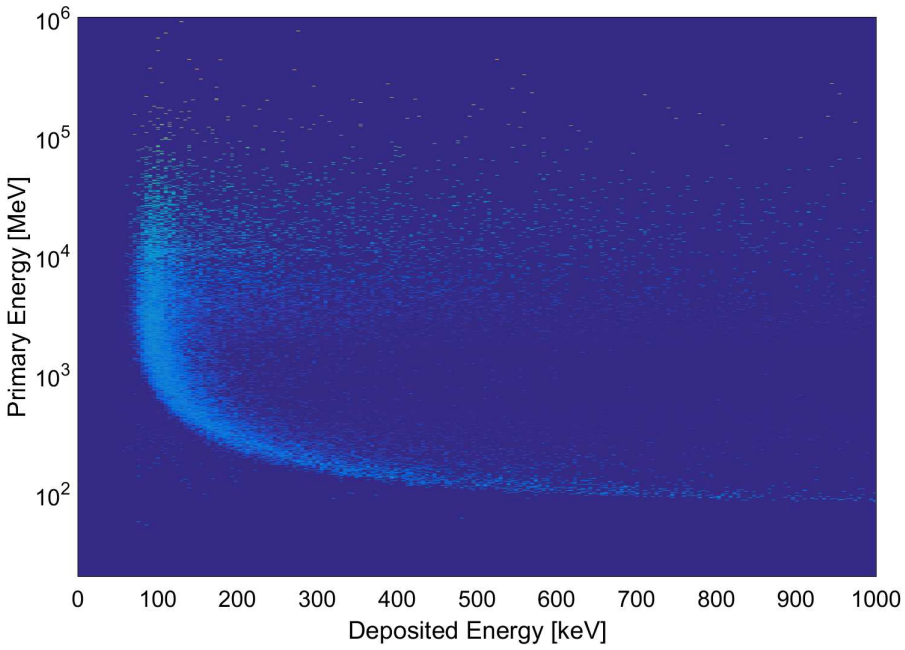

Figure 2.7: Example histogram of coincident counts from primary protons in a GEANT4 simulation with specific GCR flux. Taking each deposited energy bin, an array of factors of new flux divided by old flux can be applied to each bin of Primary energy to scale the GEANT4 data. This allows for faster fits for attenuation parameter as each proposed flux does not have to be run in GEANT4 separately. Notice also the broader scatter from higher energy primaries, which deposit energy both directly and by particle showers from interactions within the shielding.

by a proposed value of ϕ, and the flux used in the first run of GEANT4 provides an efficient scaling of the data instead of re-running this component of the model. This is essential when running the fitting process as typical run times for the GEANT4 component are several hours. Note that this stage of the simulation does not account for a threshold or electronics noise. If energy is deposited in the sensitive region(s) of the diode(s) as a consequence of an interaction anywhere in the simulated geometry, then that energy is recorded regardless of how small it is.

2.5.2 Matlab for On-Board Processing of Hits

A Matlab script processes the GEANT4 data according to a model for the electronics that handles the raw diode signal pulses on the spacecraft. Electronic noise is first added to each deposited energy, on each diode. It is assumed that this is Gaussian in nature, with a mean and variance to be determined, but assumed close to the pre-flight measurements. Calibration

pulses through the mission can be used to significantly constrain the values for these parameters, and will be discussed in more detail later.

Once the electronic noise is added to the hits, each deposited energy is then compared to a threshold energy to replicate the discriminator. The threshold, as a sourced voltage that is variable according to a commanded value, is not a clearly defined hard cut off at the commanded value. In all of the spectra there is some bleeding of hits below the nominal threshold, implying a variance. The exact character of this threshold is not known, and needs to be fitted for before the solar attenuation parameter can be extracted. The fitting algorithm is outlined later, and the results are described in chapter 3.

To implement the threshold model in the Matlab code, each hit is compared to a randomly generated threshold for that hit based on a trial model. The resulting list of hits that survive the threshold test are then binned into a histogram if both diodes record a hit, or summed to a count rate if only one diode records a hit. These correspond to the coincident and singles counts respectively.

2.5.3 Setting the Electronic Noise Parameters

As a first estimate of the change in mean and standard deviation of the electronic noise, a Gaussian was fitted to the top three bins in the main peak of the daily deposited energy spectra. Figure 2.8 shows an example days fit, with the Gaussian overlaid. Figure 2.9 shows the mean for each day with the associated errors and a linear fit to the drift. It can be seen that these parameters slowly drift through the Pathfinder mission.

The main peak shape, particularly the position, is determined by the energy deposited by a minimum ionizing particle, which is related to the thickness of the detector and corresponds to particles with energies close to the minimum in Figure 2.2. These higher energy particles, occupying the upper half of Figure 2.7, deposit energy primarily in the main peak on the left of Figure 2.7. Given that the thickness of the diodes does not change through the mission, the drift in peak position can only be accounted for by changing the mean of the electronic noise in the

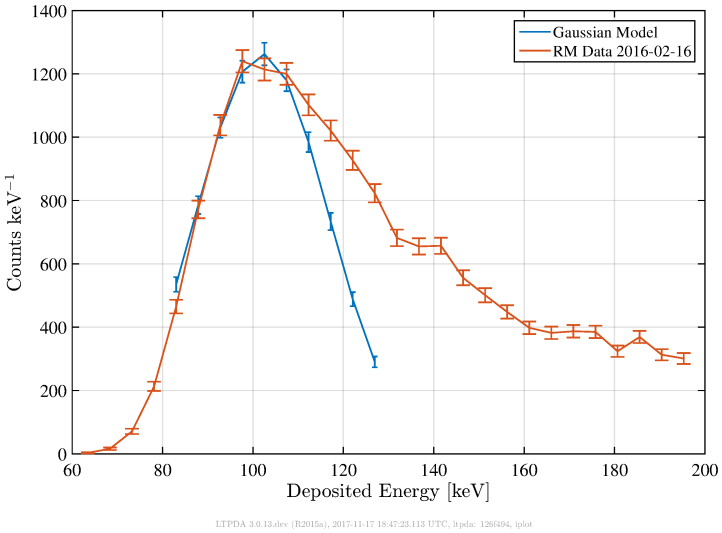

Figure 2.8: Gaussian fit (blue) to the top three bins of the main peak (red) to explore peak position and spread changes in time.

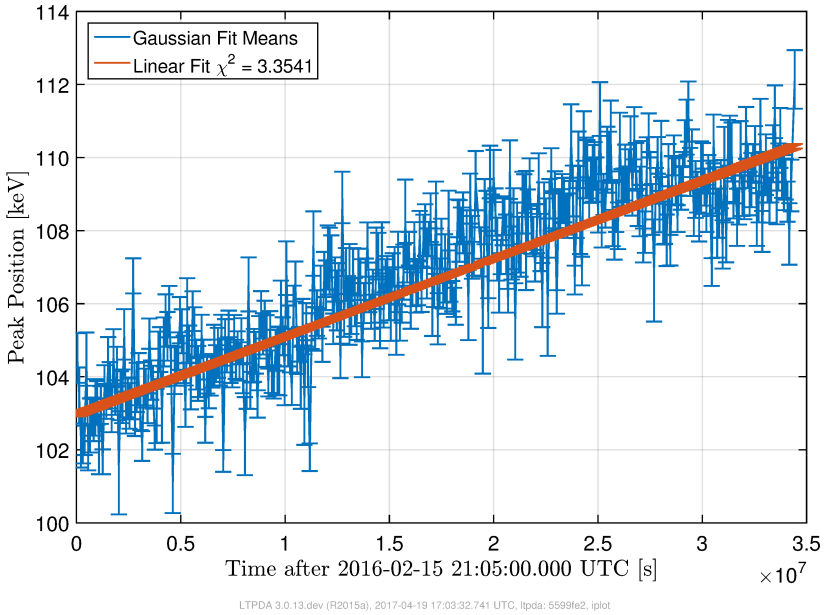

Figure 2.9: The results from fitting a Gaussian to the top three bins of the main peak in the deposited energy spectrum. This shows a slow drift through the LISA Pathfinder mission, suggesting that either the threshold parameters or the electronic noise is drifting in time. This must be accounted for in the final model for the radiation monitor on-board data processing.

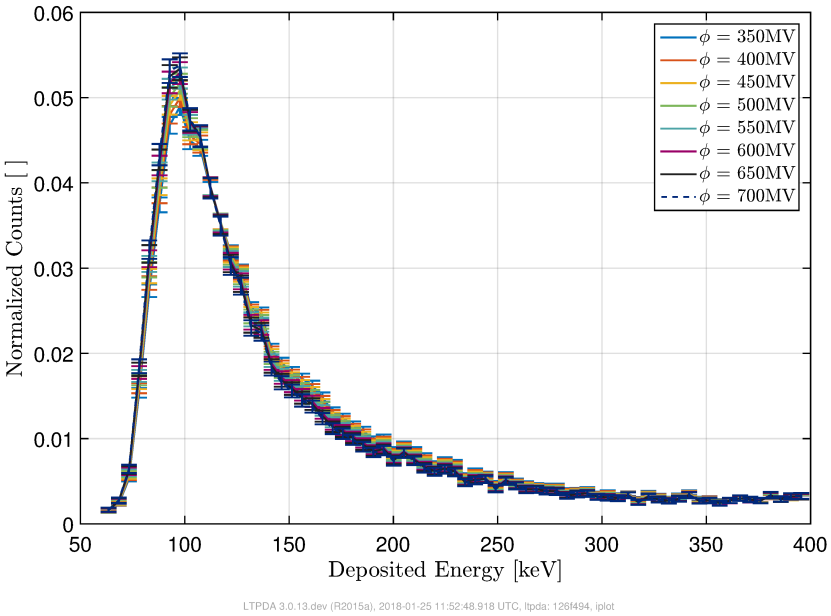

Figure 2.10: Normalized deposited energy spectra simulated using a range of solar attenuation parameters. Note the biggest effect is a broadening of the spectrum as the solar attenuation decreases. The position of the main peak does not change with the solar attenuation.

simulation. This is further demonstrated in figure 2.10, which shows a number of normalized spectra simulated for a range of solar attenuation parameters. The peak position does not change, but the spectrum does increase in spread slightly as the solar attenuation decreases. Therefore the peak position drift, and some of the change in spread, can be attributed to changes in the electronic noise and/or threshold shape.

This kind of degradation is expected for a RM like the one used in Pathfinder, and affect the data in different ways. A change in mean electronic noise will shift the whole spectrum while a change in standard deviation will broaden it. In order to further explore the degradation and account for the changes in electronic noise, the Gaussian fit was repeated for weekly test pulses. Injected at a variety of energies, a particular energy width can be defined to look at changes in the shape of the pulses. As with the main peak of the spectrum, these will correlate with changes in the electronic noise parameters assuming the injections are not changed through the mission.

Using the lowest energy pulses at around 140 keV, a Gaussian fit to the shapes over a few bins shows that not only is μ_E drifting but also σ_E^2 too. Figure 2.11 shows an example pulse and

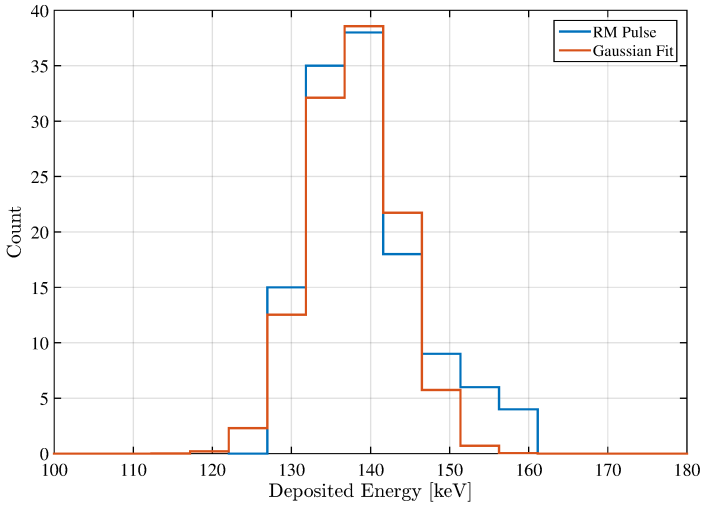

Figure 2.11: Example test pulse (blue) with Gaussian fit (red) to the electronic noise parameters μ_E and σ_E.

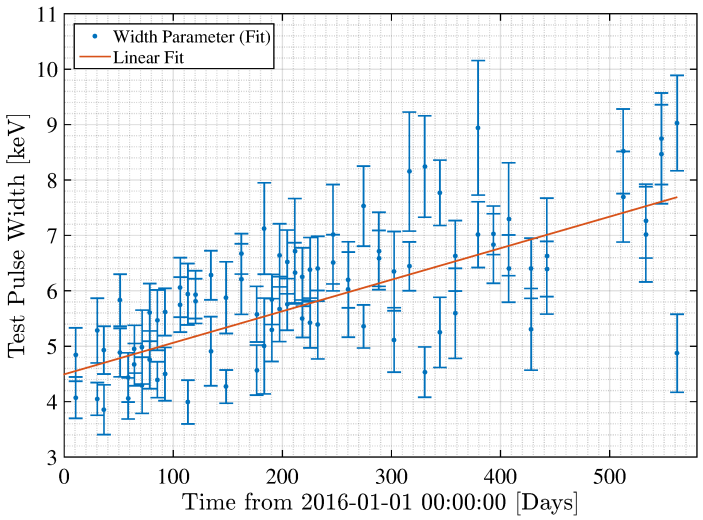

Figure 2.12: Inferred standard deviation of electronic noise. The start value was taken as 4.5 keV, in agreement with the technical note [29] plus a small additional noise to account for pre-flight degradation.

fit, with the full time series of both electronic noise parameters shown in Figures 2.12 and 2.13. Injections are cut from the spectrum, and the minimum bin count is subtracted from the pulse. This allows the pulse to be effectively removed from the main peak counts. Then the Gaussian is fitted using an rms fitting process. Since only the change in electronic noise parameters is being considered, the background trend due to the main peak counts can be ignored, assuming that it is roughly the same from day to day when pulses are injected.

Linear fits to the noise parameters are overlaid on the Gaussian fit results. These are used to estimate the electronic noise at any time in the mission by drawing a random number from a Gaussian distribution with parameters taken from the linear fits evaluated at the time under

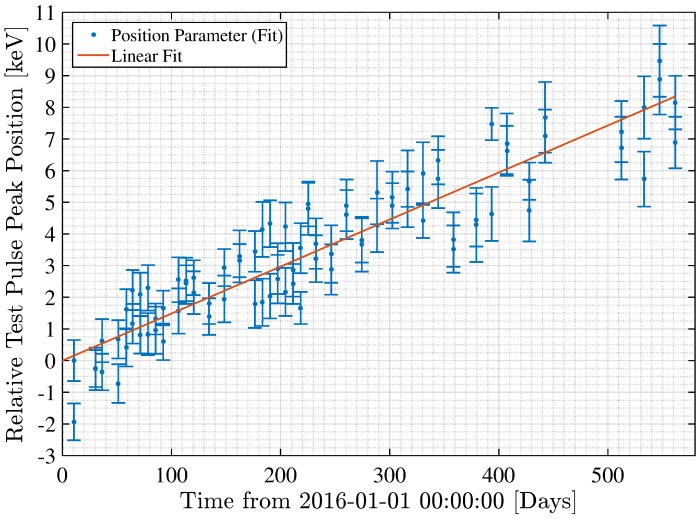

Figure 2.13: Inferred change in mean of electronic noise through the mission. The simulation sets the initial value using a calibration run from February 2016, and uses this result for the change in time.

consideration, and adding it to each recorded hit from GEANT4. Although the mean is assumed to start from 0 keV at the beginning of operations, the standard deviation can be extrapolated back using the linear fit. This suggests σ_E started from 4.5 keV, which is in agreement with the technical note findings of 4.24 keV with a small, additional degradation between testing and early flight [29].

2.6 Fitting the Threshold Distribution

Here, the procedure for fitting the parameters of a trial distribution for the threshold shape is outlined. It follows a Metropolis-Hastings algorithm so that posterior distributions for the trial model parameters can be obtained. The fit was performed on calibration data at the beginning and end of the mission, and the results of the fit will be shown in chapter 3 with the trial distributions used.

2.6.1 Likelihood Function

The likelihood function for the fitting algorithm assumes a log-normal distribution for the fitting parameter that compares one spectrum to another. This a good approximation if the number of hits in any bin used is larger than several counts. To see this, consider the likelihood function

given by

$$\mathcal{L} = P(N_D|N_S, \mu) \tag{2.5}$$

where N_D is the number of counts in a single bin of the measured data, N_S is the counts in the same bin in the simulation and μ is a known scaling parameter for the time of simulation to meet the same time span the experiment was run for (in this case one day).

Let $\vec{\theta}$ be the parameters of the model describing the threshold, and $\lambda = \lambda(\vec{\theta})$ be the true number of hits in the bin. The likelihood function can then be simplified by integrating over $\lambda(\theta)$ and using Bayes Theorem

$$\begin{aligned}\mathcal{L} &= \int P(N_D, \lambda|N_S, \mu)d\lambda \\ &= \int P(N_D|\lambda, N_S, \mu)P(\lambda|N_S, \mu)d\lambda \\ &= \int P(N_D|\lambda, N_S, \mu)\frac{P(N_S|\lambda, \mu)P(\lambda|\mu)}{P(N_S|\mu)}d\lambda\end{aligned} \tag{2.6}$$

Then, assuming bins with N_S and N_D both much greater than one, two simplifications can be made. First, the probability of N_D follows a Poisson distribution with mean λ. Second, $N_S \sim \lambda/\mu$, if the integration time is long, and therefore the probability distribution for N_S is another Poisson but with mean λ/μ. Using the latter, N_S can be taken as a function of both λ and μ in the $P(N_D|\lambda, N_S, \mu)$ term, and therefore neglected. Note that the denominator in the fraction is a scaling term independent of λ, and hence can be taken as a normalizing constant. Putting this all together, the likelihood function becomes

$$\mathcal{L} \sim \int \frac{\lambda^{N_D}e^{-\lambda}}{N_D!}\frac{(\lambda/\mu)^{N_S}e^{-(\lambda/\mu)}}{N_S!}P(\lambda|\mu)d\lambda \tag{2.7}$$

where $P(\lambda|\mu)$ is the prior on the true value, and is a strong function of the prior for the threshold parameters. In this analysis, this is taken as a uniform distribution, although it could also follow a normal distribution around N_D in the limit of a long experiment time.

Due to the assumptions made about larger counts in a bin for the likelihood function to apply, it is important to cut data below around 70 keV and above 1500 keV as outside this region the

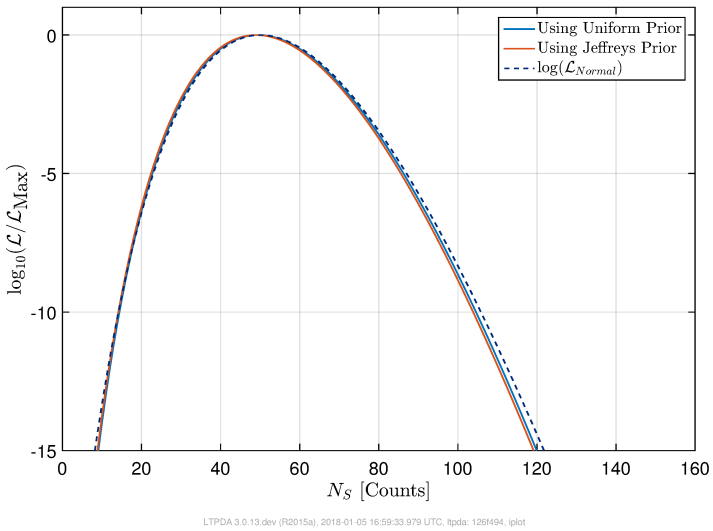

Figure 2.14: Testing the dependence of the likelihood function on the choice in prior. Both the uniform and Jeffreys prior show agreement with the Normal distribution, indicating this a good choice in selection statistic for the MCMC.

counts per bin are not enough. This cut, however, removes some bins that are most affected by the threshold as the nominal value is set to 60 keV throughout the Pathfinder mission.

Figure 2.14 shows how the log-likelihood changes as the number of counts in a bin changes. In this example, $N_D = 50$, and the log-Normal likelihood function is calculated using a χ^2 test statistic between N_D and a range of values for N_S assuming root-N errors. Two non-informative priors for λ are tested; a uniform distribution and a Jeffreys prior [79] defined on the assumption that $P(N_D|\lambda) \sim Poisson(\lambda)$. The latter takes the form

$$P(\lambda|\mu) \propto \sqrt{E\left[\left(\log\left(\frac{d}{d\lambda}P(N_D|\lambda,\mu)\right)\right)^2\right]} \propto \frac{1}{\sqrt{\lambda}} \tag{2.8}$$

Normalizing the likelihood functions by dividing by the maximum value, it can be seen that both the priors produce the same likelihood function. Furthermore, they are both in good agreement with a Normal likelihood function, with significant deviations occurring about 40 either side of the true N_D value. When N_D was changed to 10, the range of N_S where the agreement was as good was reduced to around 10 ± 4. This shows that the choice in prior is acceptable for this analysis, and that the normal likelihood function approximation is good.

2.6.2 Fitting Algorithm

The algorithm used is a simple Metropolis Hastings Markov Chain Monte Carlo method [91]. It samples a point in a given trial model's parameter space, calculates the coincident spectrum, then computes a log likelihood of the spectrum in comparison to the data. In this particular method, this is done using $\log(\mathcal{L}) \approx -\frac{1}{2}\chi^2$. Then it proposes a new point in parameter space, repeats the calculations, and then takes the difference between the new point and old point log likelihoods. If the difference is positive (new point more negative than old point) then the trial point is rejected, and the process is repeated. If the difference is negative (new point less negative than old point) then the trial point is accepted, and the process repeated but using the trial point as the old position in parameter space. The collection of accepted points forms the posterior distribution.

As the algorithm walks through the parameter space, it will gravitate to the region where the log likelihood is maximized. Given the definition of the likelihood function, this corresponds to finding the region of parameter space that has the greatest probability of reproducing the data observed. The procedure is optimized when the number of accepted points is approximately $25 - 40\%$ of the total number of points tested for a two dimensional parameter space. This is called the acceptance ratio, and is used to fine tune the stepping distribution that moves the algorithm from one proposed point to the next.

The stepping process randomly draws the next point in parameter space following a distribution that is chosen to reflect the knowledge about the parameters. This is the part of the algorithm that again takes into account the priors. The algorithm is most efficient when the stepping distribution most closely resembles the posterior distribution. In this case, the distribution is taken as a bi-variate Gaussian with no correlation for simplicity. The means are taken as the current proposal point, and the standard deviations are tuned until the acceptance ratio falls within the acceptable range.

Some of the points in the end posterior will be discarded as the Monte Carlo wanders through the parameter space before settling into the optimal region. Several attempts at the discarded

points can be used to tune the standard deviations of the stepping distributions. After removing these points, the posterior should be thinned as consecutive points are correlated with each other. The amount of thinning depends on the complexity of the stepping distribution, which for this case is fairly simple. Therefore only every other point is retained in the posterior chains.

In practice, it was found that, because at each trial step new thresholds and electronic noise were drawn, the statistic was fairly noisy relative to the sensitivity of the algorithm to global changes in statistic. Due to the adoption of uniform priors on the true value per bin, and therefore uniform priors on the threshold parameters, a grid was placed over the prior space and the statistic calculated at each point. The array of values was then smoothed and sampled from within the MCMC. This is in contrast to the fits for the solar attenuation parameter where the thresholds and electronic noise only had to be drawn once before the fitting, and hence the statistic was much less noisy.

This process was used to both quantitatively and qualitatively assess a model's ability to reproduce the calibration data. The existence of a global model, where the posterior distributions of parameters for a number of calibration spectra all agree with one another, is weighted heavily in the assessment. Ideally, one or more models tested would be able to reproduce the whole data set for one value per parameter.

2.7 Electrostatic Noise and Measuring Charging Rates

Once the thresholds have been found, and ϕ has been extracted through the mission, it is intended that a connection be drawn between the GCR flux and TM charging rates. However, in order to correlate charging with ϕ, it is important to understand how charge induced acceleration noise arises.

Energy deposited by incident cosmic rays predominantly ejects electrons, moving them from housing to test mass and vice-verse. This leaves the test masses with residual charge that can build up over time, creating stray forces on the test masses as their metallic faces have a

capacitance with the metallic housing. As the charge grows in time, so too does the parasitic force [11].

Consider a charged TM with no applied voltage. Given that the test mass has a capacitance with the housing, the stray electrostatic forces arising from the charge can be calculated. A stray force in the x axis F_x due to a charge q on the test mass is given by

$$F_x = -\frac{\partial U}{\partial x} = -\frac{\partial}{\partial x}\left(\frac{q^2}{2C_{tot}}\right) = \frac{q^2}{2C_{tot}^2}\frac{\partial C_{tot}}{\partial x} \tag{2.9}$$

where U is the energy in the system and C_{tot} is the total capacitance between the test mass and housing. Expanding in higher derivatives of the total capacitance, the force is given by

$$F_x = \frac{q^2}{2C_{tot}^2}\left[\left.\frac{\partial C}{\partial x}\right|_{x_0} + \delta x \left.\frac{\partial^2 C}{\partial x^2}\right|_{x_0} + \ \ldots\ \right] \tag{2.10}$$

where δx is the displacement of the TM from its equilibrium position at x_0. In this equation, the variable δx changes in time, causing F_x, and therefore the TM acceleration, to have a Fourier component contributing to the total acceleration noise of that TM.

Now consider the case where the charge q is allowed to vary. The total force in the x axis is now dependent on both the change in the total capacitance as the displacement δx changes, and the change in charge over time. The differential relation

$$dF_{x,tot} = \frac{\partial F_{x,tot}}{\partial q}dq + \frac{\partial F_{x,tot}}{\partial x}dx \tag{2.11}$$

shows the dependence on these parameters.

Finally, consider the case of a TM with variable charge q giving rise to a DC TM potential V_{DC}, a variable position δx and a sinusoidal applied voltage V_S. The component V_S is called the dither voltage, and is used to measure the charge through the response of the TM acceleration to the injected signal. The signal is applied at a frequency ω, while the force authorities (suspension voltages holding the TMs in place in all other degrees of freedom) are applied at audio frequencies, and hence can be ignored as measurements are processed in the mHz region.

The energy stored in the effective capacitor between the test mass face and electrode housing is given by

$$U = \frac{1}{2}C_{tot}\left(V_{TM} + V_S\right)^2 = \frac{1}{2}C_{tot}\left(V_{TM} + V_0 \sin \omega t\right)^2 \tag{2.12}$$

As before, the force due to the energy in the effective capacitor is given by

$$F_x = -\frac{\partial U}{\partial x} = -\frac{1}{2}\frac{\partial C_{tot}}{\partial x}(V_{TM}^2 + 2V_{TM}V_0 \sin \omega t + V_0^2 \sin^2 \omega t) \tag{2.13}$$

Increasing orders of derivatives of the capacitance were measured on ground from the central position in the housing. Hence it can, as before, be taken as a Taylor series. For the applications here though, this is not important and so it is left in the form above.

Using the double angle formula and grouping into terms that oscillate in response to the signal and terms that do not, the force can be re-written as

$$F_x = -\frac{1}{4}\frac{\partial C_{Tot}}{\partial x}\left(T_{DC} + T_{AC}\right) \tag{2.14}$$

where $T_{DC} = 2V_{TM}^2 + V_0^2$ and $T_{AC} = 4V_{TM}V_0 \sin \omega t - V_0^2 \cos 2\omega t$.

When the power spectral density is taken of the acceleration of the test mass with the dither, the response to this force will present two peaks in frequency space. One at ω, with amplitude proportional to $V_0 V_{TM}$, and one at 2ω, with amplitude proportional to V_0^2. After dividing by the mass, the remaining proportionality can be incorporated into the fit for V_0 and V_{TM}.

Converting V_{TM} to charge using the total capacitance C_{tot} as measured in the neutral position, the ω response to the force then becomes proportional to the charge. Dither voltages can be implemented in any degree of freedom of the TMs, however the optical readout is in x and ϕ_{TM}, where ϕ_{TM} is the angle of the TM around the z axis perpendicular to the spacecraft solar array, and so injections are made in these axes to make use of the full interferometer sensitivity. The derivation for dither in ϕ_{TM} follows as before but derivatives are taken with respect to the angle. In the angular injection case, the response will take the form of a torsion oscillator with some spring constant proportional to V_{TM}.

There are then two methods to convert a charge measurement to a charging rate. The first uses a time derivative of the charge measurement, and offers a continuous measurement for as long as the dither voltage lasts. This does, however, require a long signal injection which is not always possible. The second method uses subsequent, shorter charge measurements. This offers an averaged charging rate between the charge measurement times but is only valid if the configuration of the spacecraft, for example applied voltage actuation on the test masses, is unchanged between the two charge measurements. This is usually not the case as experiments on LISA Pathfinder require a perturbation to one environmental variable while measuring the response.

2.8 Discussion

A parameterization for the attenuation of galactic cosmic rays is outlined. This model includes a more modern LIS function, reflecting developments from Voyager data. Obtaining daily estimates for this parameter through the Pathfinder mission will be the goal of chapter 3, where the model is applied with the fitting algorithm also detailed in this chapter.

Also presented in this chapter is a two stage model for the RM. It develops existing GEANT4 code to simulate the interactions of energetic particles impinging upon the spacecraft and TMs, and has a second Matlab component to process the raw GEANT4 data in a similar fashion to the on board processing of hits from the RM.

As a first step to reducing the number of free parameters in the model, the electronic noise, which includes a dark current and capacitive noise, was set as a Gaussian. The mean and standard deviation for which were set by fitting Gaussians to a series of test pulses injected weekly through the mission into the RM. The values were found to be reasonably in agreement with estimates from ground tests.

In order to fit for the daily estimate of ϕ through the mission, the characteristics of the threshold of the diodes must be known. To provide a model for these, a fitting algorithm was outlined that takes a trial set of parameters, runs them through the RM model, and produces a trial

spectrum that is compared to a measured spectrum. By iterating this process many times in a Metropolis-Hastings MCMC process, posteriors may be drawn for a trial distribution shape for the thresholds. It was found that the likelihood function was very Gaussian in character, and therefore a simple χ^2 test statistic may be used. The results of this fitting process, the data used for the fit, and the models tested will be detailed in chapter 3.

Once the threshold has been fitted, ϕ may be extracted from the nominal data. The mechanism for measuring charging rates was described along with a brief discussion of the origins of electrostatic parasitic noise on Pathfinder. The purpose of this analysis is to outline a method to link the deposition of energy in the RM by energetic particles with the flux of GCR particles outside the spacecraft. Providing the solar attenuation parameter, as a proxy for GCR flux, through time will lay groundwork for the connection between GCRs and TM charging rates through the mission.

Chapter 3

Estimating Galactic Cosmic Ray Flux During the Pathfinder Mission

3.1 Introduction

In Chapter 2 a simple model for the Radiation Monitor (RM) was outlined so that the solar attenuation parameter ϕ may be estimated throughout the LISA Pathfinder mission. In this chapter, the threshold is characterized by comparing three distributions using the algorithm detailed in chapter 2. The solar attenuation parameter is then extracted form the RM nominal mission data as a time series of daily estimates.

During the Pathfinder mission there were two calibration runs that varied the nominal energy threshold of the RM in steps of 20 keV for a day at a time. The first run set the threshold at 20 keV, 40 keV, 60 keV, 80 keV, and 100 keV, while the second run set the thresholds at 60 keV, 20 keV, 40 keV, 80 keV, 100 keV, 120 keV, 100-60 keV, 60-100 keV, and 60 keV, where two numbers denote the front and back diode thresholds respectively.

Using these data, three threshold distributions will be fitted to the first set of calibration data, and then verified using the second set. An attempt will also be made in this chapter to discuss the correlation of measured charging rates with ϕ.

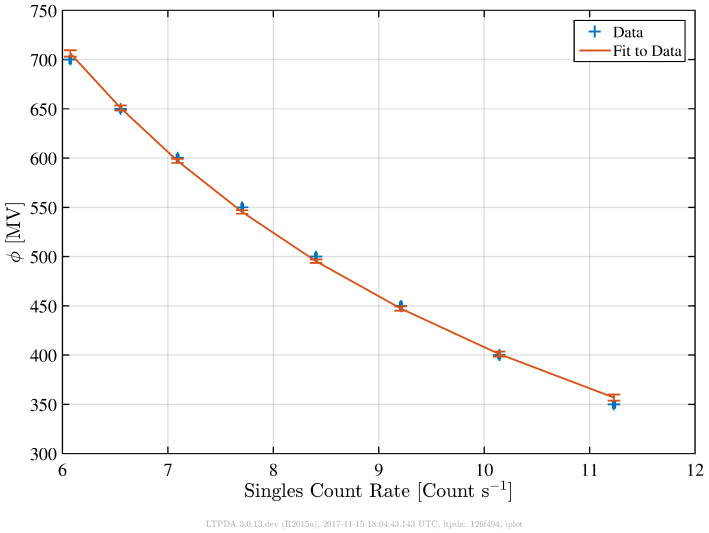

Figure 3.1: Correlation between the singles count rate predicted by the GEANT4 simulation for a range of solar attenuation parameters run in GEANT4. The red line shows a polynomial fit to the data for a constant plus inverse singles count rate. This will be used for a first estimate of the solar attenuation parameter for a selection of days through the LISA Pathfinder mission.

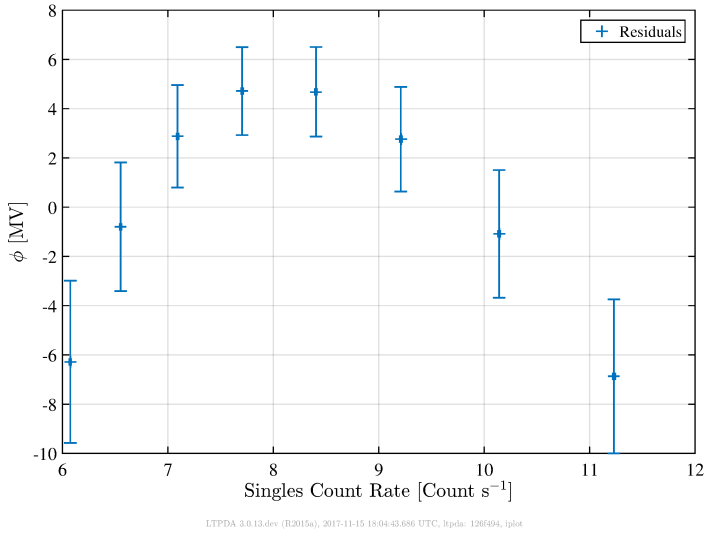

Figure 3.2: Residuals after fitting a polynomial to the correlation between solar attenuation parameter and predicted singles rate in the GEANT4 simulation.

3.2 Singles Count Rate for First Estimate of ϕ

The first estimate for ϕ can be inferred from a correlation between the simulated singles count and the attenuation parameter used in GEANT4. Choosing a range for ϕ that would be expected from the epoch of solar cycle that the nominal mission took place in, it is possible to fit for a one-to-one relationship between the singles count rate and ϕ, as seen in Figure 3.1. The residuals from the correlation function fit and the simulation data are shown in Figure 3.2.

There is good agreement using an inverse correlation, with at most 2% deviation between the correlation function's prediction of the count rate and the true count rate from the GEANT4

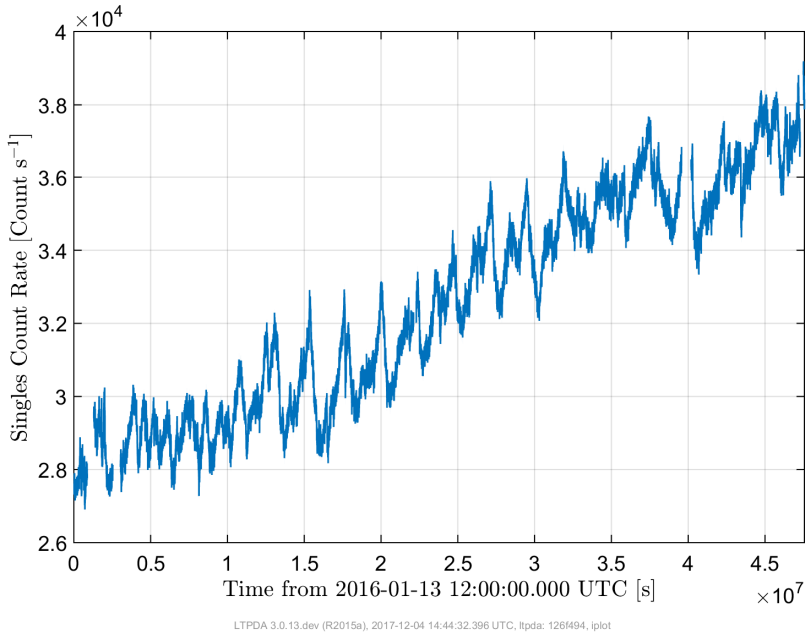

Figure 3.3: Hourly averaged singles count rate measured by the LISA Pathfinder radiation monitor.

simulation. Figure 3.3 shows the hourly singles counts through the mission measured by the monitor. At the end of the mission there was a small solar flare event whose particles were not energetic enough to penetrate the spacecraft. However, there is indication of a Forbush decrease after the flare in the last few points of the singles data as the count rate decreases significantly [116]. Evaluating the model at these counts, this time series can be turned into a time series estimate for the value of ϕ through the mission, as shown in Figure 3.4.

3.3 Fitting the First Calibration Run Spectra

In February 2016, a week long calibration run was carried out to characterize the thresholds. For a day at a time, the threshold was varied in steps of 20 keV, from 20 keV to 100 keV, see Figure 3.5 for a close up of the spectra. When the threshold was set to 20 keV and 40 keV the main peak, to the right of the noise peak, did not change. This suggests that the threshold was low enough to not attenuate the hits in this region of the spectrum. The data also underline the need for a 'soft' threshold, as the counts visibly bleed below the commanded threshold. For example, in the 100 keV data the main peak reaches down several bins below 100 keV.

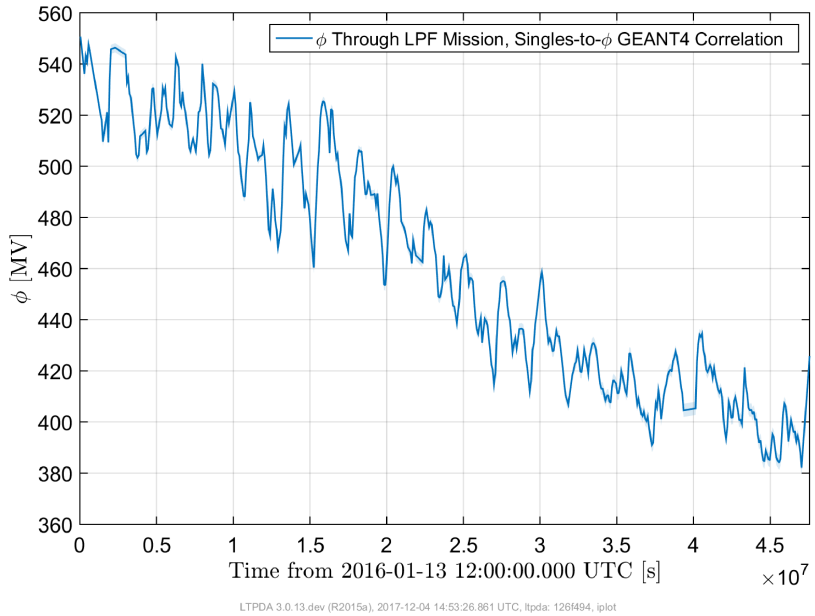

Figure 3.4: Resulting time series for solar attenuation parameter after correlating predicted singles count rate with ϕ input to GEANT4 model. This used a hard cutoff threshold at the nominal value, and is expected to give systematic errors around 10% due to noise hits neglected in the model.

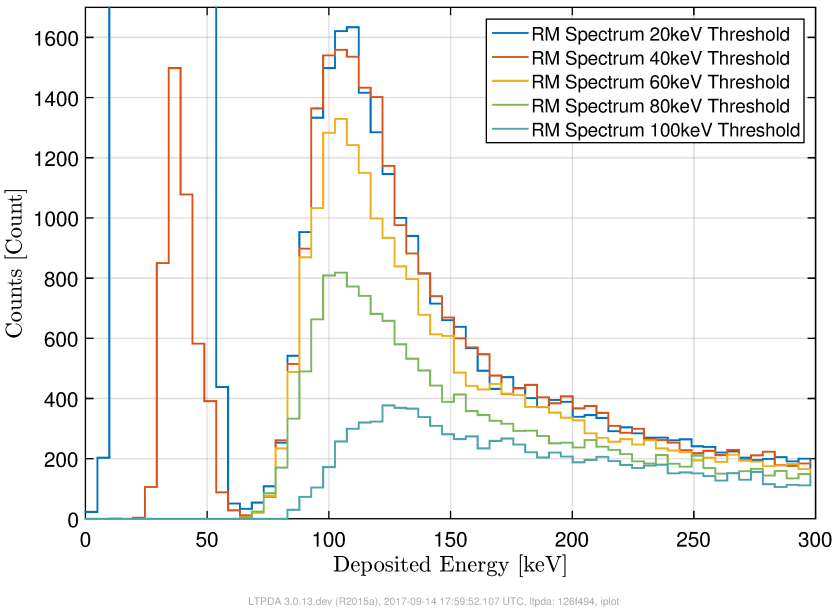

Figure 3.5: Calibration run data from mid-February where the threshold was varied from 20 keV to 100 keV in steps of 20 keV. The left peak shows the noise-noise hits while the right peak shows the main peak where hits occur from electron-hole pairs created by passing energetic particles.

There are many models for the threshold shape to choose from, ranging in number of parameters and complexity. To mirror the electronic noise parameters, the origins of which are likely similar to the origins of threshold noise, the three simplest models are chosen for the fits. These are a single Gaussian describing both diode thresholds, a double Gaussian in which the standard deviations are equal and set but two means are allowed to vary, and finally, a Gamma distribution with common parameters for both diodes that more closely reflects the shape of the deposited energy spectra.

Each model will be evaluated in a fit for the relevant parameters, and qualitatively assessed for a global model. The end goal is to find a set of parameters in at least one model that can reproduce all of the calibration spectra. The value of ϕ is assumed constant through the calibration data, and fitted for using the 20 keV data, where the threshold is assumed low enough to not affect the data above 60 keV where the fit is performed. Noting that the peak in the 40 keV data is unchanged from the 20 keV data, this would seem to be a good assumption.

3.3.1 Single Gaussian Model

The simplest of the three models tested was the single Gaussian, in which a single Gaussian distribution is used with common parameters to both diodes. This would consist of a fit for a mean μ_T and standard deviation σ_T denoting an offset from the nominal threshold value and a spread.

Many components in electronics exhibit Gaussianity, and in the limit of many draws the central limit theorem says the distribution would approach a Normal. It makes sense then to attempt to fit this model to the data.

After running the MCMC, Figure 3.6 shows an example posterior distribution with a normal fit to the binned chain. Although the distribution is noisy, likely a result of the noisy statistic relative to global changes, a Gaussian can still be fitted to find the mean best fit value, and a 1σ error bar in both parameters.

Repeating this process for all three data sets, the resulting means are shown together in the

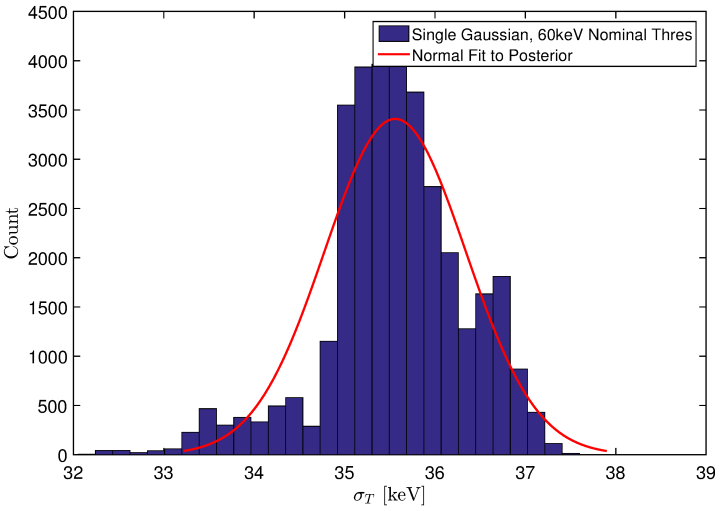

Figure 3.6: Example posterior distribution for one of the fit parameters (blue), with a Gaussian fit overlay. The distribution is noisy, with variations between bins more than $\sqrt{N}$, likely a result of the drawing processes from trial point to trial point. The Gaussian still captures the spread and mean, and so is used as a proxy for the posterior value and corresponding uncertainty.

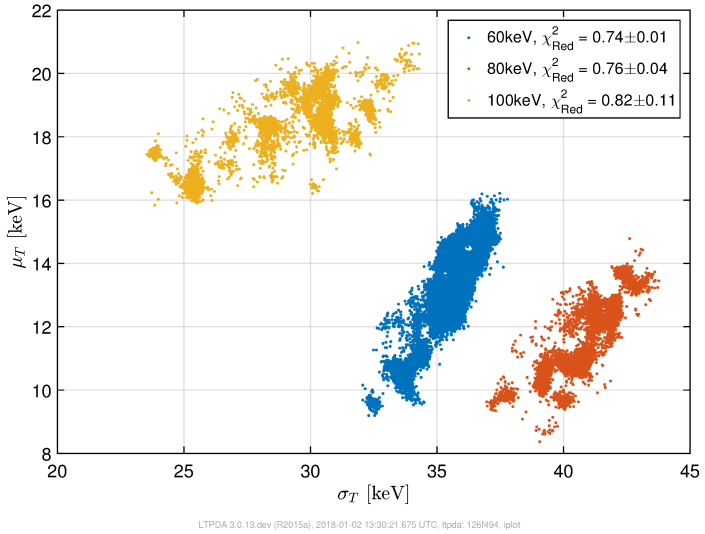

Figure 3.7: Posterior chains for the three data sets at 60 keV, 80 keV and 100 keV commanded thresholds. The reduced χ^2, χ^2_{Red}, are shown in the legend, which have been diluted due to the large number of bins between 1000 keV and 1500 keV. Note the noise in the grid of statistic values is seen in the clusters of points in each chain.

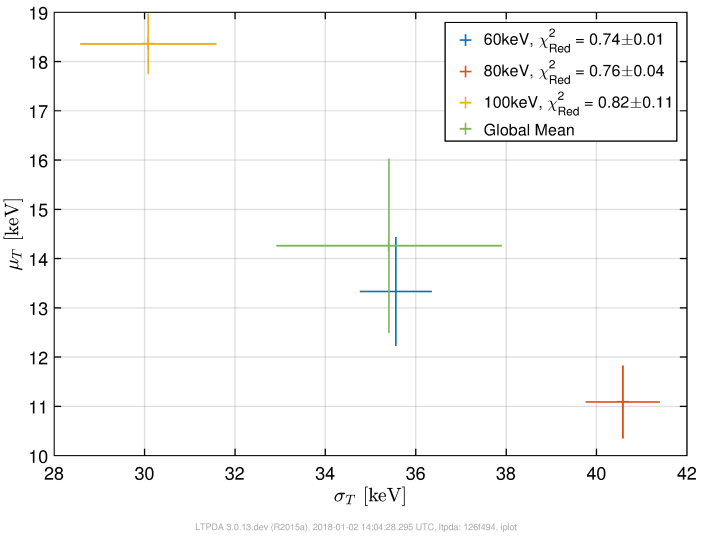

Figure 3.8: Mean posterior values and corresponding 1σ uncertainties obtained by fitting a Normal distribution to each posterior chain. This is done for one parameter at a time by marginalizing over the other parameter before fitting a normal to the resulting distribution. The green cross indicates the global model calculated by averaging over the three model means.

parameter space in Figure 3.7. All three fits exhibit agreement with one another to within a few standard deviations. This shows that a global model is plausible that explains all three data sets with just one value for both the offset and standard deviation. The values of these global parameters and their 1σ errors are shown as the light green cross, with values $\sigma_T = 35.4 \pm 1.8$ keV and $\mu_T = 14.3 \pm 2.5$ keV for the spread and offset from the nominal threshold.

Note the small values of χ^2_{Red}, the reduced χ^2 statistic, obtained by dividing the mean fitting algorithm statistic from the posterior chains by the number of bins being used in the fits. Since the upper portion of the fitting range is more affected by the solar attenuation parameter than the threshold, the simulations and data counts converge at higher bins. There are many more bins above 10^3 keV than below it in the range used for the fits, and so the reduced statistic is diluted as the fractional difference between simulation and data bin counts is much lower here than in the lower portion of the spectrum. This effect is not important in the fits as it is the change in χ^2 statistic between trial parameter values that the algorithm utilizes.

3.3.2 Double Gaussian Model

The second model tested uses an independent Gaussian for each diode, with separate offsets from the nominal threshold but a common standard deviation set to 10 keV. The value of the standard deviation was hardwired in the fits in order to reduce the number of fit parameters

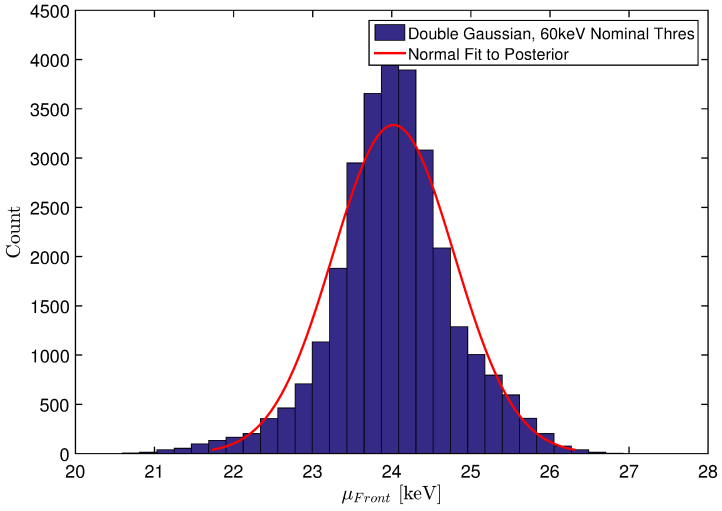

Figure 3.9: Example posterior distribution (blue) for the double Gaussian model parameter μ_{front}, representing an offset of the front diode from the commanded threshold. Gaussian fit to distribution overlay (red) giving the mean fit value and corresponding 1σ uncertainty.

while mirroring the observed order of magnitude spread in the electronic noise. Due to the noisy statistic, three dimensional fits were found to be highly inefficient and costly in computational time.

A fit was performed for the front and back diode offsets, μ_{Front} and μ_{Back} respectively. Figure 3.9 shows an example histogram of the posterior for the μ_{Front} parameter on the 60 keV day. Overlay is the Gaussian fit to the distribution (red). Although the posterior is less noisy than the single Gaussian model, the back diode offset for the 60 keV fit, shown by the blue points in Figure 3.10, presents an interesting result with a spread from 20 keV to below the cut on the data around 60 keV. This meant that the spread in theory could extend to negative infinity, as there is no data to give information on a threshold in this range. This suggests that for this model to work for these data, the back diode must accept all events as a count. The front diode is then responsible for the attenuation as it has a well defined region of acceptable values for its offset, placing it above the cut on the data.

Another interesting point is the spread of posteriors for the three days, shown as three independent clouds of points in Figure 3.10. Although the 80 keV and 100 keV data agree with one another to within a bin width, the 60 keV data presents a tension for a global model found at $\mu_{Back} = 22.0 \pm 7.1$ keV and $\mu_{Front} = 7.0 \pm 7.1$ keV. Indeed looking at the posterior mean values and the average of the means for a global mode, shown together in Figure 3.11, the green cross

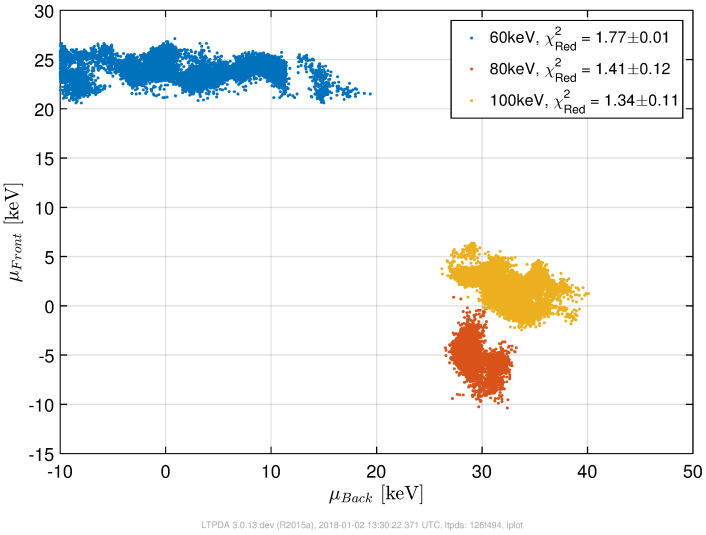

Figure 3.10: Posterior chains for the double Gaussian model. The 60 keV data presented an interesting result as the back diode offset was unbounded from below. This suggests that it affects the spectra more than the front offset as it is limited below the cut of data. The front diode is then pushed much higher to attenuate the peak to the measured level.

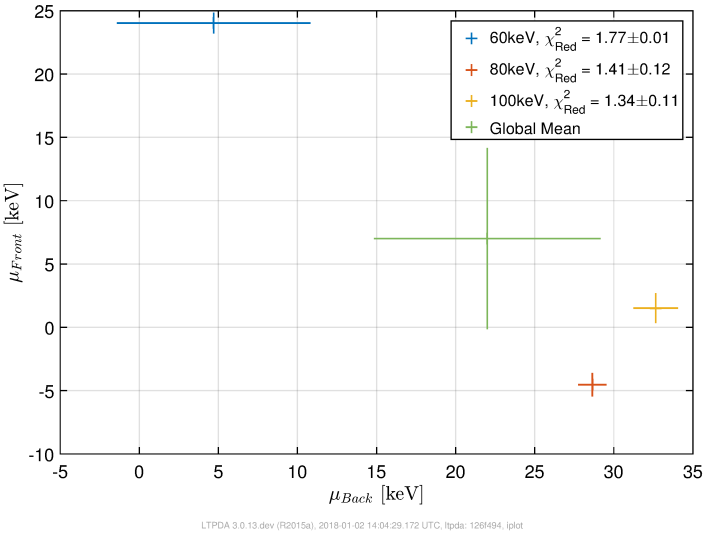

Figure 3.11: Posterior means and 1σ uncertainties for the three data sets in the double Gaussian parameter space. The green cross indicates the mean of the three fit results, giving the global parameter models.

indicating the global model spans a large area relative to the single Gaussian global model. In fact, the error bars span a range in both dimensions more than three or four times the range in the single Gaussian case. This indicates that the global solution is under-constrained in this model.

3.3.3 Gamma Model

The third and final model to fit was a single Gamma distribution describing both diode thresholds. This is motivated by looking at the ratio of the difference between the 60 keV and 20

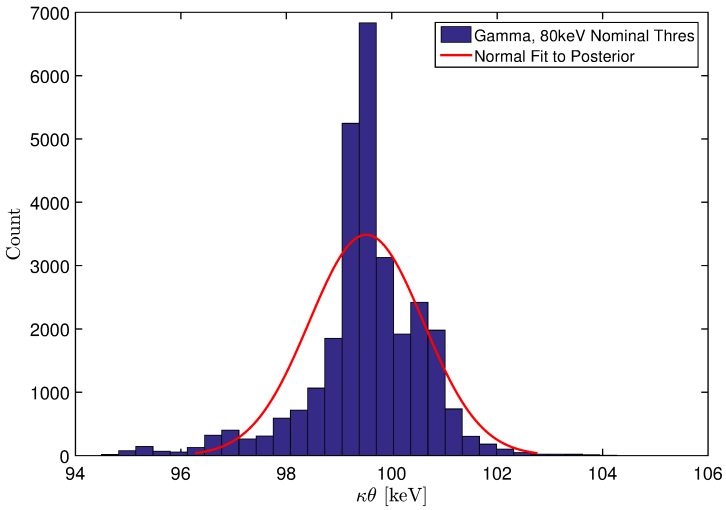

Figure 3.12: Example posterior distribution for the $\kappa\theta$ combination of parameters fit (blue). The red curve shows the Gaussian fit to the distribution giving the mean and 1σ uncertainty for the parameter.

keV data and the 20 keV data. It shows that the change in counts in each bin in the fitting range is similar to the shape of the initial distribution itself. The simplest distribution to give a shape with a main peak and extended upper tail, which also satisfies the principle of maximum entropy, is a Gamma distribution.

A Gamma distribution is determined by two parameters κ, a dimensionless value that governs the shape, and θ, with units of keV, whose product with κ gives the mean of the distribution. It was found in preliminary fits that these two parameters exhibited a high degree of correlation between each other, and so the fits were performed for κ and $\kappa\theta$.

Figure 3.12 shows the $\kappa\theta$ posterior distribution for the 80 keV data. The distribution is fairly noisy, but the Gaussian fit (red) still captures the spread of the distribution and the approximate mean, which centres about 20 keV above the nominal threshold of 80 keV.

Figure 3.13 shows how the posterior chains compare between the three fits in $(\kappa, \kappa\theta)$ space. The mean of the distributions, $\kappa\theta$, was found to be approximately 10 keV above the commanded threshold in all three cases. The shape parameter κ, however, did not exhibit a global trend in the data. Typically, this parameter takes a low value, but is defined as positive in the definition of the distribution. Hence, the fitting range only considered values for this parameter in the range $(0, 100)$.

The 80 keV data shows some tension with the other two data sets. This is demonstrated in

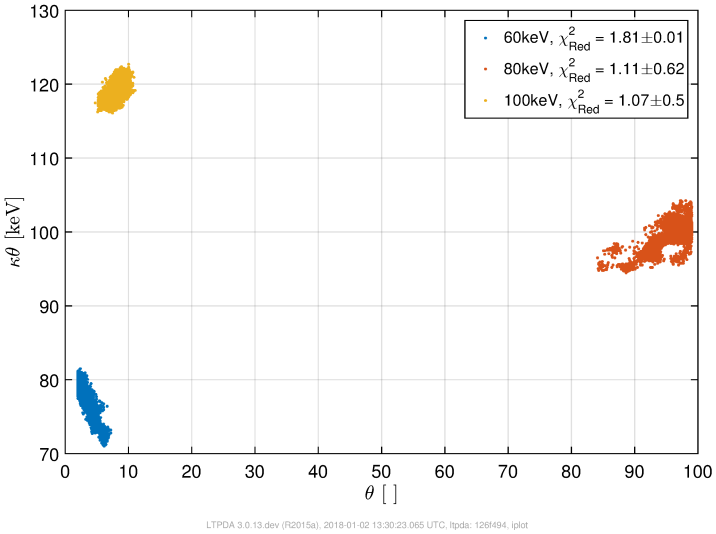

Figure 3.13: The three posterior chains for the Gamma distribution thresholds. All three present tension with one another, with the 80 keV results giving a higher than expected results for θ. Note that the $\kappa\theta$ combination gives the mean of the distribution, and is therefore expected to increase from spectrum to spectrum as the commanded threshold increases.

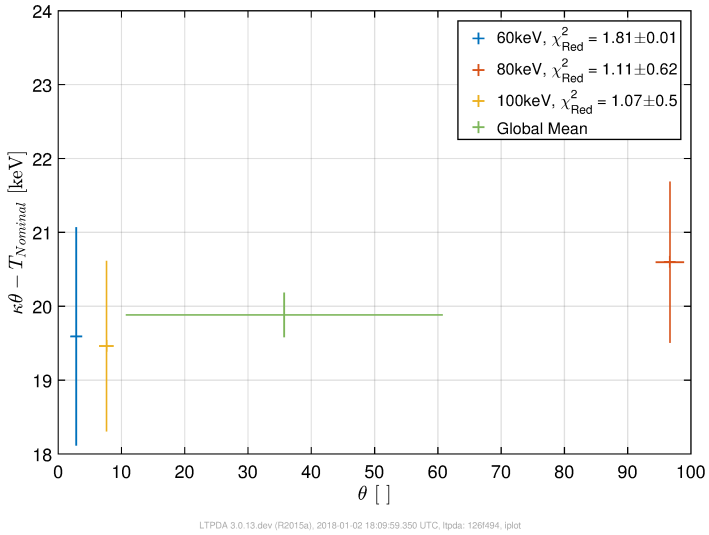

Figure 3.14: The mean parameters values and their associated 1σ uncertainty from the fits. Note that the $\kappa\theta$ combination has had the commanded threshold subtracted in order to gauge the offset form the nominal value. All three data sets agree in offset but present a great deal of tension in the shape parameter θ. The green cross shows the global model after averaging all three fit results.

Figure 3.14, where the global solution (green) extends a large range in the θ axis 36 ± 25. The combination $\kappa\theta$ has had the nominal thresholds subtracted in this plot to demonstrate that all three data sets agree in this fit result, with the global model, 19.88 $keV \pm 0.29$ keV, extending only a fraction of a bin width.

3.3.4 Global Model Predicted Spectra

In order to qualitatively assess the global models inferred from each distribution tested, the spectra produced at each of the three commanded thresholds were plotted with the measured

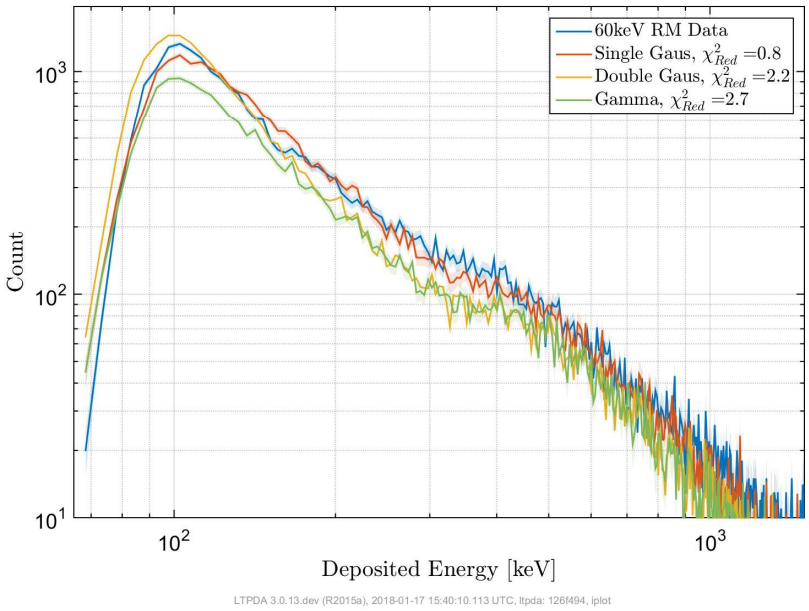

Figure 3.15: Predicted spectra for a 60 keV commanded threshold for each of the three models. Measured spectrum in 1^{st} calibration run is also shown for comparison, with χ^2_{Red} statistic values for goodness of fit displayed in the legend.

data. Figures 3.15-3.17 show the results for the 60 keV, 80 keV and 100 keV respectively.

In all three cases the Helium peak around 300-500 keV is over attenuated in the models. This indicates that either the spread in the thresholds are too high or the mean threshold value needs to be shifted down. In the double Gaussian case, the model seems to cut the leading edge too quickly as the gradient is too steep, indicating that perhaps this model could use a shift in the mean threshold value rather than a decrease in spread. In contrast, the single Gaussian and Gamma distributions show mixed attenuation of the main peak relative to the measured data.

Quantitatively, the statistic values indicate that in all three cases, the single Gaussian model best predicts the measured spectra, followed by the double Gaussian. This reflects the least scatter of posterior values in the individual fit results for the single Gaussian relative to the other models. The global model, a mean of the three fit results, is closer to the individual best fit parameter values, and so will correspondingly better predict each spectra.

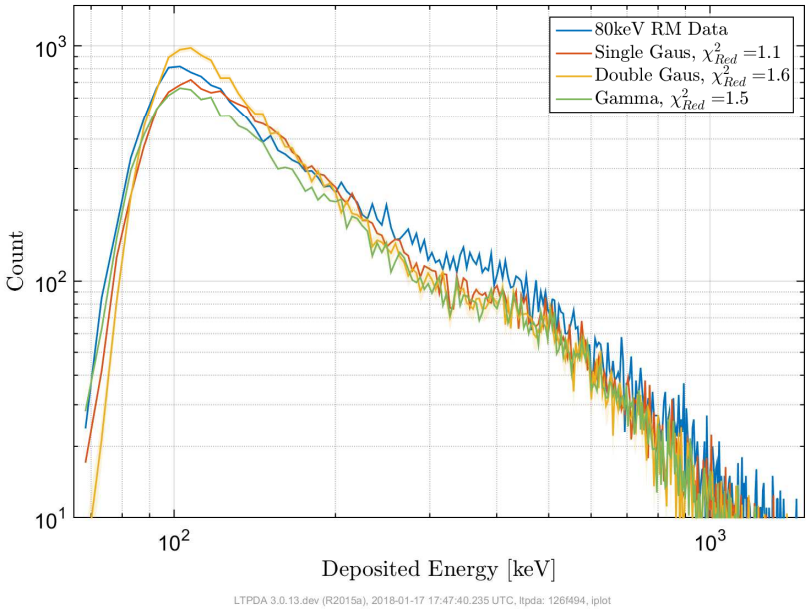

Figure 3.16: Predicted spectra for a 80 keV commanded threshold for each of the three models. Measured spectrum in 1^{st} calibration run is also shown for comparison, with χ^2_{Red} statistic values for goodness of fit displayed in the legend.

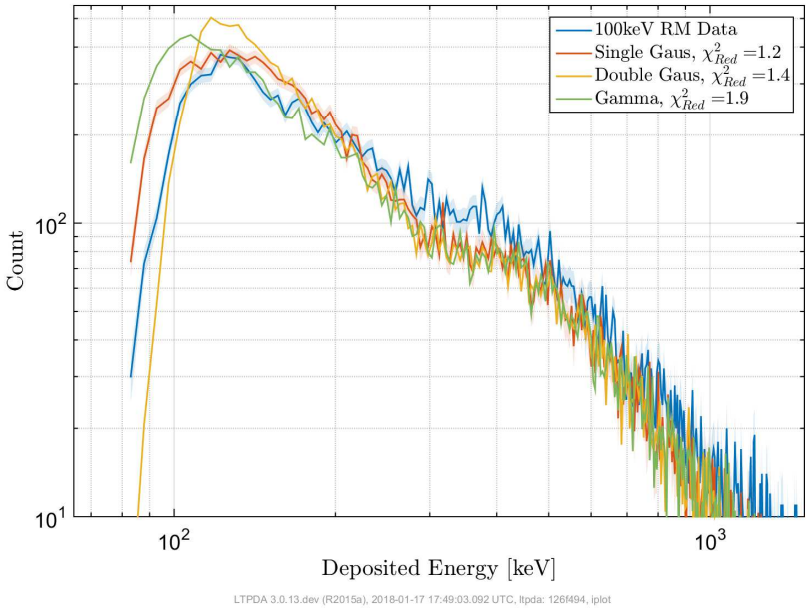

Figure 3.17: Predicted spectra for a 100 keV commanded threshold for each of the three models. Measured spectrum in 1^{st} calibration run is also shown for comparison, with χ^2_{Red} statistic values for goodness of fit displayed in the legend.

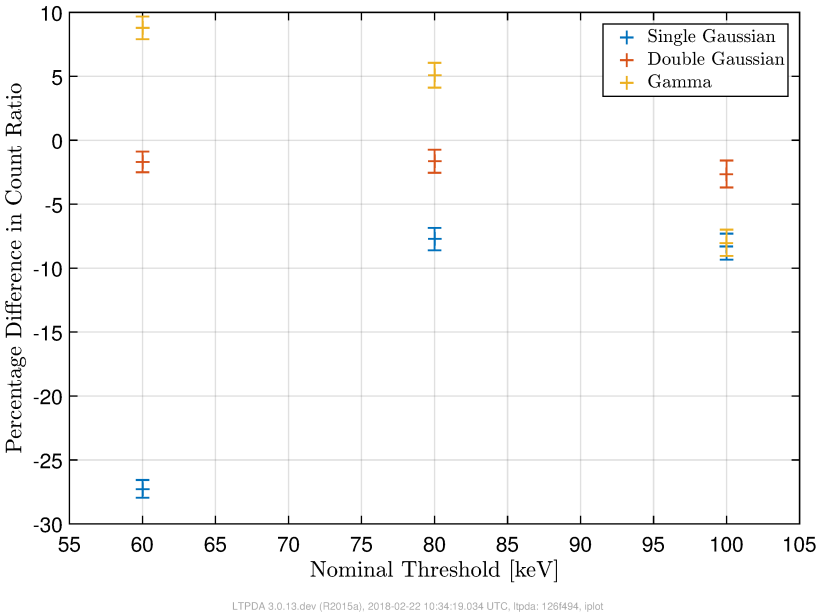

Figure 3.18: Percentage difference in singles to coincident count ratios for each of the data sets from the first calibration run used in the fits. Note that the single Gaussian and Gamma points for the 100 keV case overlay almost exactly. The singles counts do not include noise modeling, which makes the predicted singles count much less than the measured count. This exclusion is expected to make more of a difference for lower thresholds than higher ones, and for the singles than the coincident count where two noise hits must simultaneously be accepted rather than just one.

3.3.5 Singles to Coincident Ratios

One cross check for the models is the singles to coincident count ratio for the whole spectrum. It is important here to only consider counts above 60 keV in the coincident spectrum as the simulation does not take into account the noise peak, where noise-noise hits occur.

Taking the percentage difference between the measured and simulated ratio, where a negative number indicates the simulation under predicted the ratio, it is possible to compare the results for each model in the first calibration run. These numbers are shown in Figure 3.18.

Note that the singles counts were not fully simulated as noise hits become much more important in the singles than in the coincident spectra. This is because in the coincident spectra two noise hits must almost simultaneously exceed the threshold applied on each diode, which is much less probable than a single hit exceeding the threshold in the singles counts. Hence the predicted ratio is expected to be smaller than measured as the singles are missing more hits than the

coincident hits.

The double Gaussian model best predicts the three count ratios, falling marginally under the measured ratio in all three cases. The single Gaussian predicts the ratio increasingly well for increasing nominal thresholds, whereas the Gamma distributed threshold begins over predicting the ratio and ends under predicting it.

Although the stability of the double Gaussian predictions is desirable, it should be noted that as the nominal threshold increases, it is expected that the prediction moves closer to the measured value. This is because the probability for a random noise fluctuation above the threshold decreases as the threshold increases. Thus the number of measured singles not taken into account decreases as the nominal threshold increases, and the predicted ratio approaches the measured value. This makes the single Gaussian also a good fit in this cross check, and emphasizes that so far it is the best model of the three as the behaviour of the count ratios matches the predicted behaviour based on known limitations of the model.

3.4 Fitting the Second Calibration Run Spectra

A second set of calibration data was run in April 2017 to further test the models. In this run, the threshold was again fixed for a day at a time at increasing nominal energies. The commanded thresholds were 20 keV, 40 keV, 80 keV, 100 keV, 120 keV before two days were used to test individual thresholds by setting the thresholds to 60-100 keV and 100-60 keV for the front-back diode respectively. One day of 60 keV data was taken either side of the calibration run too, giving a total of nine days of data, all shown in Figure 3.19.

Note that the 20 keV data are much less than the 40 keV data in main peak height, comparing to Figure 3.5 where the 20 keV and 40 keV data were identical in the main peak. This was found to be due to saturation of the counters. The singles counts time series also exhibited this effect. In the time for the spectrum to be recorded, the number of counts accepted by the monitor amassed to more than the peak number of counts. The counter then wrapped around, starting again at zero after the maximum count was reached. For this reason, the 40 keV data

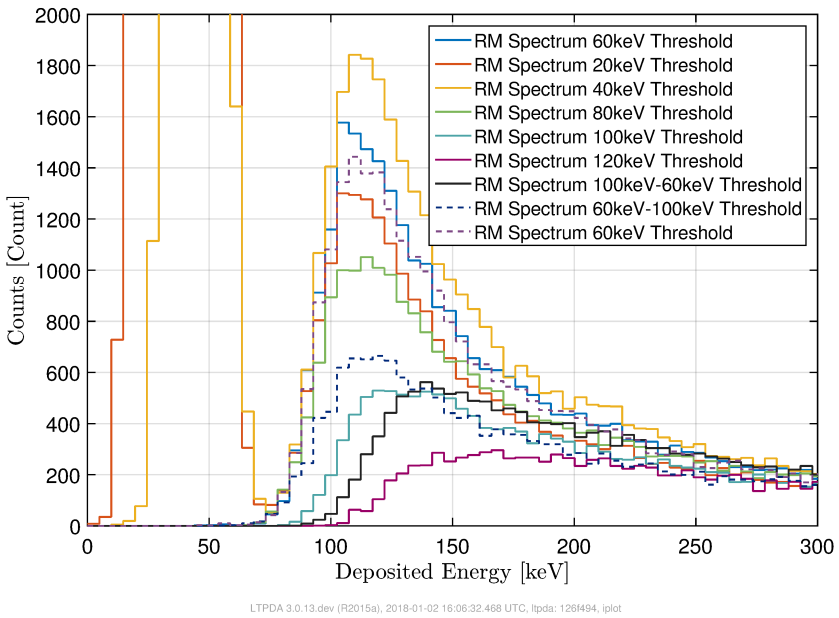

Figure 3.19: The daily histograms in the second calibration run in April 2017. Note that two of these histograms include front and back diodes set independently of one another. Also note the 60 keV data were excluded and instead one day from the nominal RM settings either side of the calibration run was included.

was used to fit for ϕ during this calibration run instead of the 20 keV data. In this case, ϕ was set to 453 MV, and the threshold again assumed to not infringe upon this fit.

The fit was repeated here for the 60 keV, 80 keV and 100 keV data so that any degradation of the model parameters could be taken into account. The inferred parameters from this fit are then used to predict the spectra of the remaining data sets to test the global model parameters' ability to reproduce data with nominal thresholds different to those of the data used in the fits.

3.4.1 Fit Results

Figures 3.20-3.22 show the fit results of the means and standard deviation uncertainties from the posterior chains. Also shown are the individual chain results from the first calibration run fits, and the global models for both sets of fits.

The single Gaussian model shows the best agreement between the first and second calibration runs. The only outlier is the 100 keV data from the second set. This pulls the global mean

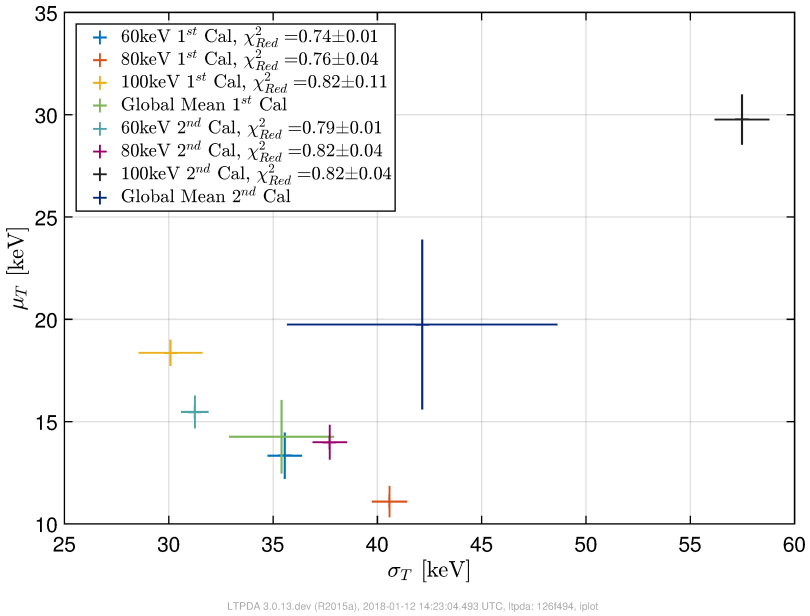

Figure 3.20: Posterior means from the first and second calibration runs fits for the single Gaussian model. Note that there is one set of data that presents some tension with the rest. This skews the global model for the second calibration run (dark blue), and lengthens its uncertainties.

for the second set towards higher values of both parameters and increases the uncertainties. However, it is still in agreement with the first global model.

The double Gaussian model presents a much greater spread in points, with the two global models only agreeing in one parameter. Note that the χ^2_{Red} statistics are around double the values for the single Gaussian model for the individual fit results. This shows that overall this model does not capture the spectra as well as the single Gaussian model.

The gamma fits also show a larger scatter than the single Gaussian model, but the global models both agree with each other in both parameters. The statistics cover a range of values, some as low as those seen in the single Gaussian case. Note that in this model, only the 100 keV cases are in agreement with each other.

Figures 3.23-3.25 show the spectra for each of the three data sets using the global parameter values deduced from the second round of fits. Also shown are the measured data and the χ^2_{Red} values.

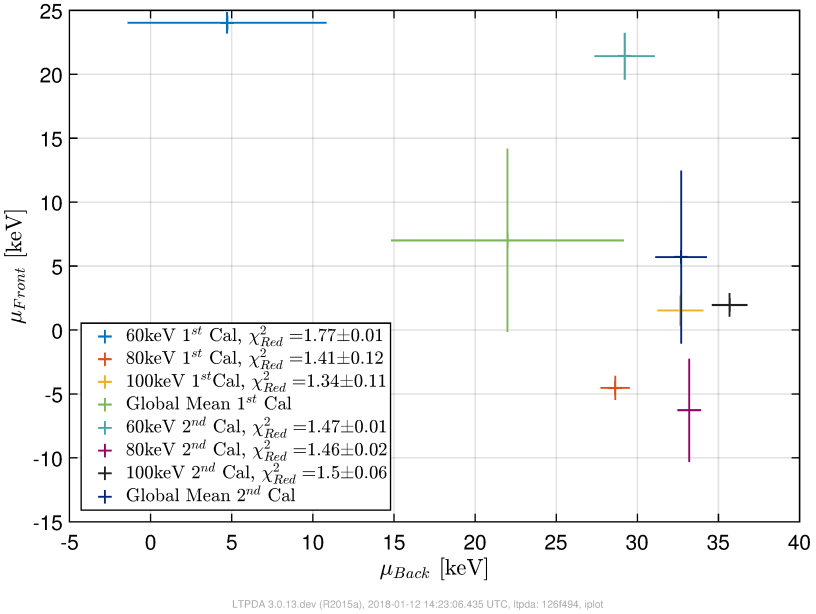

Figure 3.21: The means and 1σ uncertainties for the first and second calibration runs for the double Gaussian model. Note the large spread in the front diode offset but a tighter agreement with the back diode offset, excluding the 60 keV fit result for the first calibration run.

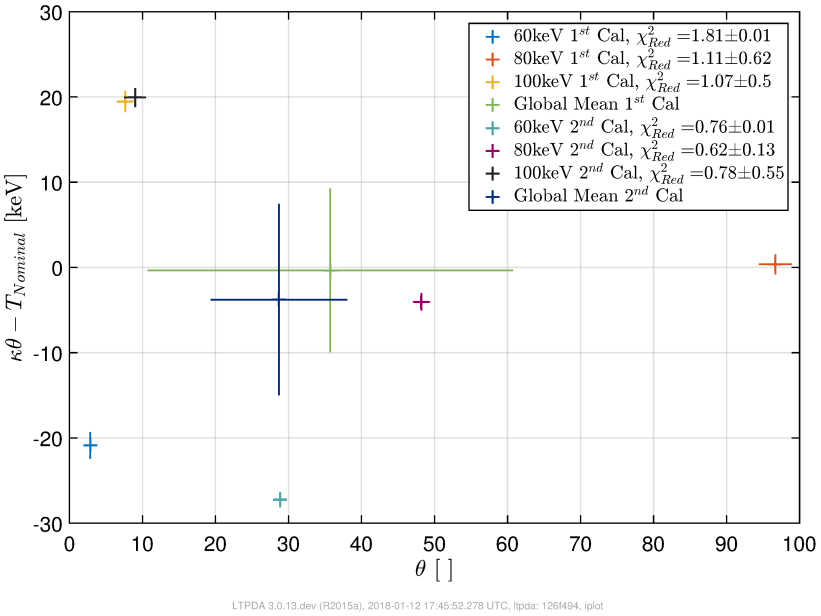

Figure 3.22: Posterior means and 1σ uncertainties for the Gamma distribution model. The individual results for each commanded threshold show some tension with one another, but the global models are in agreement. Their error bars, however, are large due to the spread in the individual results.

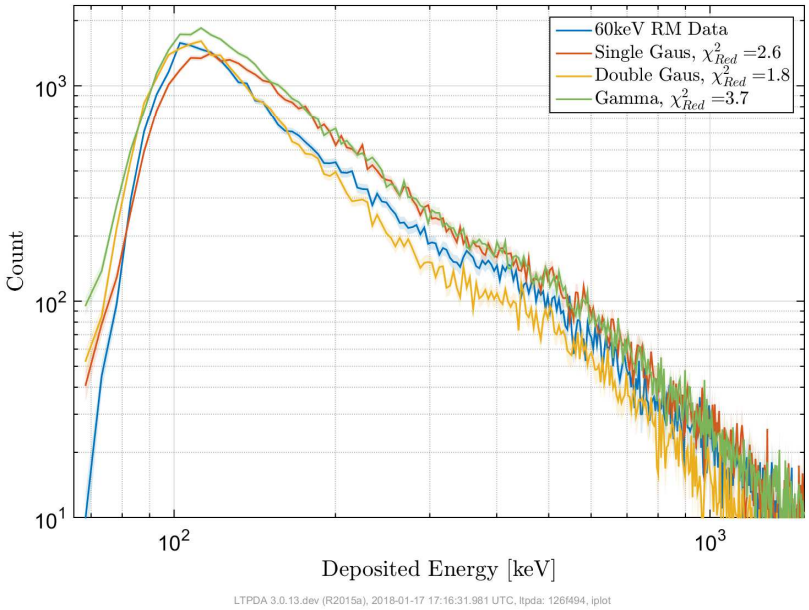

Figure 3.23: Predicted spectra for a 60 keV commanded threshold for each of the three models. Measured spectrum in 2^{nd} calibration run is also shown for comparison, with χ^2_{Red} statistic values for goodness of fit displayed in the legend.

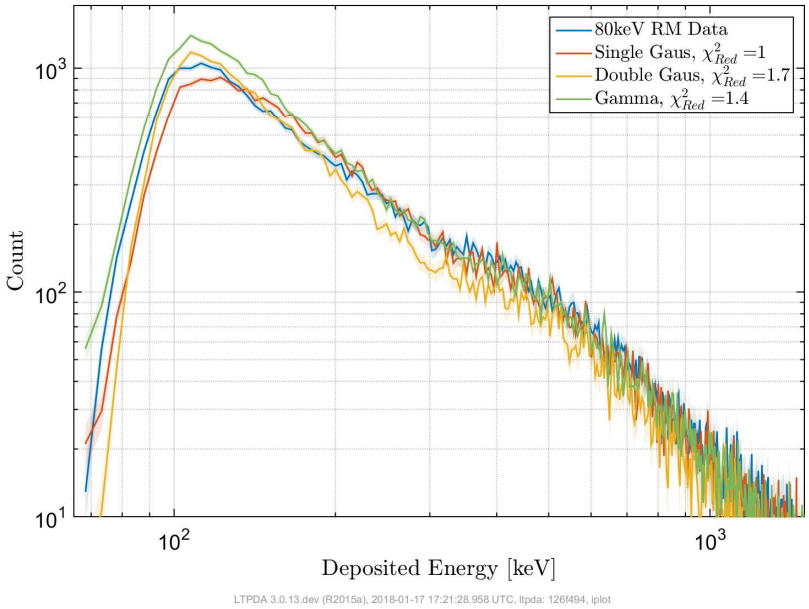

Figure 3.24: Predicted spectra for a 80 keV commanded threshold for each of the three models. Measured spectrum in 2^{nd} calibration run is also shown for comparison, with χ^2_{Red} statistic values for goodness of fit displayed in the legend.

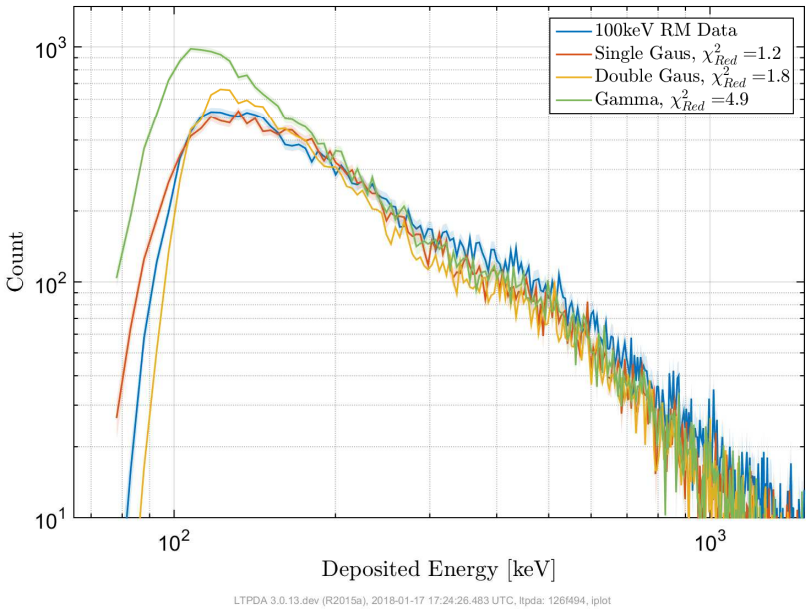

Figure 3.25: Predicted spectra for a 100 keV commanded threshold for each of the three models. Measured spectrum in 2^{nd} calibration run is also shown for comparison, with χ^2_{Red} statistic values for goodness of fit displayed in the legend.

Qualitatively all three models do reasonably well to reproduce the measured data in all three nominal threshold cases. However, the statistic values and the shape of the spectra for the Gamma distributed threshold model indicates the least-well-fitted data using the global parameters. The single Gaussian and double Gaussian then seem to both do as well as each other when looking at the shape of the spectra. Although the statistic values seem to indicate that on average the single Gaussian does slightly better.

The global models were also used to predict the shape of the 120 keV commanded threshold data for each model. The spectra are all shown with the measured data in Figure 3.26, where the best estimate of the data is by the single Gaussian model, whose reduced χ^2 is less than half the next lowest value. The double Gaussian and Gamma models did increasingly worse to reproduce the data. The double Gaussian seems to be too limited in spread while the Gamma model seems to be too liberal in spread.

The data suggests that the spread on the threshold needs to be constrained more than implied by the previous fits. In terms of the single Gaussian model, perhaps if the second calibration run's 100 keV data had been omitted, and the global parameters been more like the first

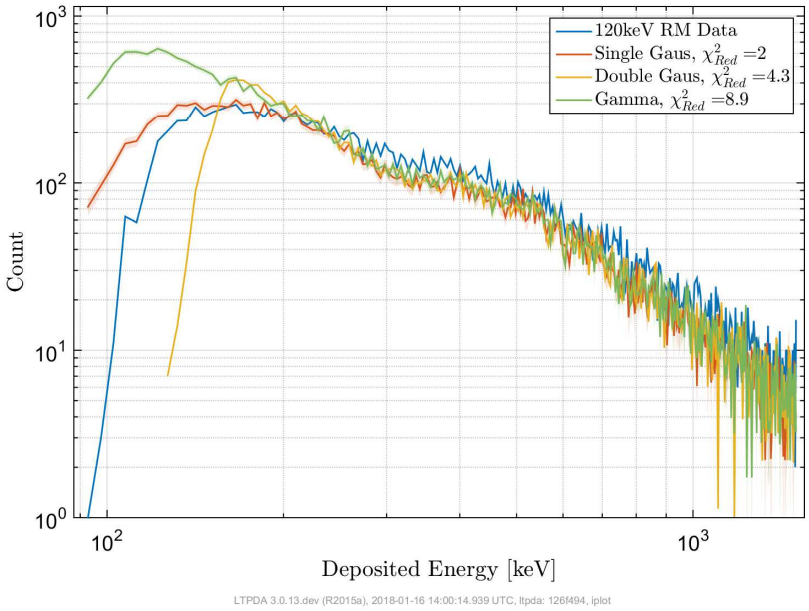

Figure 3.26: Predicted 120 keV commanded threshold data using the second calibration run global parameters. The RM measured data (blue) is plotted with the single Gaussian model (red), the double Gaussian model (yellow) and the Gamma distributed threshold (green).

calibration run's, then the resulting predicted spectrum would agree more with the data.

3.4.2 Testing Individual Diode Thresholds

The remaining two days of data from the second calibration run were used to test the models applied to each diode independently. Here the thresholds are set to 60-100 keV and 100-60 keV for the Front-Back diodes respectively.

Figure 3.27 shows the predicted spectra from each model with the measured data for the 60-100 keV thresholds. The best fit spectrum to the data is from the double Gaussian model, although the single Gaussian and Gamma models approach the correct high energy limit.

The majority of the disagreement is in the main peak for all three models. As with the 120 keV predictions, these results suggest that the single Gaussian and Gamma distributions are too broad, while the double Gaussian threshold is not broad enough. In the case of the single Gaussian, this again suggests that the 100 keV data could perhaps be an outlier in the full set of fits.

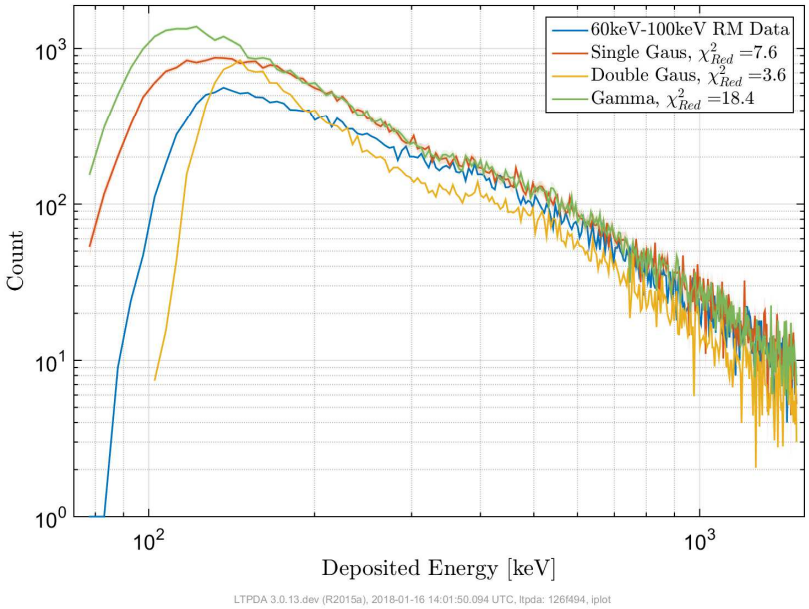

Figure 3.27: Predicted spectra by each model for the independent diode thresholds set at 60-100 keV for the front-back diode respectively. Not the statistic for the double Gaussian is the lowest, and the Gamma the highest.

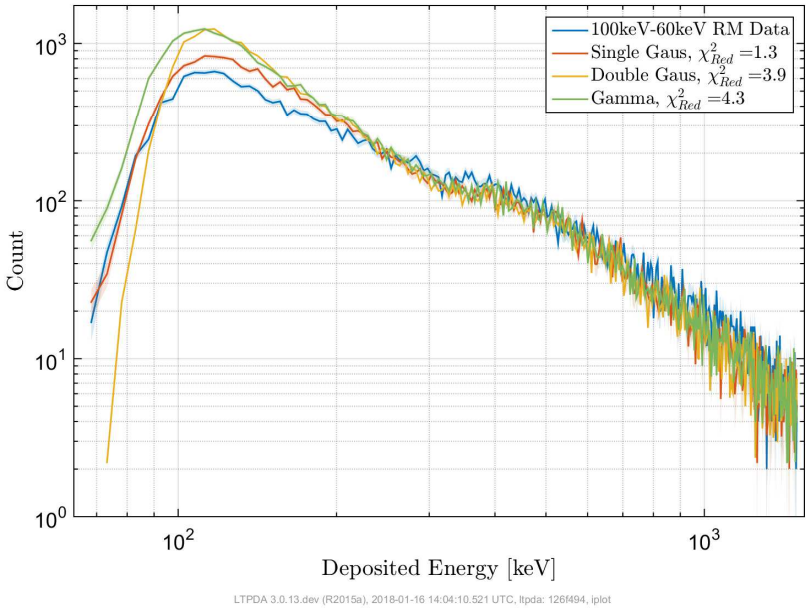

Figure 3.28: The same as Figure 3.27, only with 100-60 keV commanded thresholds for the front-back diode respectively. Note the difference in order of statistics. The single Gaussian matched the measured spectrum closer than the other models, while the Gamma model matched the farthest.

Figure 3.27 shows the predicted spectra for the 100-60 keV data. In general the global parameter values reproduced the data much better than in the 60-100 keV case. All models gave a closer approach for the high energy limit, with the tensions between simulations and RM data focused in the main peak. In this case, however, the single Gaussian model was much closer to the measured data than the other models. There is still a slight over prediction in the main peak, but the leading edge matches with that of the data better.

These plots demonstrate that there is clearly more complex behaviour in the data that is not fully captured by the models derived. Given that most of the tension is in the main peak, and that the high energy limit is a small fraction of the total hits in the spectrum, it could be inferred that better resolution is needed in the main peak portion of the spectrum. Furthermore, the LISA RMs, should they follow a similar design to the Pathfinder RM, should test the individual diode thresholds individually and in more depth to try and capture some of the complexities not fully grasped in these calibration runs.

3.4.3 Count Ratios

A further test of the models is the count ratios. As with the first calibration run data, the singles count that arise purely from noise are not simulated, and so the count ratios are expected to be lower those measured. Furthermore, as the nominal threshold rises, the gap between the measured and predicted ratios is expected to decrease as the number of noise hits that are unaccounted for decreases.

Figure 3.29 shows the percentage difference between the measured and predicted ratios for each data set, using the global models from the second calibration run. The double Gaussian model is in best agreement with the measured ratios, with some over predicting and some under predicting. The Gamma model is the farthest from measurement, although it does reproduce the expected trend in under prediction. Similarly, the single Gaussian model reproduces the expected trend, but is in better agreement on average with the measured values.

Both the Gamma and single Gaussian models suggest that the individually set nominal thresh-

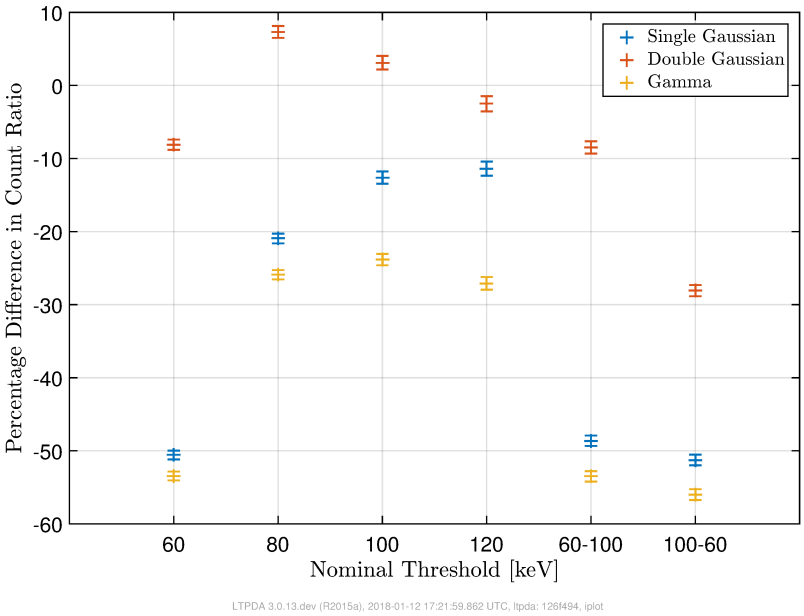

Figure 3.29: Percentage difference in the predicted and measured singles to coincident count ratios. Note again that the predicted singles count is lower than the measured due to no purely noise hits included int he simulations. This affects the singles more than the coincident counts, meaning that the predicted ratios are expected to be lower than the measured ratios. Furthermore, this effect will diminish as the commanded threshold is increased, meaning that as the commanded threshold increases, the percentage difference in predicted and measured ratios should decrease.

old values have count ratios that are governed mostly by the lower of the two thresholds set as their deviations from the true values are the same as the 60 keV case. Overall, the count ratios imply that there are approximately half as many noise counts as counts already accounted for missing in the simulation. In future developments of the model, these results could be used to infer the time dependence of the noise hits, which is required to fully simulate these hits. Furthermore, comparison of the over/under prediction of the simulation in the two calibration runs can give an estimate of how the time dependence changes with mission time. This could be useful for LISA, where the mission time is several times as long as Pathfinder's.

3.4.4 Convergence Tests

Two forms of convergence tests for MCMC simulations are now employed to test the convergence of the fits. One tests the stability of a single chain using a z-score [59], while another,

the Gelman-Ruben statistic, tests the end solution by comparing multiple chains initiated at different regions in parameter space [58]. The former takes short intervals of the posterior chain and compares the inferred means and uncertainties at different times. If they are in agreement with each other to within a variable margin, then the chain has converged to a stable solution. The latter uses the inferred posterior values and uncertainties in two or more chains to compare independent solutions of the same fit. If all the posterior values are in agreement to within the combined uncertainties, then the solution is globally acceptable.

These tests are aimed to capture any variation in the optimal model for the data due to initialization of a chain. Sometimes, particularly in many variable parameter spaces, some combination of parameters can act in similar ways to other parameters, hence leading to multiple stable points in parameter space. In this situation, because each model purposefully used a two dimensional space to reduce computational costs, the chains were run twice to perform these tests.

Figure 3.30 shows the z-scores for each of the primary chains. These scores show that all of the individual chains have converged as the posterior mean for each segment is no more than one standard deviation away from the whole chain's mean, implying a stability in the values reached.

Figure 3.31 shows the Gelman-Ruben statistic for each of the parameters fitted in the first and second calibration run. These compare the primary posterior chain with a secondary chain initialized in a far region of parameter space from the initialization point of the primary chains.

These results show that with the exception of the Gamma distribution, all of the chains and posteriors were stable to within one standard deviation, and that the posterior values reached for each model were global solutions for the fits.

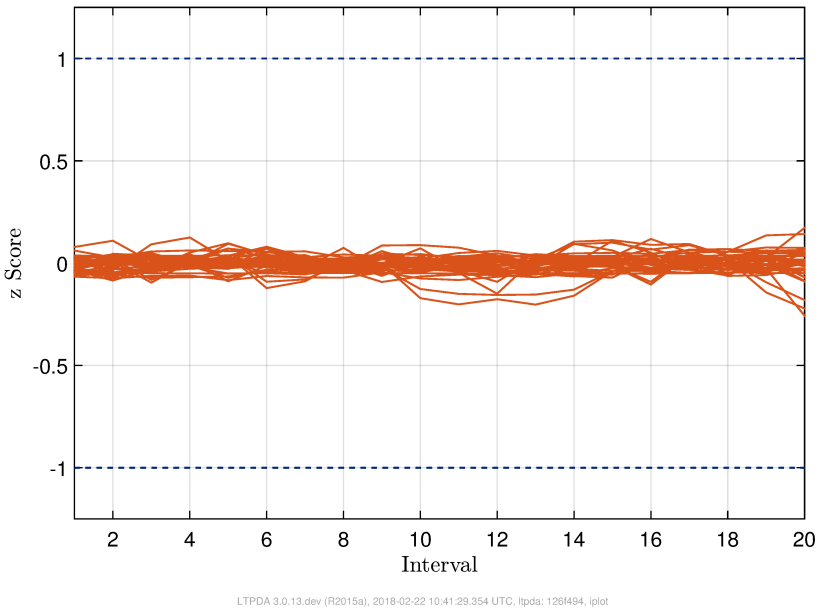

Figure 3.30: z-scores for each posterior chain obtained in the fits. There are 36 in total (all red): 2 parameters for for each of 3 models fitted using 2 calibration runs with 3 data sets each. The z-score is defined as the deviation of a local mean value (given by interval number) divided by the standard deviation of the whole posterior chain. Therefore intervals exceeding 1 (dashed blue lines) suggest that the mean value for that subsection of data exceeds the whole posterior mean by 1σ. In this case, none of the intervals for any of the chains exceed this limit, indicating a good stability in the chains and the true minimum in the model has been reached.

3.5 Quantifying Daily Changes in ϕ

Some of the variation in the fit results could be due to a change in the solar attenuation parameter from day to day. Through both sets of calibration data, ϕ was assumed constant through the two weeks. However it was already demonstrated that there is a roughly week long cycle in solar activity that is causing a similarly cyclic variation in ϕ.

Here an attempt is made to quantify some of this variation in model parameter best fit values by looking at the TC2 channel from Integral's SREM data [67]. Figure 3.32 shows these data through the time of the first calibration run. The data have been averaged to hourly counts, and the percentage change from the initial value taken. There is a small, gradual dip in the counts through the week, which is directly correlated with changes in ϕ. The data used in the fits correspond to just before half way through this stretch of data to the end.

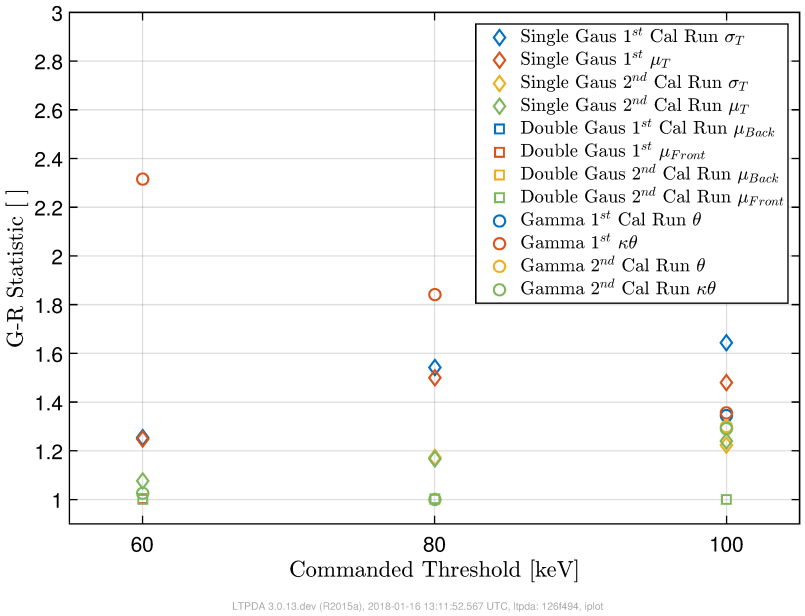

Figure 3.31: Gelman-Ruben statistics for each of the 36 posterior chains plotted as a function of the commanded threshold for clarity. The single Gaussian (diamonds) and double Gaussian (squares) showed a good agreement between the primary and secondary chains. However, the Gamma distribution presented some trouble, especially in the 60 keV data. Not shown is a point at (60,9.4) corresponding to the θ posterior from the first calibration run's 60 keV data, indicating that the posterior solution is not singular as the two chains did not agree on posterior values.

This shows that there is a total possible change of around 3-4% through a week long calibration run, implying a change in ϕ of around 20-25 MV. In order to take these variations into account in the fits, the single Gaussian model was re-run for $\phi = 580$ MV and $\phi = 630$ MV, corresponding to the original value of 605 ± 25 MV for an upper limit of the effects of this assumption on the results.

Figure 3.33 shows the resulting fits for the two new values of ϕ, along with the original fit results. Although the points agree with each other in the σ_T axis, there is a deviation in the lower estimate of ϕ of almost a bin width. The change in point position highlights that only some of the change in μ_T posterior values in the three data sets can be explained by variation in the solar attenuation parameter.

Further doubt can be cast on the model as the global parameters derived suggest a large standard deviation that would place a significant portion, around 30%, of the randomly drawn

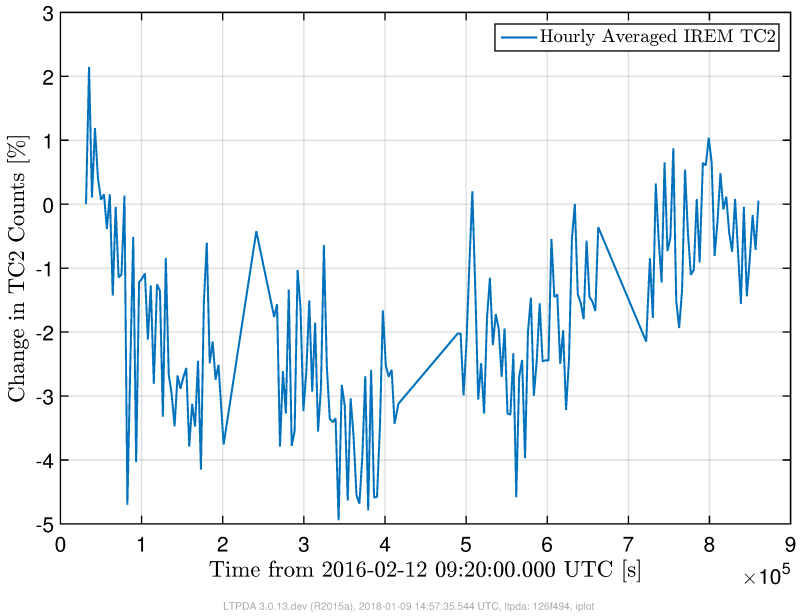

Figure 3.32: Hourly averaged TC2 data over the time of the first calibration run, from Integral data online. This channel is equivalent to the singles channel in the Pathfinder RM, and correlates with the change in solar attenuation parameter ϕ, indicating that there is some change in this parameter through the calibration run that is not accounted for in the fits.

thresholds in the range of data used for the initial fit for ϕ. Since the threshold was assumed to be absconded below the cut at 60 keV when fitting for ϕ, the fit results cannot be totally trusted. In addition, the blind tests of individually set thresholds and 120 keV data were not well reproduced by any one of the models' global parameters. What has been learned, however, is that a simple, single Gaussian distribution is the best choice in distribution for the thresholds.

3.6 Coincident Count Spectra for Second Estimate of ϕ

In this section, the output from GEANT4 is processed to form a predicted coincident count spectrum, which is then used to give a more accurate estimate for ϕ through the Pathfinder mission compared to the first estimate in section 3.2. Since the single Gaussian threshold model performed the best in the fits but significant doubt was shed on the fit results, this model was adopted for the thresholds, but the mean and standard deviations were set to the electronic noise values to reflect that they may have some common origins in the spacecraft.

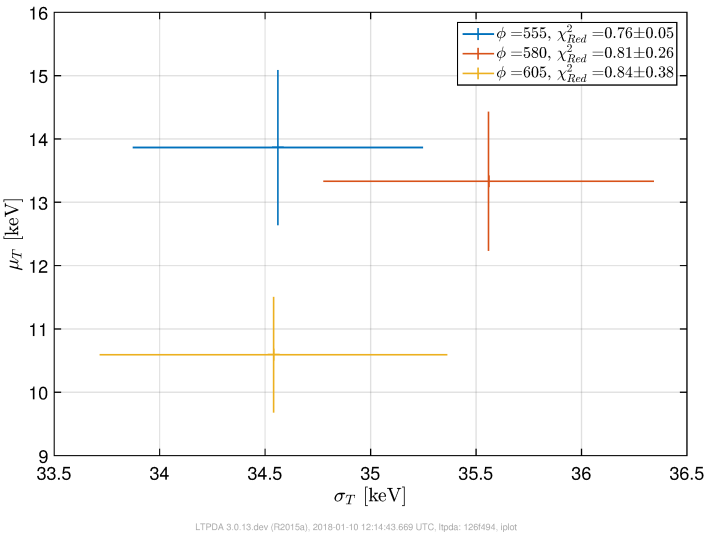

Figure 3.33: A test of the dependence of the fit results on an expected change in solar attenuation parameter through the calibration run. The maximal change in ϕ is estimated using the TC2 data to be around 20-25 MV over two or three days. The blue and yellow crosses indicate the fit results for ϕ-$\delta\phi$ and ϕ+$\delta\phi$ respectively.

The hits from GEANT4 have electronic noise added to them, and then both diode energies are compared with the Gaussian distributed threshold. The entries that survive the comparison in both diodes are then recorded as a coincident hit. The back diode deposited energy is then binned into a histogram ranging from 0 keV to 5000 keV with 1024 bins, constituting the predicted coincident spectrum.

Summing the ten minute measured spectra through each day gives the daily coincident spectra. These have better bin statistics than the ten minute spectra as the total coincident count is larger. This is better for the fitting process that assumes a root-N error on the individual bins, an assumption that works better for larger counts.

Using a Monte Carlo method to sample a ϕ value, the primary spectrum for protons and helium nuclei are re-scaled, and the resulting coincident spectrum calculated. A posterior distribution for the daily ϕ can be produced as the procedure finds the optimal ϕ that best fits the measured coincident spectrum. Then a mean and 1σ uncertainty are estimated by fitting a Gaussian to the posterior. Figure 3.34 shows the predicted daily parameter (blue) compared to the results using the singles count (red).

Figure 3.35 shows an example coincident spectrum predicted by the single Gaussian model for the RM for January 13^{th} 2016. Red data shows the measured spectrum for comparison, and the reduced χ^2 is included in the legend. Although the fit was not ideal, it illustrates

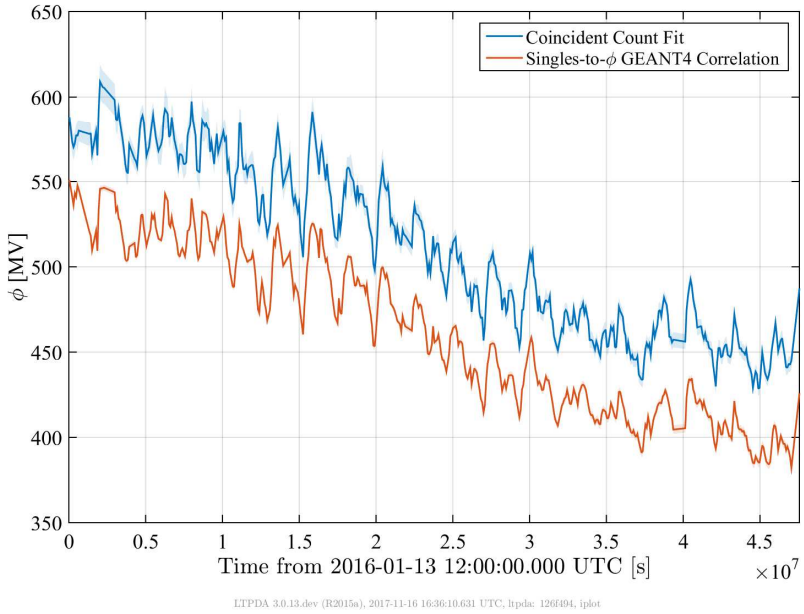

Figure 3.34: Resulting solar attenuation parameter predicted by fitting the GEANT4 data to the daily measured coincident spectra through the mission (blue). For comparison, the results from the correlation of the singles count with various values of ϕ using just GEANT4 data and a hard threshold (red).

that the simulation is a good approximation to first order. There is a discrepancy both in the leading edge of the main peak and in the smaller Helium peak around 400 keV. The main peak is affected by both the shape of the threshold and the solar attenuation parameter, but the Helium peak is less affected by the threshold given it is higher in mean deposited energy. This suggests that there is perhaps a problem in the GEANT4 model for the interactions between Helium nuclei and the detector, or the threshold is not wide enough as the position of the Helium peak has not quite lined up with the measured data.

As was expected, the singles count estimate was systematically lower than the coincident count estimate by about 8%. This reflects that the model did not include the noise hits in the singles count case, which did not affect the coincident count fit as it was possible to cut them from the fits. The fit to the singles counts predicted a lower ϕ so that the singles rate was increased to meet the measured rates and account for the missing noise hits.

In both time series produced the 9-13 day oscillation is observed, corresponding to heliospheric current sheet crossings at harmonics of the Sun's 27 day rotation period. The general trend to

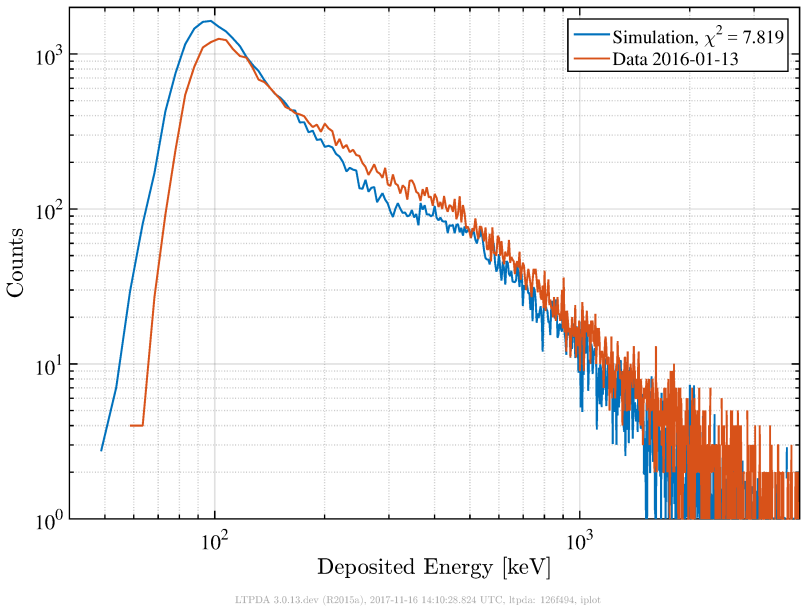

Figure 3.35: Example spectrum from the coincident count fit (blue). The measured spectrum for the example day is shown (red). Note the discrepancy in the position of the helium peak around 400 keV. The leading edge of the main peak also presents some tension, but the shape is determined by a number of parameters whose exact values is not always straightforward to extract.

lower values of attenuation corresponds to the time in the solar cycle epoch when operations took place: the solar minimum occurring around a year after the end of operations giving the minimum ϕ, and a decreasing value in time through operations.

3.7 Comparing Results with INTEGRAL-PAMELA Correlation

In order to test the validity of the results, it is possible to compare the GCR fluxes with predictions from other experiments. The comparison made here uses a combination of two experiments: IREM on INTEGRAL and PAMELA. IREM uses a slightly more sophisticated monitor comprising several layers of sensitive detection materials. PAMELA, currently no longer operational, used a similar monitor to INTEGRAL to predict the solar attenuation parameter through the majority of the previous solar cycle.

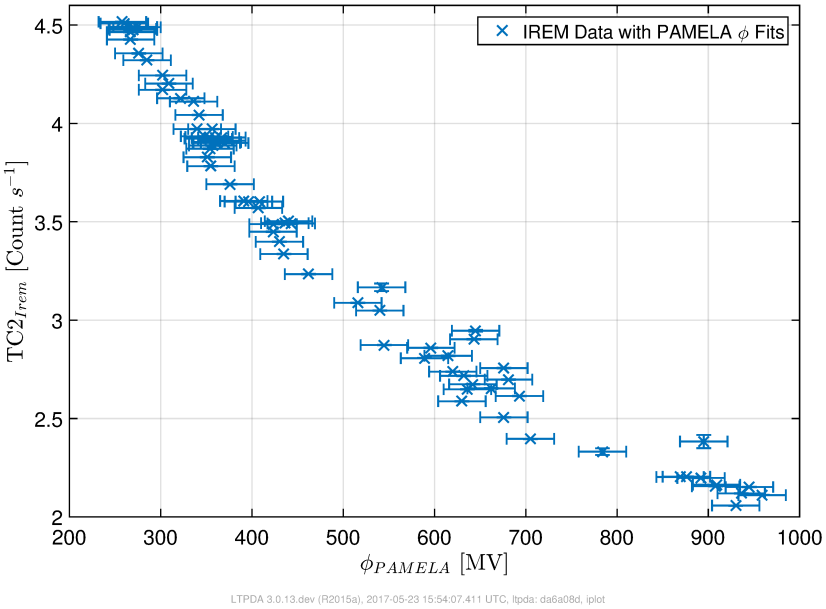

Figure 3.36: Correlation between the TC2 channel in INTEGRAL and PAMELA predictions for the solar attenuation parameter ϕ between January 2003 and January 2009.

Correlating IREM's TC2 channel, which closely resembles the Pathfinder singles channel, with PAMELA estimates for ϕ from 2003 to 2009 in monthly averages, then evaluating using the TC2 measured counts through the Pathfinder mission reveals another estimate for ϕ. Figure 3.36 shows the correlation between the two data sets, while Figure 3.37 shows the monthly TC2 counts during the Pathfinder mission. Figure 3.38 shows the resulting ϕ estimate from this correlation.

It should be noted that the PAMELA estimates use an older model for the LIS, which is outlined in Usoskin *et al.* [123] where the PAMELA estimates were taken from. This means that the absolute values of the attenuation parameter from the Pathfinder RM data fits cannot be directly compared with those obtained from this correlation. Instead the structure of the flux variations must be compared graphically.

Figure 3.39 shows the fluxes predicted by the coincident count fits and the IREM-PAMELA correlation for September 1^{st}, 2016. Note the difference in ϕ for the two methods, where different LIS models were used, highlighting the need for a qualitative comparison instead of direct comparison between the phi values from each fit. There are small differences between

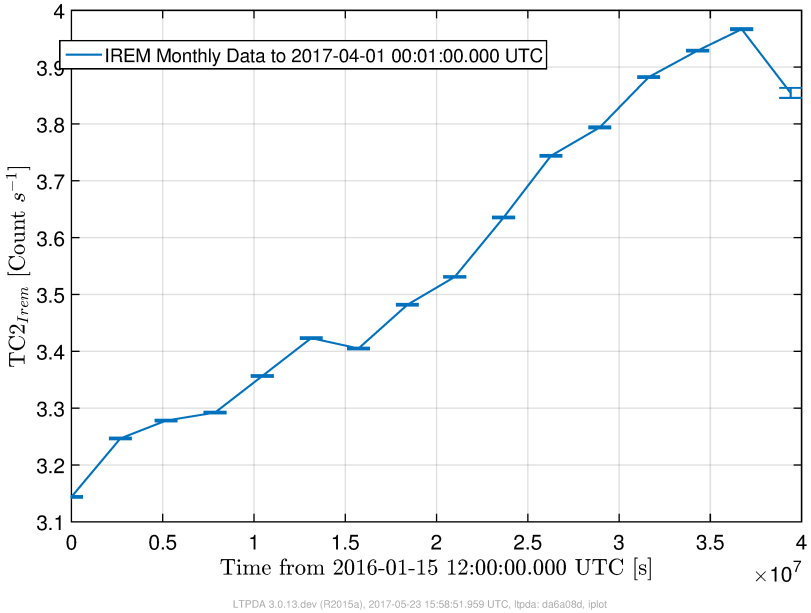

Figure 3.37: Monthly average counts for the TC2 channel in INTEGRAL during the LISA Pathfinder mission. This will be used to evaluate the function fit to the INTEGRAL-PAMELA correlation for the time 2003 to 2009 to give an estimate of the solar attenuation parameter ϕ in this time.

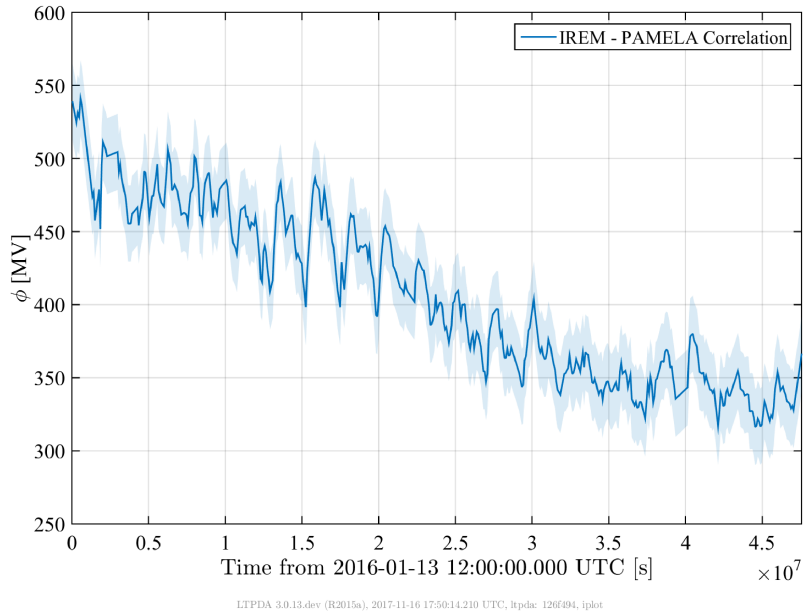

Figure 3.38: Solar attenuation parameter ϕ as a function of time through the LISA Pathfinder mission as predicted by a correlation between INTEGRAL and PAMELA data from the preceding solar cycle. Shaded region shows the associated error with the fit result.

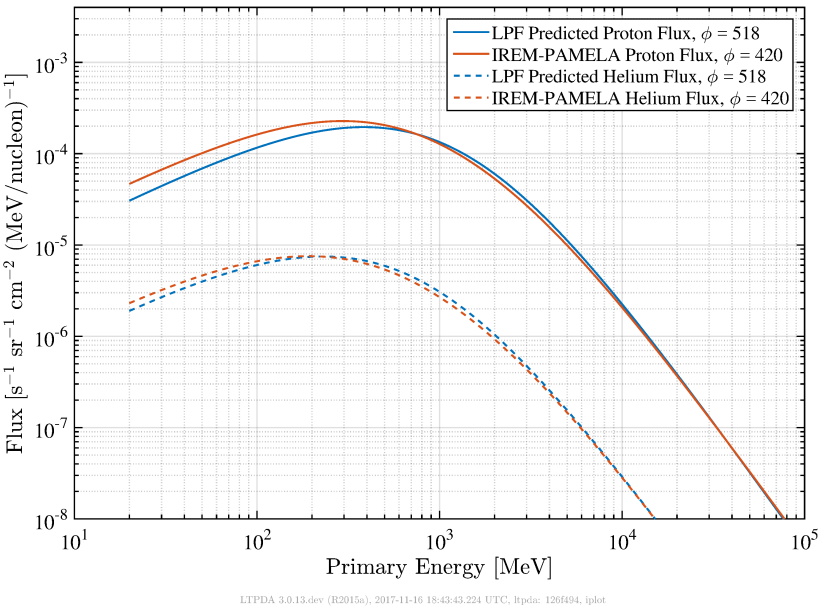

Figure 3.39: Example spectra predicted by the coincident count fits (blue) and the IREM-PAMELA correlations (red) using data from the previous solar cycle. The discrepancy in the lower energy limit is included for effect. In reality, the spacecraft will shield up to around 100 MeV. There is a slight difference in the higher energy limit that accounts for the older LIS model used for the PAMELA estimates. The integrated fluxes are in agreement to within 10%.

the two models, including a slight change in the high energy. This emphasizes the difference in LIS as the high energy limit of the ϕ model tends to the LIS. The shape changes are also visible in the turning points. The low energy limit is extended further for emphasis when in reality the spacecraft will shield up to around 100 MeV. The low energy limit is determined by a combination of the attenuation parameter and the LIS model used, which explains the larger difference in results at lower energies. Note that the difference is more pronounced in the Proton spectrum than in the Helium. Overall, the integrated flux (Protons plus Helium) is in agreement within about 10%.

3.8 Outlook for LISA

The purpose of this work was to test existing models for the radiation environment, and the understanding of the underlying physics behind these models. Then, these models can be used to provide *in situ* measurements of the radiation environment so that the charging rates, and

therefore the charge induced acceleration noise, can be projected to times in the solar cycle that LISA may fly in. In this section, the results of the analysis are briefly put into context for the LISA mission. It will be demonstrated that although the final projection cannot yet be made, this analysis provides a stepping stone for the estimation.

3.8.1 Correlating ϕ with measured test mass charging rates

In order to project charge induced noise and charging rates to LISA, it is necessary to correlate variations in GCR flux with test mass charging rates. Using the radiation monitor, which includes a similar amount of shielding relative to the test masses, *in situ* measurements of ϕ can be correlated with the charge rate measurements.

However, several charge management and measurement experiments have shown that there is more to charging rates that just the GCR flux. The TM potential and force authorities (configurations) can change the charging rates, even in extreme cases reversing the current. For this reason, the end correlation of space weather with charging rates cannot be presented here as it requires further analysis to assess the dependence on these parameters. Instead, a brief, qualitative description is given of the importance of these measurements while highlighting the complexity of the final goal.

Nearly three hundred charge measurements were made through the mission. Of these, only around fifty last longer than an hour and provide a continuous charge rate as a function of time. An example of this is shown in Figure 3.40 with the singles count rate from the radiation monitor. The correlation is clearly visible while the configuration of the spacecraft (in this case nominal) and the test mass potential varies slowly as the charge accumulates.

In total, only a handful of longer measurements at a time were in the same configuration. Shorter measurements can be used to measure charging rate if a linear extrapolation is used between subsequent measurements. However this can only be done if the interim experiments do not change the test mass potential, force authority or do not trigger a safe mode re-grab. Unfortunately as these measurements were often performed once a week during station keeping,

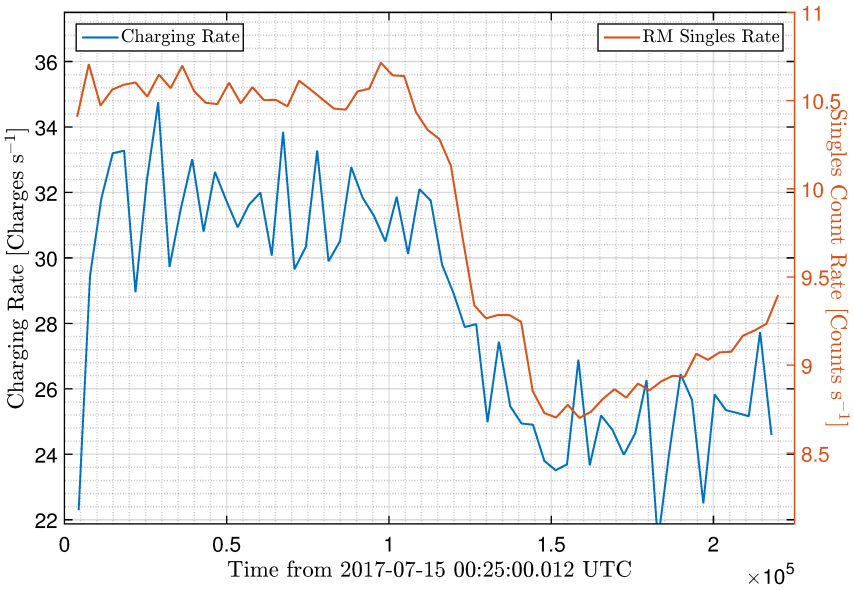

Figure 3.40: Example of a long charge rate plotted with the RM singles count rate. There is a clear correlation between the two. However, test mass potential and force authority change the correlation properties.

these vetos often applied.

Grouping the longer charge runs by translational and rotational charge measurement modes (injections in x and ϕ TM axes respectively), some qualitative aspects can be detailed. Figure 3.41 shows the remaining nominal measurements of charge using translational and rotational injection modes, and the ultra ridiculously low authority (URLA*) with rotational modes only. Of the fifty-odd measurements, never more than five or six were in the same configuration as there were several configurations available from 'big', to 'nominal', to 'low' etc. which diluted the number of similar measurements.

The scatter within each configuration (colour coded) is due to test mass potential, which was not labelled at each point. Notice that the trend seems to suggest a positive correlation in URLA* and negative trends in the nominal cases, suggesting the authority severely effects the results. It also implies that there is a significant population of secondary charges with energies of order eV's, as these would be strongly influenced by the voltages applied on the test mass that are of orders of a few volts in amplitude. Such low energy charges (likely electrons) were indeed anticipated, but not explicitly included in the GEANT4 simulation as there is a lack of

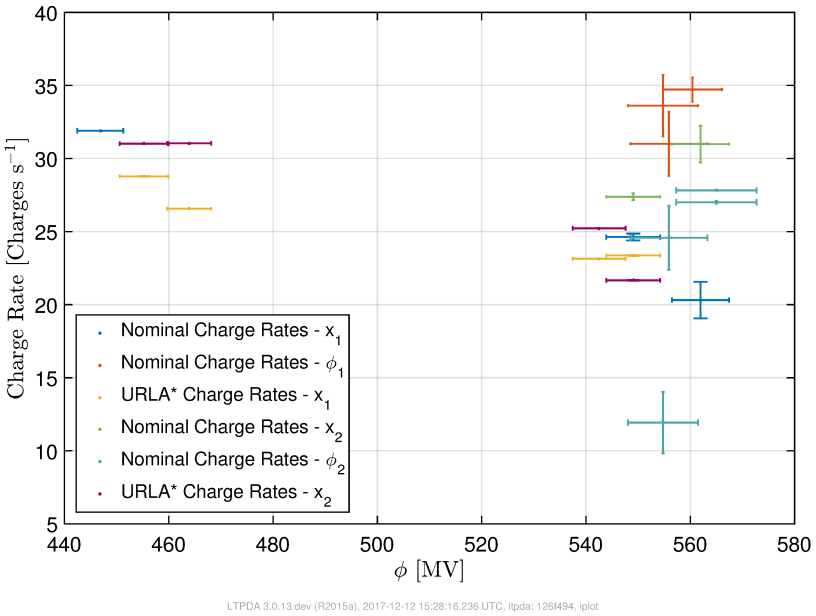

Figure 3.41: Illustration of the complexity in correlating test mass charging rates with solar attenuation parameter. The results are a strong function of test mass potential and force authority, leading to a change in slope and position of the points. Colour denotes configuration, while test mass potential is not labelled but assumed the source of scatter in each group of points.

models at such low energies.

In order to complete this analysis, shorter charge runs would need to be looked at in more detail, picking out sequential measurements where the interim experiments did not change the charging properties significantly, to increase the number of reliable charge rate measurements. A simulation that estimates charging rates from GCR fluxes exists, and will be run using the ϕ values derived in this analysis. A comparison can then be made between the measured and simulation rates, with any deviation likely a result of low energy charges.

3.8.2 Lessons Learned for LISA RMs

As the preparations for LISA begin, the lessons learned from Pathfinder are under review. As a result of the analyses presented here, several recommendations were made for the pre-flight testing of the RMs for LISA.

The most significant recommendation would be to fully characterize the threshold noise charac-

teristics on ground for the RM and accompanying electronics. This can be done using a simple oscilloscope trace and test pulses injected into the system to simulate a hit. Furthermore, electronic noise parameters should be measured directly at several points in the circuitry to account for the contribution from each component. Test pulses should be characterized and better documented pre-flight with the system response included in the testing. These changes would mean the pre-flight noise properties could be used to calibrate the instrument in-flight and more accurately account for degradation through the mission.

There should also be tests of the long term behaviour of the monitor. The flight time for LISA is longer than Pathfinder, and so it cannot be concluded here if degradation will play a significant role in the analysis of the same data in LISA. Therefore testing should be done to ensure that noise parameters for both the electronics and thresholds will not degrade beyond acceptable limits for flight.

It was also noted that because the majority of hits fall in the main peak of the spectrum, and therefore close to the nominal threshold, the binning in the RM is not optimal to reconstruct the energies of primary particles. It was recommended that a restructuring of the bins be made so that resolution around the main peak is improved at the expense of bins in the tail of the spectrum. This can be done, for example, with logarithmic binning instead of the linear spread used in the Pathfinder RM.

3.9 Discussion

Of the three models tested for the threshold shape, the single Gaussian model best reproduced the measured spectra using a global model. This model was derived using the first calibration data, and then substantiated using the second calibration data. Although it reproduced the data well, the 100 keV fit in the second calibration run did present tension in the results. The 120 keV data also showed some tension as the χ^2_{Red} statistic was higher than with the other nominal threshold spectra fits. This implies that as the threshold increases, there are complexities in the system not taken into account. This could be in any of the parameters used in the model, for

example a component in the electronics saturating as the threshold voltage increases, causing the electronic noise to step change. However, for the entire Pathfinder mission, the threshold was set to 60 keV, implying that understanding the behaviour at higher thresholds may not be necessary if only to suggest that there are other factors not accounted for in the model.

The parameters for the thresholds fit at the time of the first calibration run, around February 2016, were found to be $\mu_T = 14.3 \pm 2.5$ keV and $\sigma_T = 35.4 \pm 1.8)$ keV. These values agree with the individual fit results for this model, and with errors smaller than the bin width used to construct the spectra.

However, reasonable doubt was cast on the fit results as the parameters extracted suggest that the initial assumption that the fits for ϕ using the 20 keV and 40 keV data are independent of threshold was invalid. Furthermore, the 120 keV data and individually set thresholds data were not well reproduced, and the variation of the parameters from each fit result was not entirely explained by a variation in ϕ through each week. For these reasons, the single Gaussian, which fared best out of the three models tested, was adopted for the threshold distribution but the parameters values were equated to those found for the electronic noise. This reflected that part of the electronic noise could be similar in origin to the threshold noise if they are, for example, sourced from the same reference voltage.

As with all experiments on Pathfinder, it is important to note lessons learned so that improvements can be implemented when designing LISA. In retrospect, the threshold noise should have been measured individually on ground. Indeed, the functionality of the circuitry behind the monitor was checked pre-flight, an example check is shown in Figure 3.42, but no measurements were recorded [29].

Relating this back to Figure 2.5, the yellow curve denotes an injected pulse from B7 or B8 into the charge amplifier B1 or B2. The purple shows the the voltage of the discriminator for that diode, either B5 or B6, while the green trace shows the peak holder B11 that keeps track of the maximum voltage recorded in a given signal pulse, and the cyan vertical line denotes the voltage reference (threshold) which is stored in B9 or B10. The horizontal scale is $2\,\mu$s/pt and the vertical scale is 1 mV per minor axis tick (roughly equivalent to 100 keV).

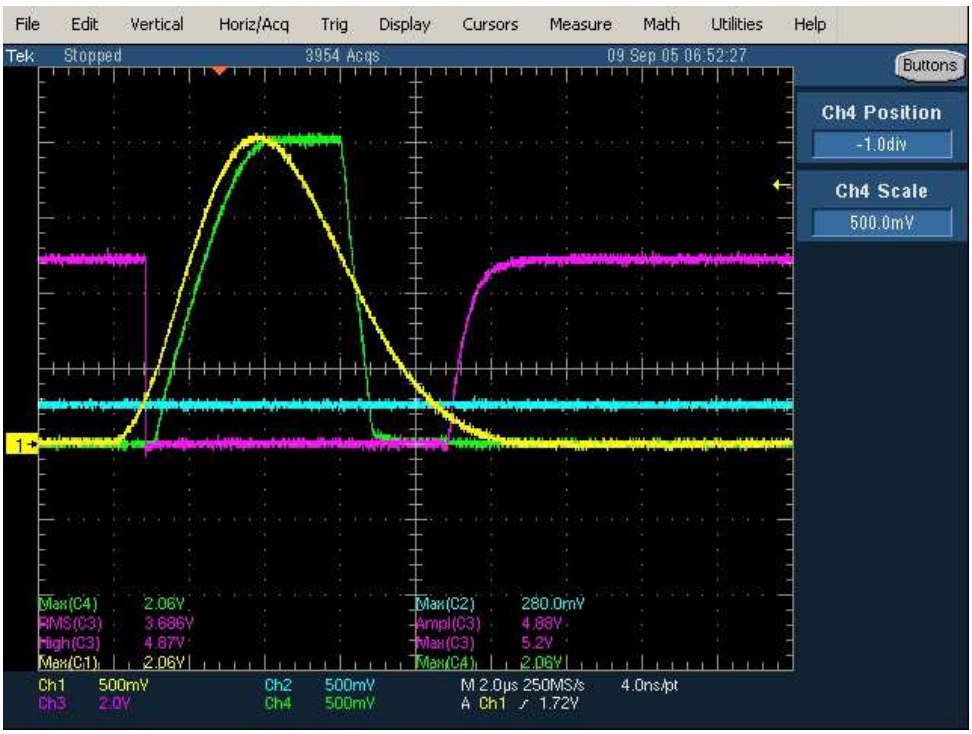

Figure 3.42: Oscilloscope trace of an example pre-flight threshold test. Note that the small ticks in the vertical axis correspond to 100 keV. This gives a large spread in threshold value (cyan) around the main peak of hits recorded in the deposited energy spectra. The yellow shows an injected test pulse with a relatively high energy, the purple shows the discriminator voltage, and the green shows the peak holder keeping track of the maximum voltage of the signal. Taken from ref [29].

Qualitatively it can be seen that there is a large spread in the threshold (cyan), with the majority contained in a range of around 100 keV. This shows a large spread, which is in agreement with the single Gaussian model where the standard deviation predicts 95% of points are contained within a range of 141.6 keV.

These tests did not consider the case where the signal was just above the threshold. Considering the position of the main peak at around 100 keV, it can be said that the majority of points fall within the qualitatively allowed spread of threshold values when the nominal threshold is set to 60 keV. In the future, the threshold can be characterized by outputting the trace of the oscilloscope. This would allow for pre-flight measurements of the threshold, and for tests of the individual diode thresholds too. Then, these models can be verified in-flight by similar calibration runs, with second calibration runs used to fit for degradation.

It was found that the radiation monitor on LISA Pathfinder was able to provide daily estimates

of the solar attenuation parameter through the mission time to a good agreement with estimates using other monitors in space [15]. In particular, an agreement was found in the estimated flux for two species of GCR particles using the daily coincident counts and an IREM-PAMELA correlation. Furthermore, the RM on Pathfinder was sensitive enough to measure modulations at integer fractions of the 27 day solar rotation period. These features are thought to be associated with co-rotating interaction regions and heliospheric current sheet crossings.

There was some ambiguity about the shape of the threshold. It is thought that the shape of the threshold could be more complex than assumed in this model. The complex circuitry in the on board processing means that a non-Gaussian threshold shape could be possible, and could to some extent account for the tension in the leading edge of the main peak.

There was also tension in the simulated and measured Helium peak positions. One possible explanation of this is the physics list used in the GEANT4 portion of the model did not adequately simulate the helium physics at the energies sampled. Another explanation could be a problem with the geometry used. This would also affect the simulated main peak, which is primarily determined by proton interactions. However the main peak is also primarily affected by the choice in threshold shape, making the parameters correlated with each other and determination of their values non-trivial.

The correlation between test mass charging and solar attenuation of GCRs was shown to be a strong function of several parameters, and so projections of charging rates to LISA could not be made at this time. A further investigation would have to be done to look at the dependence of charging rates on the test mass potential and the force authority. Tentative results suggest a possible correlation, though dependence on configuration is too strong to say for sure.

Future projects linking the space weather at the first Lagrange point with test mass charging rates can now use the solar attenuation measured in-situ. This will facilitate a more realistic model with smaller systematic errors as no extrapolation of GCR flux to the position of the spacecraft needs to be made. Although complicated, some hints have been found at the charging rates when considering specific configurations of test mass potentials and suspension forces. Furthermore, understanding the temporal behaviour of the GCR variations and the

consequent fluctuations in the TM charging will be invaluable input with the LISA charge induced acceleration noise model.

Chapter 4

Measuring the Gravitational Constant in Space

4.1 Introduction

In the 17^{th} century, Newton extensively tested the application of an inverse-square law to gravity. He hypothesized that the force exerted on a test particle by a nearby body is proportional to the body's mass and inversely proportional to the square of the distance between them [96]. Later, in 1793, Cavendish arguably measured the constant of proportionality, or 'big G', for the first time using an idea and apparatus inherited from John Mitchell. In today's units, his measurement corresponds to 6.74×10^{-11} $\mathrm{m^3 kg^{-1} s^{-2}}$ [37].

Despite the success of the theory through the centuries, modern physics has seen some disagreement with the inverse-square law in systems that should obey these dynamics. For example, the rotation curves of galaxies [105] diverge from the expected behaviour, indicating that there could be new physics at these scales. Given the extensive tests of the inverse-square law at Earth scales, it makes sense to treat these divergences as a next-to-leading-order correction in the gravitation constant. However, measuring big G is notoriously difficult and as a result, G is one of the most poorly constrained constants to date.

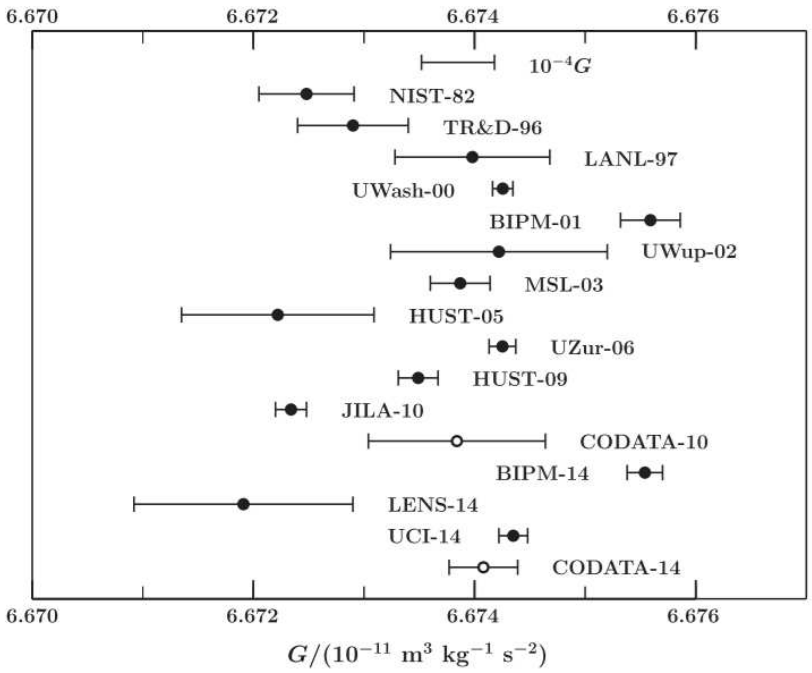

Figure 4.1: Selection of modern measurements of the gravitational constant, taken from ref [94]. Even though most measurements have relative uncertainties at parts in ten thousand or less, there is a spread between measurements at parts in a thousand.

To demonstrate this, Figure 4.1 shows a selection of recent measurements collated in the 2014 CODATA report of physical constants [94]. In each method, an attractor mass sources a change in force on a measurement mass, which can then be used to extract G using the inverse square law. Notably, the most competitive measurements with relative uncertainties at parts in 10^5 show inconsistencies between each other at parts in a thousand. The CODATA reported value is $6.67408 \pm 0.00031 \times 10^{-11}$ $\mathrm{m^3 kg^{-1} s^{-2}}$, and takes the disagreement into account with a relative uncertainty of $\sim 0.005\%$. Finding new ways to measure G and reduce the spread is becoming more important as the search for new physics continues.

As other experiments such as MICROSCOPE [117] go to space to test the axioms of GR that manifest in the inverse-square law, it makes sense to ask if gravity gradiometers can also measure the low energy limits of relativity. To test this concept and identify obstacles for future missions to address, an attempt was made to measure the gravitational constant for the first time in space by Pathfinder.

There are two limitations on sensitivity for Pathfinder to measure G. The first is that the absolute separation of the two test masses is only known to parts in a thousand. The second is that the main observable, Δg_x, cannot be used as it would include both the source mass motion and the test mass response. This means that the electrostatic suspension forces have to

be used instead of the full sensitivity of the interferometry system to measure the signal. Given these limitations, a competitive measurement of G is not possible. However, this experiment will provide invaluable lessons to be learned, paving the way for future space based laboratories dedicated to measuring G.

4.2 Method

The concept for a measurement of G has been discussed for a number of years within the collaboration. However, it was only when the nominal mission extension was confirmed that the experimental procedure, from formulation to execution on the spacecraft, was formalized internally [118]. The specific contribution made to this experiment was data analysis after the experiment was run.

The method used one of the test masses, called the 'source mass', to induce a change in absolute acceleration of the second test mass. This is done by periodically moving the source mass between extreme positions in the x direction, with the change in acceleration of the test mass proportional to the total distance moved by the source mass. The signal is then measured by a change in suspension force on the test mass required to hold it stationary.

TM2 was chosen for all but one signal run as the source mass. It was displaced from the center of the electrode housing by varying amplitudes in a square wave. At each position, the source mass was left to dwell for around twenty minutes while the response of the system settles to a stable state. This procedure is shown in Figure 4.2, which was taken from the experiment summary document [118] outlining the motivation for the experiment.

In order to optimize the accuracy of the electrostatic forces, the thrusters that keep the spacecraft on orbit were switched off. This meant that the spacecraft moved off its orbit in a 'solar sail'; effectively sailing on the flux of photons from the sun. The force on the spacecraft due to this flux, known as the solar radiation pressure (SRP) force, is large and variable over a typical time frame for several signal runs. It also causes the spacecraft to roll with respect to the Sun

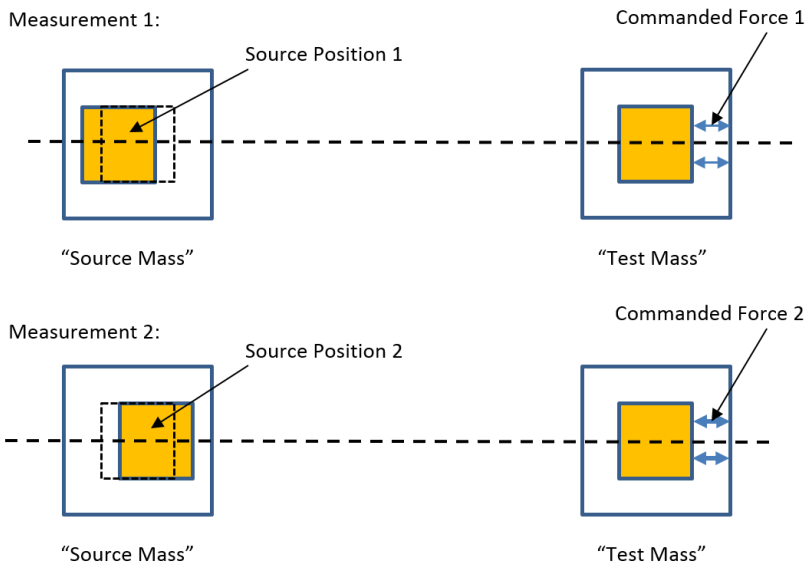

Figure 4.2: Cartoon outline of the experimental method to measure Newtons constant. Taken from ref [118].

pointing direction, as demonstrated by Figure 4.3 showing typical spacecraft angles through a solar sail.

The star tracker provides an estimate of these angles with respect to a fixed frame, which is used to calculate the components of the centrifugal and SRP forces in the x-axis, $F_{Cent,x}$ and $F_{Rad,x}$ respectively, as the spacecraft rotates. The displacement of the test mass with respect to the spacecraft, o_{TM}, is measured by the optical metrology system (OMS), and taking a second time derivative of this gives the total test mass acceleration $\ddot{o}_{TM}$. Denoting the acceleration of the test mass due to the surrounding spacecraft material as $a_{Grav,SC}$, and the acceleration of the test mass due to the source mass explicitly as $a_{Grac,SM}$, the residual acceleration of the test mass is given by

$$a_{TM} = \ddot{o}_{TM} + \frac{g_{SM}}{M_{SC}} F_{SM,x} - \frac{g_{TM}}{m_{TM}} F_{TM,x} - \frac{g_{TM}\Delta t}{m_{TM}} \frac{dF_{TM,x}}{dt} - \frac{1}{m_{TM}} F_{Rad,x} - \frac{1}{m_{TM}} F_{Cent,x} - \omega_{TM}^2 o_{TM} + a_{Grav,SC} + a_{Grav,SM} \tag{4.1}$$

In this expression, the reaction of the control loop to changes in the OMS read of the test mass position is given by $\omega_{TM}^2 o_{TM}$. $F_{TM,x}$ is the total applied electrostatic force on the test mass in the x-direction to keep it centred, which fractionally changes in response to the source mass movement. A time delay Δt for the reaction time of the control loop is also included and approximated by a first derivative of the electrostatic force. A recoil acceleration of the

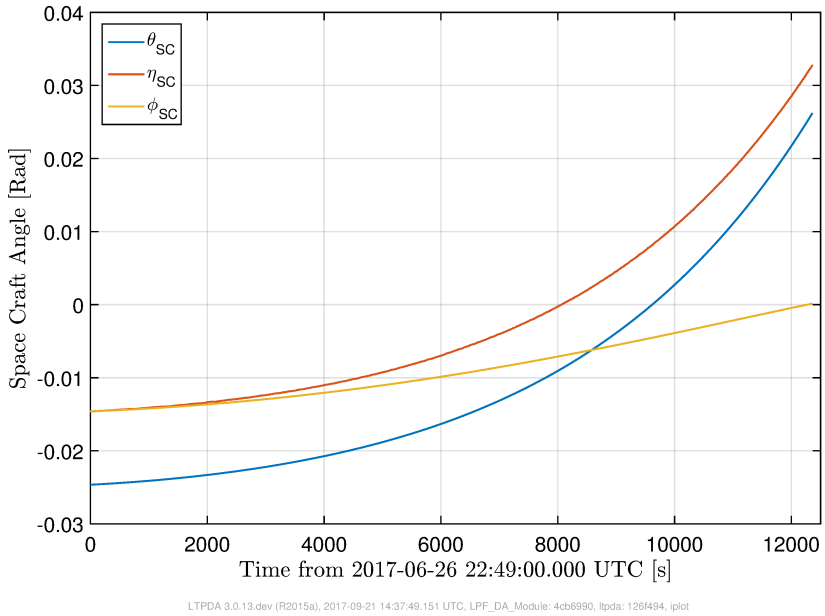

Figure 4.3: Typical spacecraft angles as recorded by the star tracker through a solar sail.

spacecraft is taken into account by the total applied electrostatic force on the source mass in the x direction, $F_{SM,x}$, diluted by the spacecraft mass M_{SC}. Each electrostatic force is scaled by a gain, g_{SM} and g_{TM}, which correct for systematic errors in the on board processing of requested forces.

During a solar sail, the source mass moved by a relatively large distance (± 600 μm, ± 900 μm, or ± 1200 μm) compared to nominal mission experiments. In order to safely move the source mass without risking a re-grab of the masses by the control system, the electrostatic sensors were switched to 'wide range' during the move. This decreased the precision of the position readings by the electrodes, but did not saturate them. Once in place, the electrostatics were moved back to 'high resolution', where the force readings were much more accurate.

In each solar sail, there was enough time to slew the source mass to the pre-set maximal position four times, alternating between positive and negative displacements from the central housing position. Much of the dwell time in high resolution is cut during the processing as transients take time to die out. An example of the source mass movement in a single solar sail is shown in Figure 4.4. The blue line shows the more precise OMS readout, while the red shows the electrostatic readout. Clearly seen are step changes in the red line corresponding to transitions

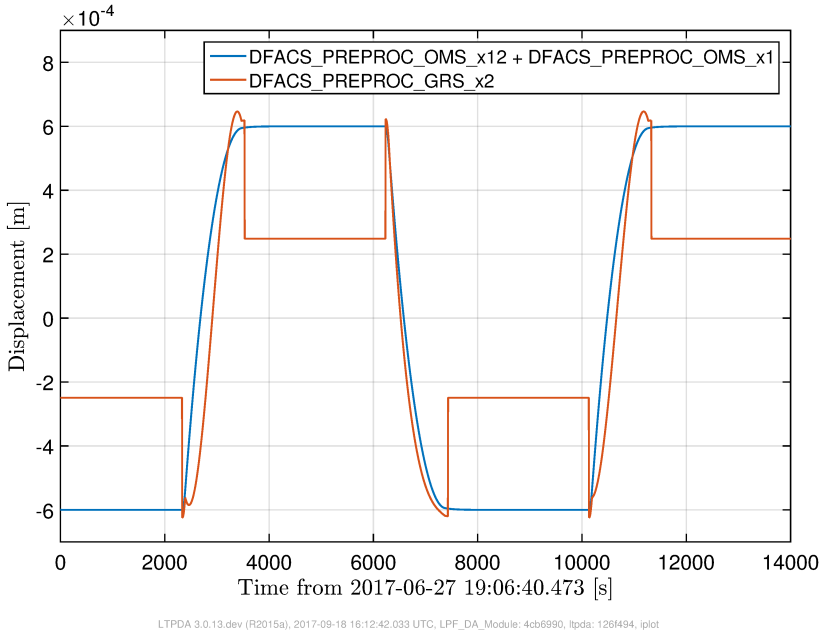

Figure 4.4: First solar sail readout of the source mass position using the optical metrology system (OMS) and the electrostatic sensors (GRS). In each sail, the maximal position is reached four times, with two subsequent positions leading to a single estimate of G.

between wide range and high resolution.

In order to reduce the number of fit parameters, a difference is taken between the positive and negative displacements. The background acceleration $a_{Grav,SC}$ is constant since the test mass is held stationary, and therefore cancels. A superscript i, where $i = \{1, 2\}$, is added to the terms in equation 4.1 to denote the source mass position in either positive or negative displacement. Taking the difference between positions 2 and 1, the change in acceleration on the test mass due to the change in relative position of the source mass is then

$$\begin{aligned}\delta a_{TM} =&(\ddot{o}^{(2)}_{TM} - \ddot{o}^{(1)}_{TM}) + \frac{g_{SM}}{M_{SC}}(F^{(2)}_{SM,x} - F^{(1)}_{SM,x}) - \frac{g_{TM}}{m_{TM}}(F^{(2)}_{TM,x} - F^{(1)}_{TM,x}) \\ &- \frac{g_{TM}\Delta t}{m_{TM}}\frac{d(F^{(2)}_{TM,x} - F^{(1)}_{TM,x})}{dt} - \frac{1}{m_{TM}}(F^{(2)}_{Rad,x} - F^{(1)}_{Rad,x}) \\ &- \frac{1}{m_{TM}}(F^{(2)}_{Cent,x} - F^{(1)}_{Cent,x}) - \omega^2_{TM}(o^{(2)}_{TM} - o^{(1)}_{TM}) + (a^{(2)}_{Grav,SM} - a^{(1)}_{Grav,SM})\end{aligned} \tag{4.2}$$

Where $(a^{(2)}_{Grav,SM} - a^{(1)}_{Grav,SM})$ is the signal term, which takes a derivative form of the inverse square law

$$a^{(2)}_{Grav,SM} - a^{(1)}_{Grav,SM} = \frac{2Gm_{SM}}{r^3}\Delta r \tag{4.3}$$

In this expression r is the separation between the test mass and source mass in their electrostatic centres, and Δr is the total displacement between two high resolution positions in the signal run (either 1.2 mm, 1.8 mm or 2.4 mm). m_{SM} is the mass of the source mass, and G is Newton's constant. The point mass approximation can be corrected for using a factor calculated by a numerical integration simulation. However, given the dimensions of the masses and their separation, this correction is only important at the parts in a thousand level, and so will be neglected for now.

The magnitude of some of the terms in equation 4.2 are already known *a priori* as similar terms enter into the observable Δg_x of the nominal mission. The gains were measured around 1 for both test masses, the stiffness around 10^{-7} s^{-2} and the time delay at milliseconds. This puts the terms with g_{SM}, ω_{TM}^2 and Δt around 10^{-15}-10^{-14} ms^{-2}, which is well below the signal level of about 10^{-12}-10^{-11} ms^{-2}. Since the absolute separation between the masses is known at parts in 10^3, it is possible then to neglect these terms. Equation 4.2 then becomes

$$\begin{aligned}\delta a_{TM} =&(\ddot{o}_{TM}^{(2)} - \ddot{o}_{TM}^{(1)}) - \frac{g_{TM}}{m_{TM}}(F_{TM,x}^{(2)} - F_{TM,x}^{(1)}) - \frac{1}{m_{TM}}(F_{Rad,x}^{(2)} \\ &- F_{Rad,x}^{(1)}) - \frac{1}{m_{TM}}(F_{Cent,x}^{(2)} - F_{Cent,x}^{(1)}) + (a_{Grav,SM}^{(2)} - a_{Grav,SM}^{(1)})\end{aligned} \tag{4.4}$$

The remaining parameters g_{TM}, $F_{Rad,x}^{(2)} - F_{Rad,x}^{(1)}$ and G are fitted for in three stages. First, an injected sinusoidal force is used to fit the control loop response in frequency space, giving the gain g_{TM}. Then a 'blank run', where the experiment is performed with no source mass displacement, is used to fit for the SRP force as the signal term cancels. Finally, the signal runs are used to fit for G directly.

4.2.1 Fitting for the gain

The gain was fitted using a Markov Chain Monte Carlo (MCMC) method in frequency space. The source mass was moved to +1.2 mm and a sinusoidal signal at 30 mHz and then 10 mHz was injected into the electrostatic force on the test mass. The response of the system was recorded while in high resolution, and the terms that respond to the injected force on the test

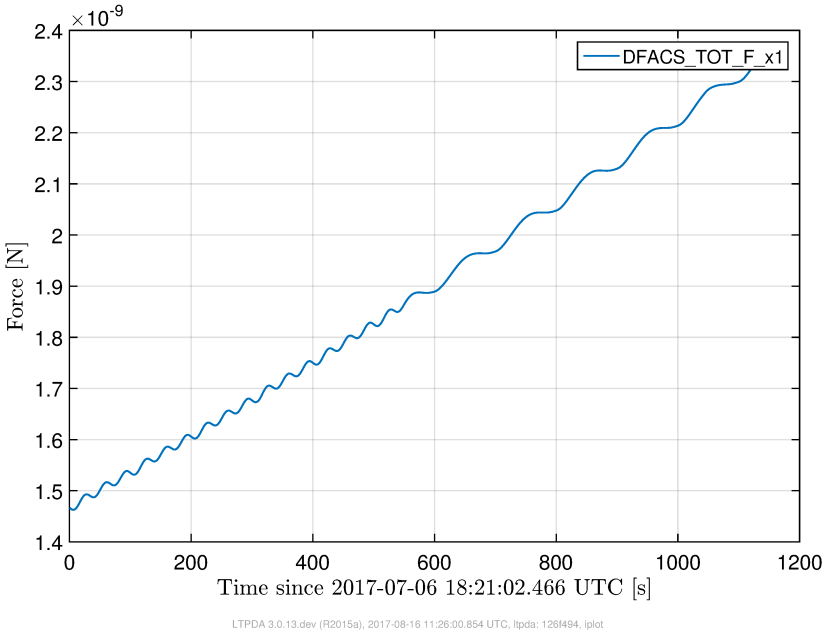

Figure 4.5: Example of the injected calibration signal into the total force acting on the test(measurement) mass. Two frequencies are used at 10mHz and 30mHz.

mass, namely $F_{TM,x}$ and $\ddot{o}_1$, are moved to Fourier Space using a power spectral density (PSD). The remaining terms in equation 4.1 can be omitted from the fit as they have no frequency space contribution to the response.

Figure 4.5 shows the injected calibration tone in the force on the test mass. The gradual background drift is approximately constant over a much longer time, and therefore enters as a gradual lift at lower frequencies in the force PSD. The fit is performed on a specific range of frequencies, from 5 mHz to 35 mHz, so that the results focus on the response to the calibration tone and minimize the effects of the gradual background.

Figure 4.6 shows the PSD of the total force on the test mass. Clearly visible are the excesses at 10mHz and 30mHz due to the injected calibration tones. The drifting background is also visible at lower frequencies.

The fitting algorithm chooses a trial value for the gain, and computes the model

$$a_{TM}^{inj} \approx \ddot{o}_{TM} - \frac{g_{TM}}{m_{TM}} F_{TM,x}^{inj} \tag{4.5}$$

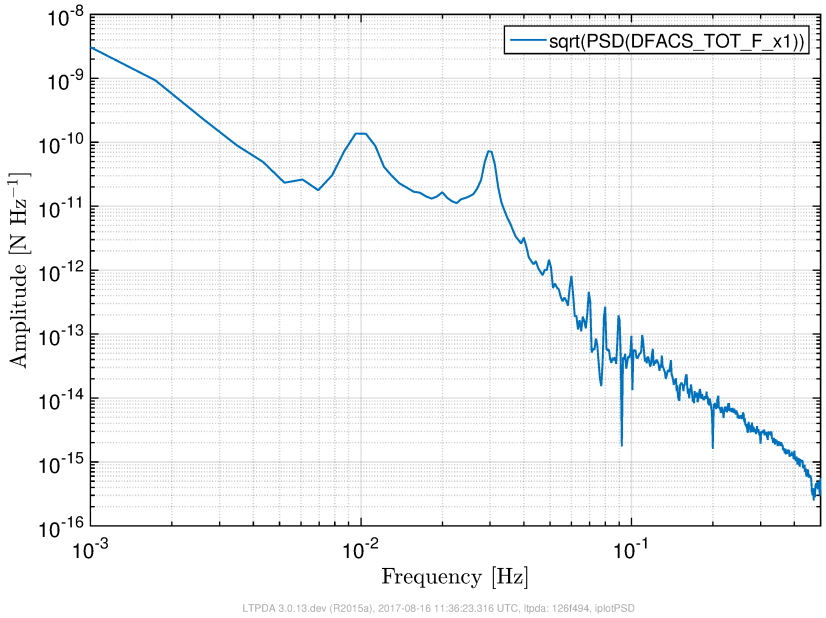

Figure 4.6: PSD of the injected calibration signal into the total force acting on the test mass.

before subtracting it from the data with the injection response. It compares the residuals of this subtraction to a section of the blank run in frequency space. In theory, once the correct gain is chosen the residuals should be equal to the blank run, where no injections are present.

The resulting posterior distribution for the gain is shown in Figure 4.7. The red curve shows a Gaussian fit to the binned posterior chain in blue. The dashed lines show the 1σ region either side of the mean posterior value, indicated by the solid red vertical line. The lower plots show the difference between the Gaussian fit and the posterior histogram, with root-n error bars from the histogram bins. The mean value was found to be $g_{TM} = 1.083 \pm 0.0103$, in agreement with nominal mission measurements of 1.0778 ± 0.0001.

4.2.2 Centrifugal Force

During a solar sail the spacecraft rotates due to a torque arising from a small initial angular offset to the SRP force. The rotational motion causes the test masses to experience a centrifugal force which can be calculated exactly. Euler angles are defined for the spacecraft as θ_{SC}, η_{SC} and ϕ_{SC} for rotations around the x, y and z axes respectively. Constructing the angular

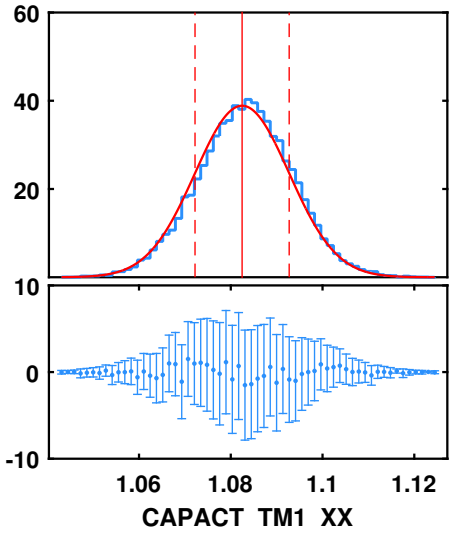

Figure 4.7: Posterior distribution for g_{TM} obtained using a Monte Carlo Markov Chain to fit the response of the system to an injected force. The upper plot shows the binned posterior along with a Gaussian distribution fit to the distribution. The solid red shows the mean, while the dashed line shows the 1σ uncertainty either side of the mean. The lower plot shows the residual after taking the difference between the binned data and the Gaussian model

velocity vector $\vec{\omega}^{(i)} = \left(\dot{\theta}^{(i)}_{SC}, \dot{\eta}^{(i)}_{SC}, \dot{\phi}^{(i)}_{SC}\right)$, where i indexes the segment of high resolution data being considered, the centrifugal force on the test mass is then

$$\vec{F}^{(i)}_{Cent} = \frac{1}{2} m_{TM} \vec{\omega}^{(i)} \times \left(\vec{\omega}^{(i)} \times \vec{d}\right) \tag{4.6}$$

where $\vec{d}$ is the separation vector of the test masses in the coordinate frame of the spacecraft. This assumes that the test masses are placed symmetrically either side of the spacecraft centre of mass. The difference between centrifugal forces in subsequent high resolution times is small enough that this is a good approximation.

In practice, $\vec{F}_{Cent}$ is not a constant, but an increasing force through the solar sail as the SRP force continually spins up the spacecraft. The centrifugal term is therefore the difference in the centrifugal force acting on the test mass at different times of the solar sail; $\vec{F}^{(i+1)}_{Cent} - \vec{F}^{(i)}_{Cent}$. The magnitude of this difference grows, and so becomes more important later in the solar sail. Figure 4.8 shows the centrifugal force calculated for the blank run.

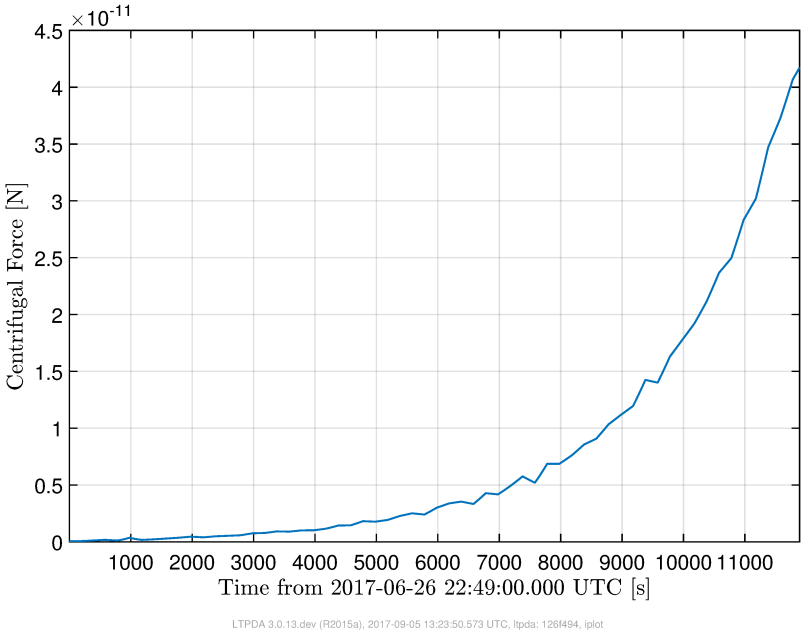

Figure 4.8: Centrifugal force (x-axis component) calculated for a solar sail with no source mass movement.

4.2.3 Fitting for the Solar Radiation Pressure

The largest component of the test mass acceleration during a solar sail is the component of the SRP force in the test mass - source mass axis. Assuming the magnitude of the force is constant through a solar sail and directed in the negative z direction only (radially away from the Sun), it is possible to use the spacecraft angles to project the force in the test mass - source mass axis.

Each data point of the spacecraft angles is treated as a new, rotated frame with coordinates (x', y', z'). The component of the SRP force in the x' axis is then

$$F_{Rad,x'} = \left(\cos(\theta_{SC})\sin(\eta_{SC})\cos(\phi_{SC}) - \sin(\phi_{SC})\sin(\theta_{SC})\right) F_{Rad,z} \tag{4.7}$$

where the spacecraft angles are defined in the same way as before, and $F_{Rad,z}$ is the constant, un-projected force.

$F_{Rad,z}$ can be fitted for using the blank run, where the signal term in equation 4.2 cancels. Longer stretches of usable data are also possible as the whole solar sail is performed in high

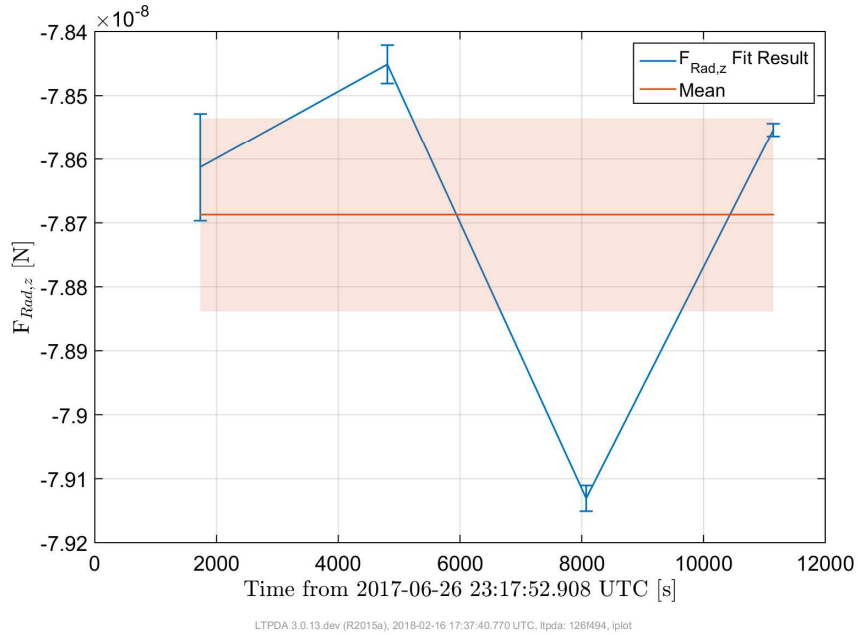

Figure 4.9: Fit results for the radiation pressure force. The blank run was split into eight segments, with each pair of data segments giving one fit result (blue). The final constant is then the mean of the four fit results (red), with an associated 1σ uncertainty (shaded red) determined by the quadrature sum of the individual uncertainties plus the standard deviation of the scatter.

resolution. The data are divided into eight segments, where equation 4.2 is calculated without the SRP force term to give the pre-fit acceleration. For each segment, the combination of angles in equation 4.7 is calculated, and the difference between pairs of segments taken. A fit is performed for a constant $F_{Rad,z}$ that minimizes the sum of $(F^{(2)}_{Rad,x'} - F^{(1)}_{Rad,x'})/m_{TM}$ with the pre-fit acceleration segments.

Figure 4.9 shows the four results of this fit for each pair of data segments. The blue points show each fit result and the red line gives the mean between them of $F_{Rad,z} = 7.8687 \pm 0.0175 \times 10^{-8}$ N. This result represents the force on the test mass to give it the same acceleration as the spacecraft as it rolls with the SRP force. Therefore the force on the spacecraft can be calculated by multiplying by the ratio of the spacecraft mass $\sim$ 420 kg to the test mass mass $\sim$ 2 kg, giving 16.9 μN. This excludes an infrared force of around 7 μN and differs from the quoted value in pre-flight estimates of around 20 μN (excluding infrared component). Note the descending span in error bars as the fit becomes more sensitive to the radiation pressure force. This is due to the combination of angles starting flat and increasing toward the end of the solar sail.

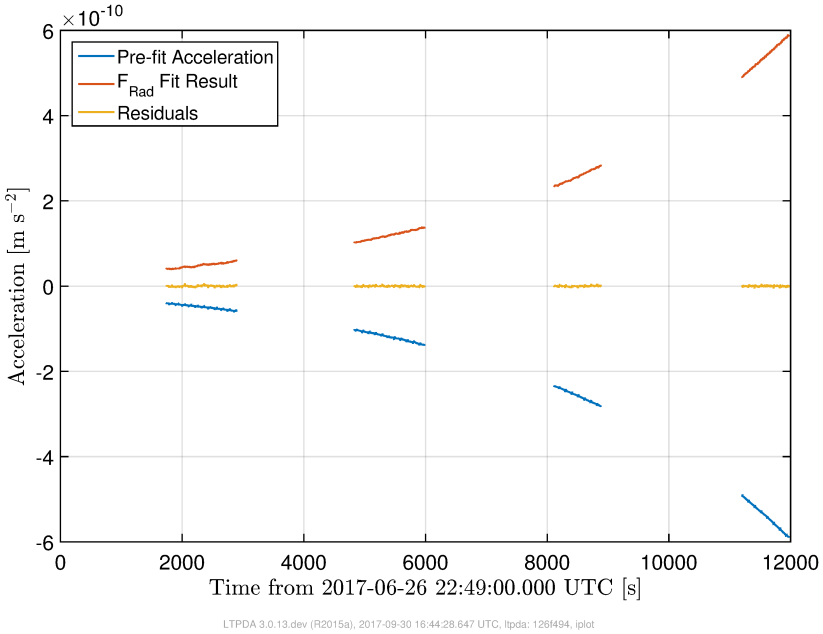

Figure 4.10: The blue data shows the sum off all the terms in equation 4.2 except the radiation pressure force term. The red curve shows the resulting force projected into the x direction from the fit. The yellow data shows the residuals after summing the red and blue data.

Figure 4.10 shows the four segments of differences taken. The blue data show the sum of all the contributions to the test mass acceleration in equation 4.2 except the SRP term, with the signal term set to zero. The red data show the fit results for $F_{Rad,z}$ and the yellow data show the residuals after the blue and red are summed.

Figure 4.11 shows a close up of the residuals. It can be seen that they are consistent with zero, which indicates the goodness of the fit. However, the signals considered here are expected to be around $0.6 - 1.2 \times 10^{-11}$ ms^{-2} depending on the source mass displacement, indicating that the noise within high resolution stretches may present a problem later given they span a significant proportion of the signal.

4.2.4 Fitting for the Signal

The signal run was performed ten times, with each solar sail comprising four segments of high resolution data, giving two independent fits for G per sail. The last solar sail was only half as long in length, only allowing for one fit for G. This gave a total of nineteen signal fits, 7 at 1.2

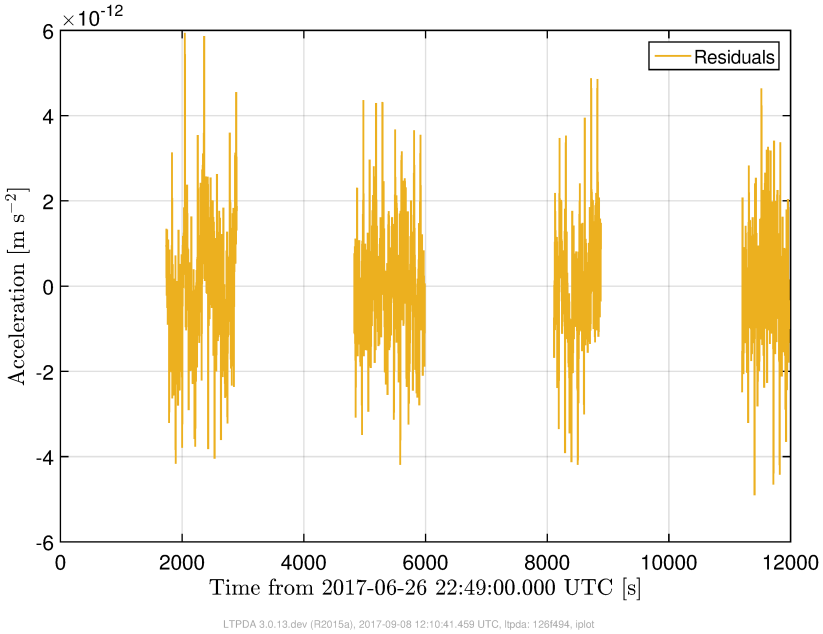

Figure 4.11: Close up of the residuals after summing the pre-fit acceleration and the fit results for the radiation pressure force. The span of the residuals is comparable with the signal strength from a 600 μm amplitude signal.

mm, 2 at 900 μm and 10 at 600 μm source mass displacement. The final result will be a mean of the nineteen measurements with an added uncertainty of a standard deviation. This will account for assumptions of constant solar radiation pressure between signal runs and through the rotation of the spacecraft.

Using the fit results from the injection calibration and the blank run, all the terms except the signal in equation 4.2 can be calculated for the pre-fit acceleration. A Least Squares Covariance (LSCOV) method in LTPDA is used to fit for G in the signal term given by equation 4.3, such that δa_{TM} is minimized.

The resulting nineteen fits for G are shown in Figure 4.12. The yellow points show each fit result, with corresponding error bars from the fits that account for statistical and some systematic uncertainties in each measurement. The red line shows the mean of the measurements, and the shaded red area indicates the uncertainty on the mean due to both the quadrature sum of the individual error bars and a standard deviation from the scatter of the points. The scatter increases the error from less than 1% to 5.2% and shows that random errors in each data segment dominate the relative uncertainty.

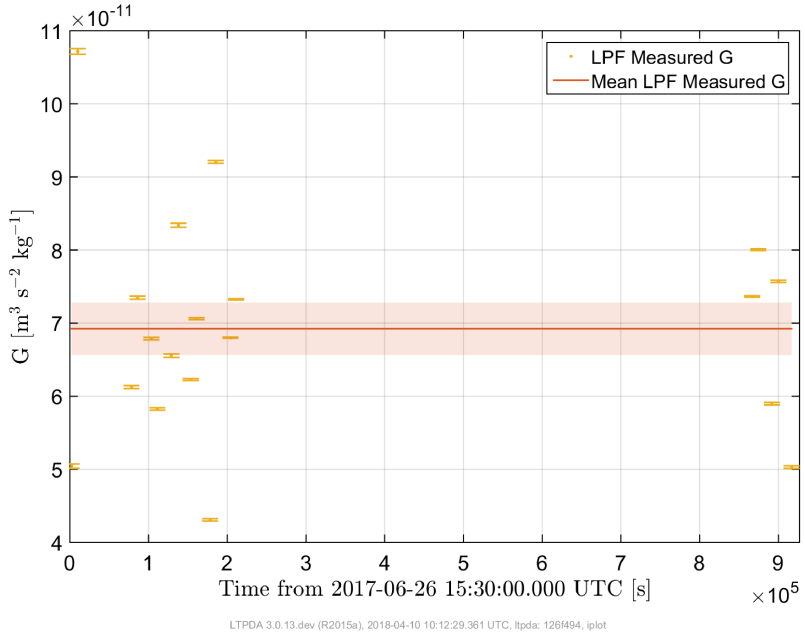

Figure 4.12: Resulting 19 independent fits for G (yellow). Taking the mean (red) of the independent fits gives a larger uncertainty (shaded red) as a standard deviation of the individual points is added to the quadrature sum of the individual uncertainties. This accounts for errors incurred by assuming the SRP force is constant.

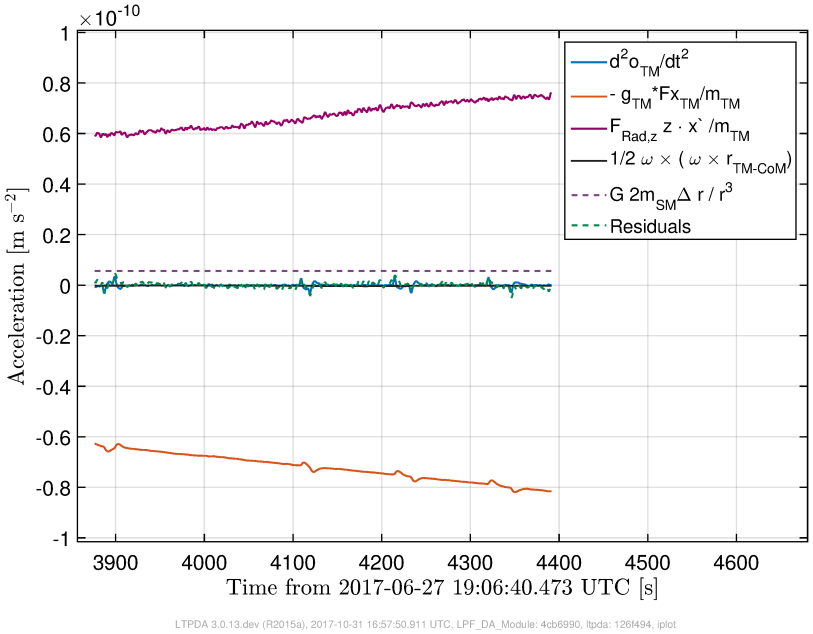

Figure 4.13: Breakdown of each component from equation 4.2 contributing to the acceleration of the test mass during a signal run with 600 μm source mass displacement. Note that this example is taken from the beginning of a solar sail where the amplitude of the centrifugal and SRP components are smallest.

From these results, the gravitational constant was measured to be $6.93 \pm 0.36 \times 10^{-11}$ $m^3kg^{-1}s^{-2}$, which is in agrement with the CODATA reported value of $6.67408 \pm 0.00031 \times 10^{-11}$ $m^3kg^{-1}s^{-2}$. Although the relative error of 5.2% is high, the experiment highlighted some difficulties that future experiments similar to Pathfinder will need to overcome in order to measure G in space. In particular, the degree to which the SRP force needs to be known in each solar sail. To demonstrate this, Figure 4.13 shows the components of equation 4.2 along with the residuals. It emphasizes the weakness of the signal relative to the other components of δa_{TM}, especially the SRP term. A fluctuation in $F_{Rad,z}$ below 1% would be around the same order of magnitude as the signal, and therefore can heavily affect the end result. In order to mitigate this effect and reduce the scatter, the SRP force needs to be measured more often or within each solar sail.

4.3 Investigating the Solar Radiation Pressure

In order to gauge the effects of the assumptions made about the SRP force, the results for G were plotted against the change in angular projection of the force, or Δangles for short, in Figure 4.14. There is possibly a weak correlation, with the best fit line shown in red. There are also two groups of points at lower and larger Δangles, corresponding to evaluations at the beginning and ends of solar sails. The spread in points is visibly larger in the measurements at later Δangles. This could be due to the larger change in Δangles amplifying the difference in the approximation for and the true value of the SRP force.

One method to explore the effects of the spacecraft rotation on the fits is to split the results for $F_{Rad,z}$ into early and late times of the solar sail. This should capture any variation in effective SRP force due to a change in geometry of the spacecraft as it rotates relative to the direction of the force. Taking the first two and last two fit points gives an estimate for $F_{Rad,z}$ in the early and late parts of the solar sail.

The two resulting estimates for the force are shown in Figure 4.15. Implementing these values in the signal runs, a new estimate for G and its relative error can be found, as shown in

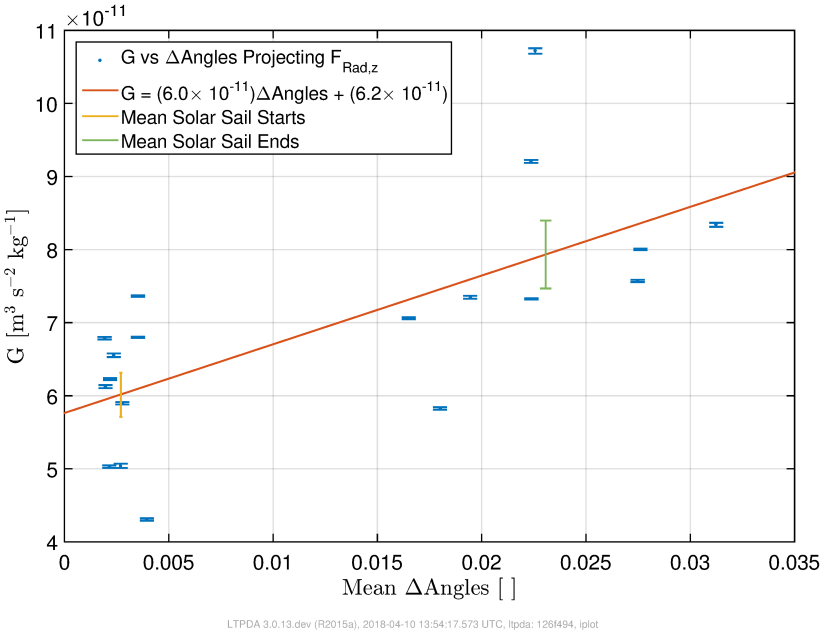

Figure 4.14: G as a function of the change in angular projection of the radiation pressure force into the source mass - test mass axis, given by the sines and cosines of equation 4.7. There is a weak correlation between G and the change in projection angles, possibly indicating the limitations of the assumptions about reflectivity and the magnitude of the force itself.

Figure 4.16. The new mean is reduced to $6.23 \pm 0.26 \times 10^{-11}$ $\mathrm{m^3 kg^{-1} s^{-2}}$, with a relative error of 4.2%.

The reduction in relative error from 5.2% to 4.2% reflects the increased number of parameters describing the measured data and highlights that the uncertainty in the SRP force is partly responsible for the scatter. This also quantifies the dependence of the final result on this term; although the early and late estimates have changed $F_{Rad,z}$ by only 0.25%, the final estimate for G was changed by 10%. Figure 4.17 shows each fit for G against the means of the angular projections, along with the new line of fit.

The averages of the two clouds of points now agree with each other to within their uncertainties. The slope of the line of best fit has also been reduced, indicating that taking two means for $F_{Rad,z}$ has accounted for this weak correlation. However, the new mean value of G has reduced further from the CODATA value, and the 1σ uncertainty now does not include the CODATA value. This deviation is likely due to the scatter in the measurements of $F_{Rad,z}$, and the lower than expected mean value compared to pre-flight estimates.

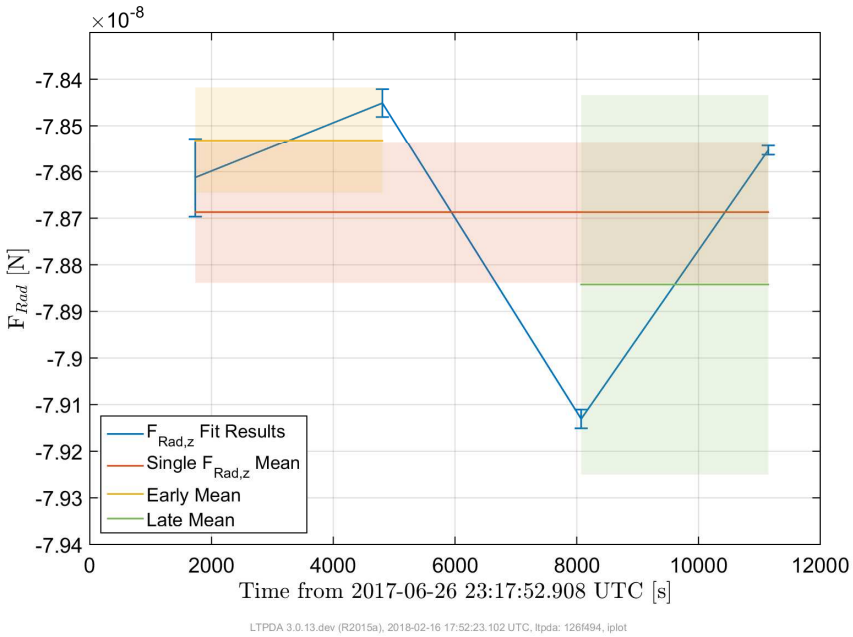

Figure 4.15: Fit results from the blank run for $F_{Rad,z}$. The red line shows the overall mean, while the yellow and green show the early and late means respectively. These will be used to explore changes in the effective radiation pressure force through a solar sail.

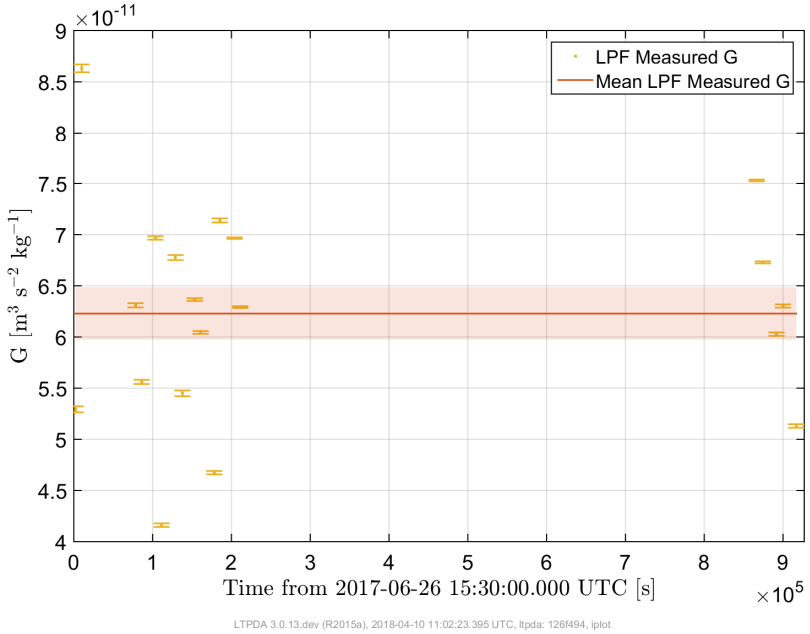

Figure 4.16: Resulting G measurements after using the early and late averages for the SRP force term. The solid red line shows the global mean, with the red shaded region showing the uncertainty due to both statistical uncertainties and the scatter between points.

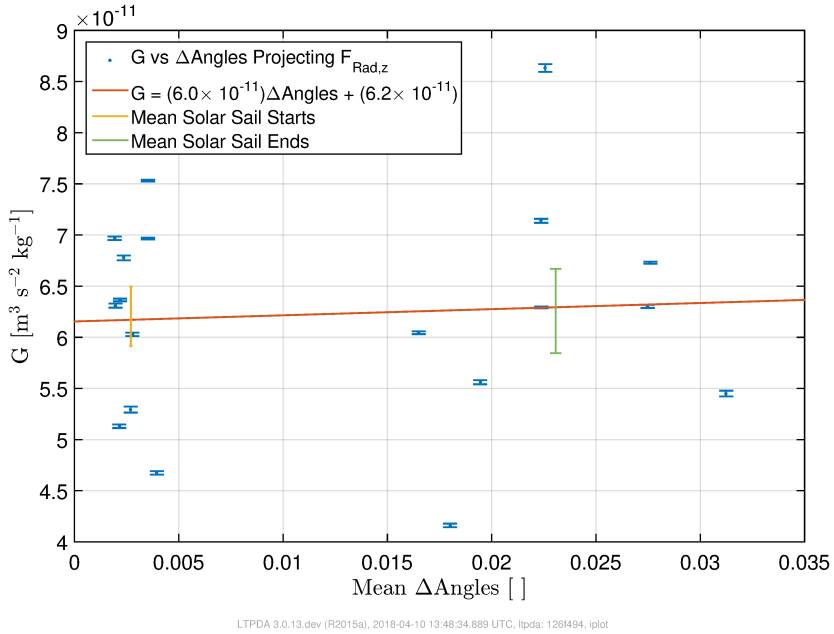

Figure 4.17: G plotted as a function of the projection operator. The significant difference between measurements earlier and later in solar sails is no longer seen after using two values for the radiation pressure force.

It is possible to estimate the fluctuations possible in the SRP force through typical experimental time scales. Figure 4.18 shows the change in z component of the commanded force on the spacecraft in the interim between the two main times the experiment was repeated.

After subtracting the mean in each section of data and filtering, there is an apparent change in the force that is just under the percent level over two to three days. This poses a problem when using the fit results for $F_{Rad,z}$ as a constant for each solar sail: a 0.5% change in $F_{Rad,z}$ causes its term in equation 4.2 to change by 4×10^{-12} ms^{-2}, which changes G by more than 50-67% depending on the source mass displacement. This suggests that according to the thrusters, there is a large enough change in the SRP force to account for a large portion of the scatter.

It is also possible to demonstrate the variability possible by using an estimate of the total solar irradiance (TSI), as measured by the total irradiance monitor (TIM) on the Solar Radiation and Climate Experiment (SORCE) [82]. This estimate of the energy contained by solar photons can be scaled to the distance Pathfinder is from the Sun and converted to changes in power on the spacecraft. Figure 4.19 shows the result using the most up to date data available, which falls short of the experiment time. It shows that the dominant effect changing the radiation power

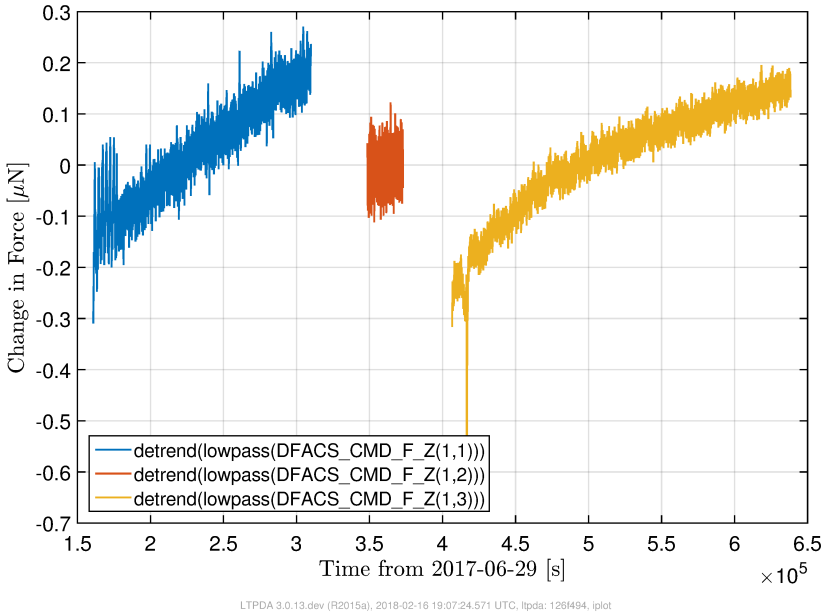

Figure 4.18: Thruster data showing the change in force exerted on the spacecraft in the z direction in the time between the two sets of G measurements. Between sections of data the constant force was modified, causing some transients that were cut.

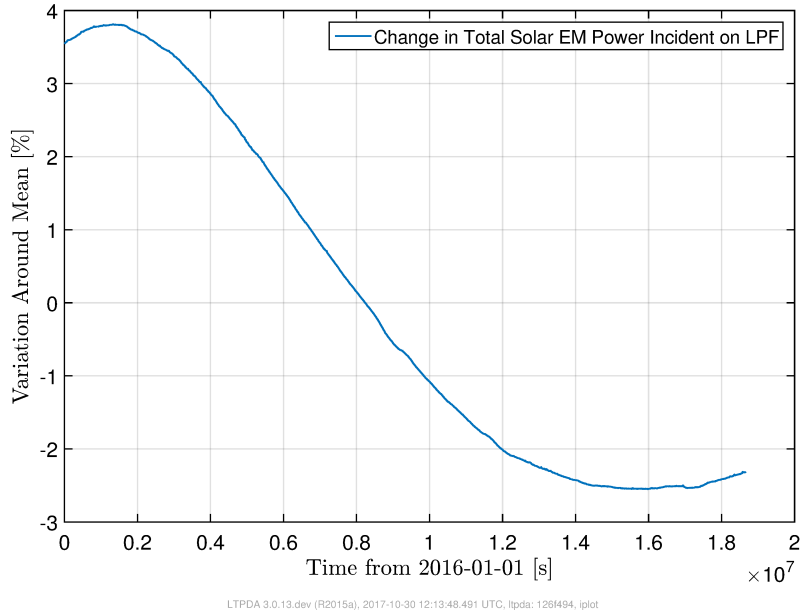

Figure 4.19: Estimate for hourly changes in solar radiation power incident on LISA Pathfinder. Data taken from SORCE/TIM measurements of Total Solar Irradiance. [82]

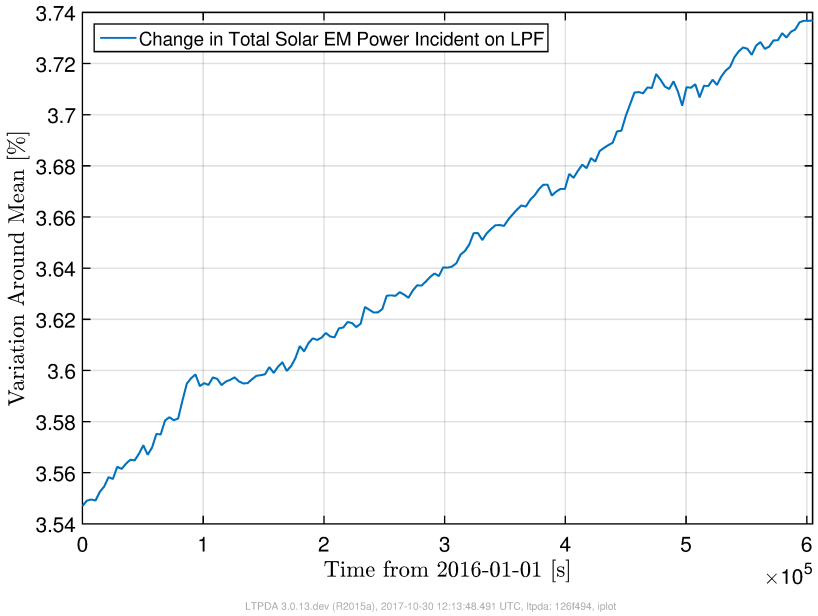

Figure 4.20: Estimate for typical hourly changes in solar power output over a week. Variations of around fractions of a percent are very likely from day to day. This can account for a large fraction of the scatter of G measurements.

on the spacecraft is the proximity to the sun, with smaller fluctuations due to solar activity occurring under the larger trend. Figure 4.20 shows the first week of the change in power data, demonstrating that the possible changes on the hourly scale is above the limit for the constant SRP assumption to be acceptable.

These results show that $F_{Rad,z}$ played a crucial role in this experiment. Furthermore, assumptions about the SRP force have limited the end result of the experiment by increasing the scatter on the independent fits for G. In particular, it has been demonstrated that this term cannot be considered a constant as fluctuations above the critical limit between runs of the experiment are possible.

4.4 Discussion

The final measurement reported here used a standard deviation to account for assumptions about the SRP force $F_{Rad,z}$ and any other source of uncertainty that was not included in the analysis. The standard deviation far outweighed the uncertainties accounted for, increasing the

relative error by several percent.

$F_{Rad,z}$ was found to be $7.869 \pm 0.018 \times 10^{-8}$ N, orders of magnitude above the next force acting on the test mass. Once multiplied by the combination of angles, the resulting radiation pressure term is nearly three orders of magnitude above the peak of the centrifugal force at around 1×10^{-11}N. This means the SRP force needs to be known to, and constant at, better than parts in 10^3. In the case of the blank run, it was found that depending on the segment of the data being considered, the fit for this force can change by 0.25%. Indeed, even the fit value for the whole blank run gave a 2σ confidence interval of 0.4% of the value, an amount that the SRP force was shown to be capable of varying by between solar sails.

The variation of the SRP force depending on the section of the blank run used for the fit also underlines a further assumption about the effective SRP force; the reflectivity of the spacecraft does not change with spacecraft orientation. Although the angles are small through a solar sail, the angular dependence of the reflectivity of the solar array is not known and therefore could also be a source of this uncertainty.

During the nominal mission, the forces on the test masses in the z direction gave an estimate of the SRP force. A derivative could be taken, allowing for a fit per data segment for this force. However, in this experiment the source mass moved by a much larger distance, which meant the sensors in the y and z directions had to be kept in wide-range mode in order to prevent saturation of the electrodes. Consequently, the readings on the electrostatic forces in these axes were too noisy; the reported forces using this method varied above the required accuracy to correct the scatter. Estimates between solar sails are also not possible as the spacecraft has to be rotated back to its initial orientation, causing a large force to register in all degrees of freedom of the test masses.

Another difficulty in the experiment was the presence of periodic glitches in the OMS readout and applied forces on both masses. Figure 4.21 shows a close up of Figure 4.13, where the glitches can be clearly seen about every 100s, putting them in the frequency range of the injection calibration fits. Moreover, they increased the amplitude of the residuals to a significant fraction of the signal.

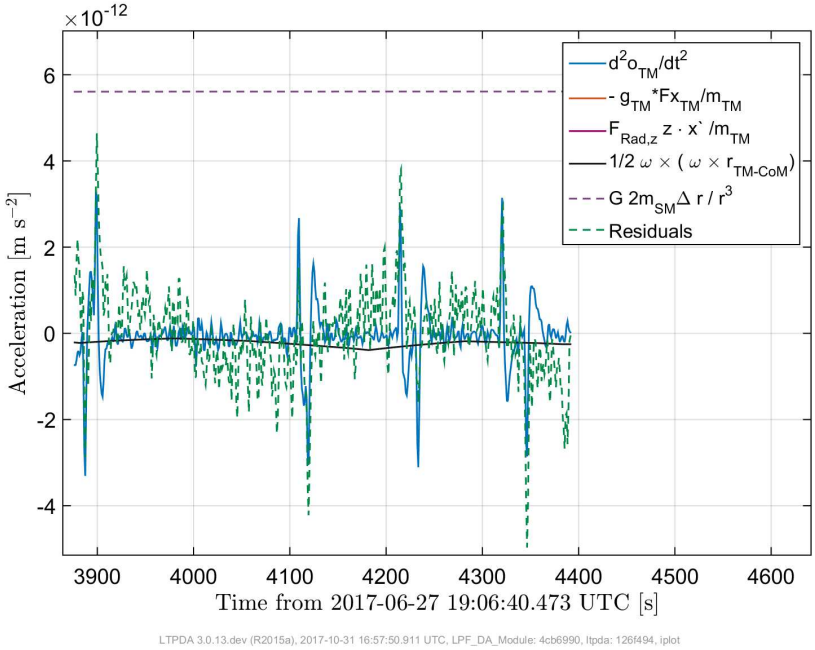

Figure 4.21: Close up of Figure 4.13, showing some of the components of equation 4.2. Clearly seen are the glitches in the second time derivative of the OMS readout of the test mass position. These glitches are also seen on the force readouts, and pollute the injection fits as the frequency of the glitches is within the frequency range of the fit.

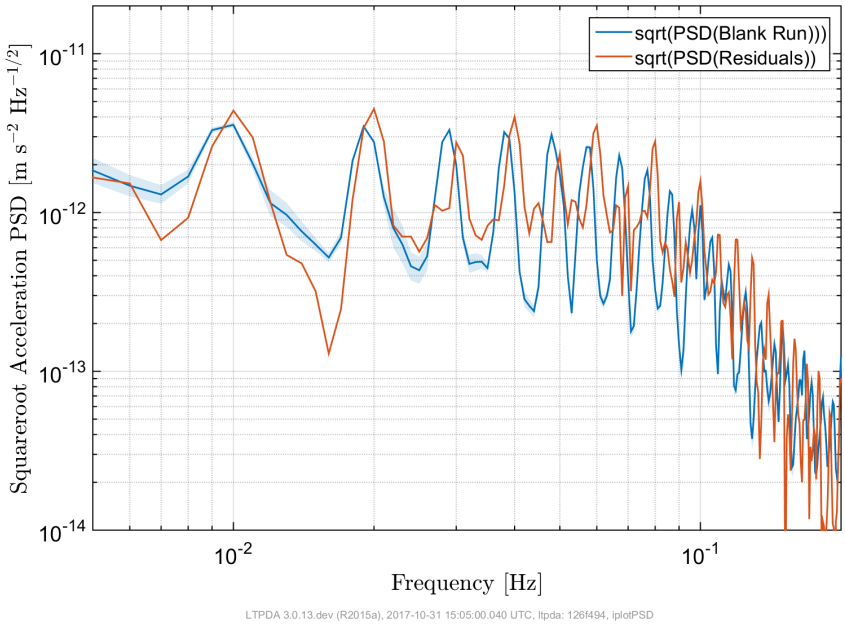

Figure 4.22: Power spectral densities of the blank run and injection signal data evaluated with the parameters that most reduce the difference between these two data sets in frequency space. The harmonics seen are likely a result of the glitches in the data with a period of around 100 s. This is within the frequency range of the MCMC fit (5-35 mHz) and influences the result.

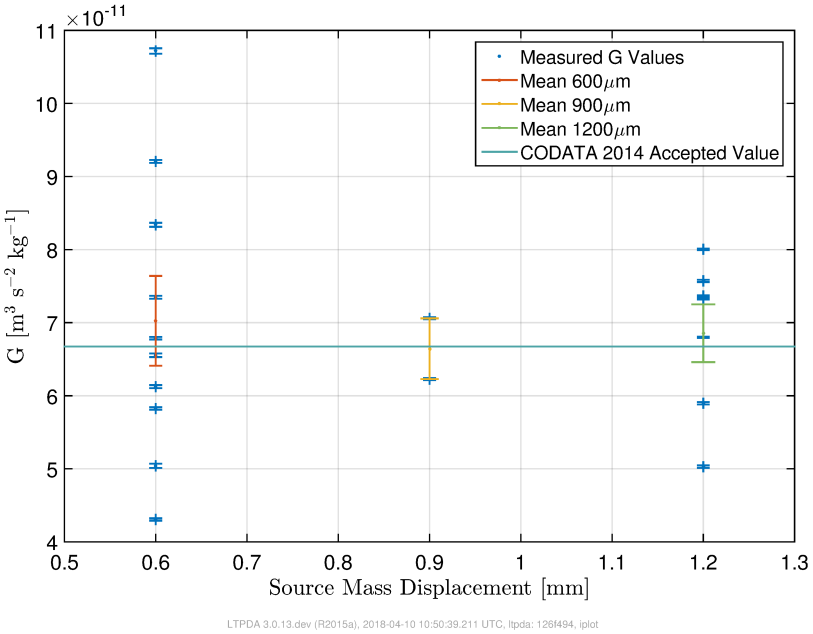

Figure 4.23: Results for G as a function of the source mass displacement. The mean value of G evaluated at each source mass amplitude is also shown, with errors dominated again by the scatter of points. The horizontal line indicates the CODATA 2014 value for comparison.

Figure 4.22 shows the PSDs of the blank run and the injection run residuals after subtracting the fit results for the gain. The peaks show the harmonics of the base signal at around 10 mHz and highlight that regular glitches enter into the fits at an early stage in the analysis. Furthermore, the glitches are not consistently the same shape, making them difficult to characterize and subtract from the data.

The dependency of the results on the source mass displacement and the length of the high resolution segments was investigated to test any remaining uncertainties not accounted for. Figure 4.23 shows the fit values of G versus the source mass displacement amplitude. No visible trend is observed, with the scatter at each amplitude being roughly in agreement with the other amplitudes. All three means are in agreement with each other, to within their uncertainty which is again dominated by the scatter of points. Each mean is also in agreement with the CODATA value, shown by the horizontal line.

Figure 4.24 shows the same plot but for the case of two $F_{Rad,z}$ estimates at the beginning and end of a solar sail. Each groups error bar is still dominated by the scatter of points, and has not significantly reduced from results using one estimate for $F_{Rad,z}$. All three points are still

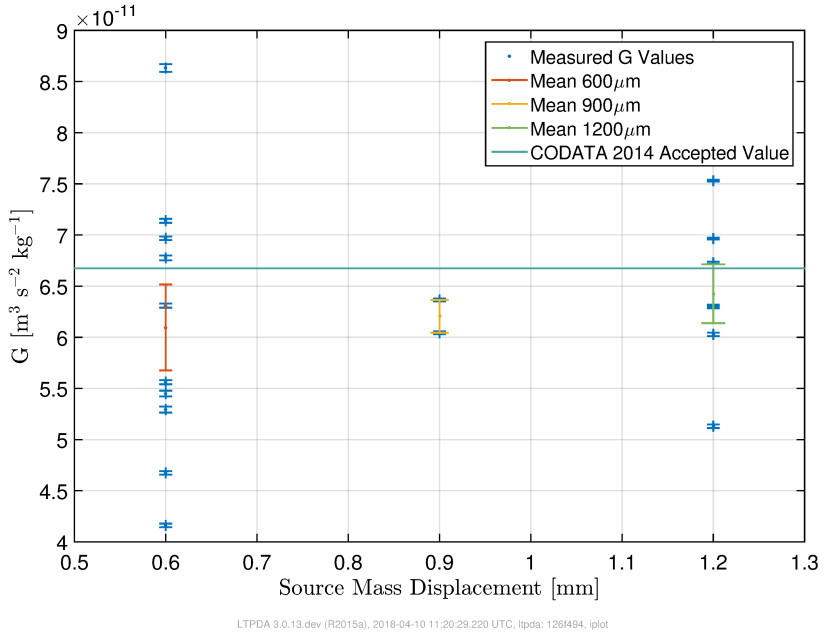

Figure 4.24: G as a function of the source mass displacement amplitude after adjusting for earlier and later SRP forces in a solar sail. All three averages are consistent with each other but two differ from the CODATA value by around 1σ.

in agreement with each other, although two are now more than 1σ from the CODATA value. This suggests that this correction only accounts for part of the errors, and again that the mean SRP force must also vary between solar sails.

Figure 4.25 shows G versus the duration of the high resolution segments used in the fits. Again there does not seem to be any clear correlation, indicating that the length of data used for the fits does not significantly alter the fit results.

Figure 4.26 shows the fractional errors from each fit for G as a function of the duration of high resolution segment multiplied by the amplitude of the source mass displacement. This combination of variables is expected to show some correlation with the fractional errors on G; longer durations average over random effects and transients, while larger source mass displacements give larger signals which the fits should be more sensitive to. Although the scatter is still large, there is a slight inverse trend in the data. Given that the trend is weak, it can be said that the scatter of points far outweighs the statistical uncertainties in the measurements, and if the scatter can be accounted for then the resulting error on the final reported value could be reduced to around a percent.

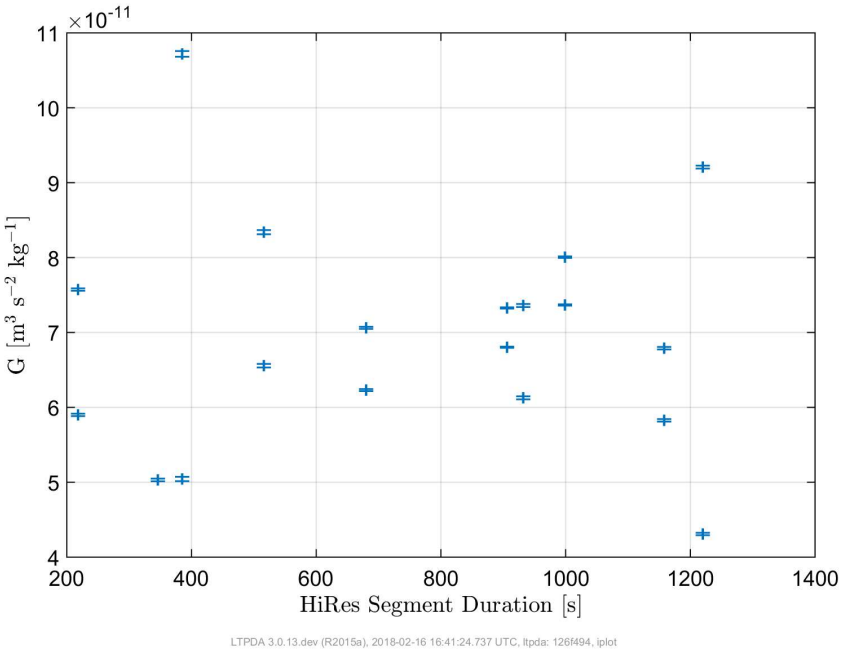

Figure 4.25: G measurements plotted as a function of length of high resolution data segment used in the signal fits. No obvious trend is visible, indicating the fit results do not depend strongly on the length of data used. Note that the lengths tested are always longer than the time between glitches.

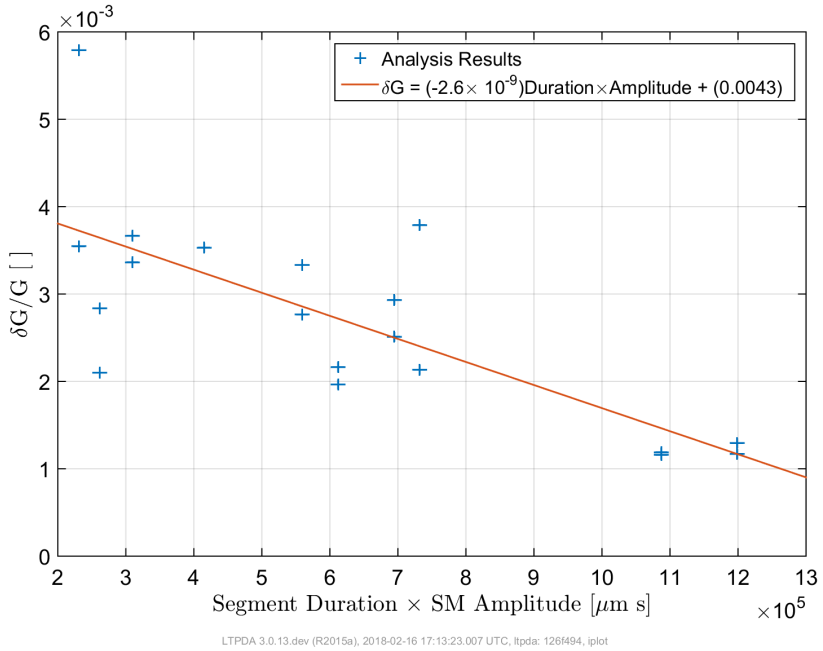

Figure 4.26: Fit errors on G as a function of the length of data used within each high resolution segment multiplied by the source mass displacement. This should show some negative correlation as the fits should be more sensitive to longer segments of data and larger displacements of the source mass. A slight negative correlation can be seen.

Future work on this project includes a cleaning method to remove glitches from the data. This would run a Matlab script to identify glitches in the high resolution segments, and then a python script to fit a sine-Gaussian model to each impulse. Such codes exist for nominal Δg_x noise runs, but need to be tuned for this data as the background noise is not as stable and the origins of the glitches have not yet been identified. For more information about glitch removing methods, see supplemental material in the February 2018 Pathfinder results article [14].

If this experiment were to be repeated in the future, care needs to be taken to find a way to better account for the SRP force. Alternatively, an additional mass outside of the interferometry system could be used to source the signal. This would negate the need to perform a solar sail as the drag free system could then be used, decoupling the noise of the thrusters from the sensitive axis. Furthermore, the centrifugal force would be greatly reduced, and the calibration parameters (e.g. gains and stiffnesses) could be taken from nominal mission calibration experiments.

Once the final results of this experiment are released, it is hoped that they will encourage the addition of space based gravity gradiometers as a method to measure this constant. Just as Cavendish inherited his apparatus, it is hoped that future designs for measurements of G in space will inherit the lessons learned here and one day populate future versions of the CODATA plot.

Chapter 5

Tests of Fundamental Physics with LISA Pathfinder

5.1 Introduction

Since its conception in the earlier part of the last century, general relativity (GR) has had success in predicting various phenomena [130]. Most notably, the Hulse-Taylor binary pulsar orbital decay [114], the Perihelion procession of Mercury [41], the lensing of light around heavy objects [47], the procession of gyroscopic orbits due to frame dragging [52] and most recently, the equivalence principle of free-fall acceleration [117]. Each of these effects have been measured and agree with GR predictions.

However, there are still observed conflicts with GR. Still unexplained are rotation curves of galaxies [105] which require a darker form of matter to be compatible with GR, hidden from measurement by decoupling from light and located throughout the galaxy. Furthermore, the measurement of cosmic acceleration at an increasing rate [104] saw the confirmation of a cosmological constant in the Einstein field equations, corresponding to a dark energy permeating the Universe.

One of the biggest problems that faces modern physics is the reconciliation of all four funda-

mental forces in a grand unified theory. Although advancements have been made to join the Weak and Electromagnetic forces [62] [107] [129], followed about a decade later by the strong force [44], gravitation still lacks a full theoretical description that unifies it with the other three forces at very high energies. Known as the 'hierarchy problem', quantum field theory predicts corrections to the Higgs particle mass that place it many orders of magnitude higher than observed. Theorists have tried to reconcile this using a wide variety of modifications to both gravity and quantum field theory.

These problems have led modern theoretical physics to explore methods of introducing a cosmological constant and dark matter, or perturbing GR in order to explain the differences in a new theory of gravitation. Searches for new physics have probed the parameter spaces for many of these theories and with the advent of gravitational wave astronomy, new ways to place exclusion limits are anticipated [18].

As the sensitivity of precision physics experiments improve, the low energy limits of these theories also come into reach, many of which include signatures unique to their mechanics. In this chapter, the role that Pathfinder, and more broadly any highly sensitive gravity gradiometer, can play in this discussion is explored.

5.2 Newtonian Gravity as a Limit of General Relativity

In order to see how the low energy limit of gravity can be probed, it is important to understand how various theories of gravity can imprint on this limit. In this section, the reduction of GR to the Newtonian limit is shown, and then a qualitative example of how the result can be changed when perturbing GR is provided. More detail on the derivation and other aspects of geometry as applied to GR can be found in the lecture notes by S. Carroll [36].

The first step to recovering Newtonian dynamics in the weak field limit is to show that the geodesic of a particle not subject to any forces in a curved space-time is equivalent to an accelerating particle subject to a gravitational force in flat space-time. To do this for GR, the metric, $g_{\mu\nu}$, is taken as the Minkowski metric representing a flat space-time, $\eta_{\mu\nu} = \mathrm{diag}(-1, +1, +1, +1)$,

plus a small perturbation $h_{\mu\nu} = 2/c^2 \text{diag}(-\Phi, -\Psi, -\Psi, -\Psi)$

$$
\begin{aligned}
g_{\mu\nu} &= \eta_{\mu\nu} + h_{\mu\nu} \\
g_{\mu\nu} &\approx \begin{bmatrix} -1 & 0 & 0 & 0 \\ 0 & 1 & 0 & 0 \\ 0 & 0 & 1 & 0 \\ 0 & 0 & 0 & 1 \end{bmatrix} - \begin{bmatrix} 2\Phi/c^2 & 0 & 0 & 0 \\ 0 & 2\Psi/c^2 & 0 & 0 \\ 0 & 0 & 2\Psi/c^2 & 0 \\ 0 & 0 & 0 & 2\Psi/c^2 \end{bmatrix}
\end{aligned} \tag{5.1}
$$

The scalar potential fields Φ and Ψ, with units $m^2 s^{-2}$, are the simplest choice in perturbation that still preserve the cosmological principle which states there is no preferred place or direction in the universe. It can be also assumed that Φ and Ψ are independent of time as the Newtonian limit assumes a non-accelerating system, and velocities can be boosted into the reference frame.

The proper time τ is defined to be the local time measured by a massive particle, i.e. non-zero mass, as it moves in a time-like fashion along its world-line, and so τ may be used to parameterize that motion. Also defining $g^{\mu\nu}$ as the dual (or contravariant) metric, such that $g^{\mu\rho} g_{\rho\nu}$ results in the identity matrix $I^\mu_\nu = \text{diag}(1, 1, 1, 1)$, consider the geodesic equation governing the trajectory due to a force F^μ on the particle

$$
F^\mu = m \left(\frac{d^2 x^\mu}{d\tau^2} + \Gamma^\mu_{\rho\sigma} \frac{dx^\rho}{d\tau} \frac{dx^\sigma}{d\tau} \right) \tag{5.2}
$$

where

$$
\begin{aligned}
\Gamma^\mu_{\rho\sigma} &= \frac{1}{2} g^{\mu\lambda} \left(\partial_\sigma g_{\lambda\rho} + \partial_\rho g_{\sigma\lambda} - \partial_\lambda g_{\rho\sigma} \right) \\
&\approx \frac{1}{2} \eta^{\mu\lambda} \left(\partial_\sigma h_{\lambda\rho} + \partial_\rho h_{\sigma\lambda} - \partial_\lambda h_{\rho\sigma} \right)
\end{aligned} \tag{5.3}
$$

Using the diagonal form of the metric the only non-zero components for $\Gamma^\mu_{\rho\sigma}$ are for the special cases when $\rho = \sigma$. Denoting spatial indices with roman lower case letters and the time index

with 0, the non-zero connection coefficients can be written as

$$\Gamma^0_{00} = -\frac{1}{c^2}\partial_0\Phi \approx 0 \qquad \Gamma^i_{00} = \frac{1}{c^2}\partial_i\Phi$$
$$\Gamma^i_{jj} = \frac{1}{2}\left(2\partial_j h_{ij} - \partial_i h_{jj}\right) = \pm\frac{1}{c^2}\partial_i\Psi \qquad \Gamma^0_{ii} = -\frac{1}{c^2}\partial_0\Psi \approx 0 \tag{5.4}$$

where Γ^i_{jj} is negative if $i = j$ and positive if $i \neq j$. Taking $F^\mu = 0$ in equation 5.2 for no external forces on the particle in the curved space-time, the time coordinate equation of motion can be found as

$$\frac{d^2x^0}{d\tau^2} - \frac{1}{c^2}\partial_0\Phi\left(\frac{dx^0}{d\tau}\right)^2 - \frac{1}{c^2}\partial_0\Psi\left(\frac{dx^i}{d\tau}\right)^2 = 0 \tag{5.5}$$

Then applying the assumption that the gravitational perturbation is static, $\frac{d^2x^0}{d\tau^2} = 0$; and so the coordinate time t ($\equiv x^0$) is seen to be proportional to the proper time, namely $x^0 \propto \tau$.

Next, consider the spatial coordinate geodesic equation

$$\frac{d^2x^i}{d\tau^2} + \frac{1}{c^2}\partial_i\Phi\left(\frac{dx^0}{d\tau}\right)^2 - \frac{1}{c^2}\partial_i\Psi\left(\frac{dx^i}{d\tau}\right)^2 + \frac{1}{c^2}\partial_i\Psi\left(\frac{dx^j}{d\tau}\right)^2 + \frac{1}{c^2}\partial_i\Psi\left(\frac{dx^k}{d\tau}\right)^2 = 0 \tag{5.6}$$

Which can be multiplied twice by $d\tau/dt$ to convert to derivatives with respect to time t using the chain rule. Note that the derivatives of Ψ are multiplied by the components of the three velocity $v^{i,j,k} = dx^{i,j,k}/d\tau$, which are assumed small in the Newtonian limit. Neglecting these terms, the equation can be further reduced to

$$\frac{d^2x^i}{dt^2} = -\frac{1}{c^2}\partial_i\Phi \tag{5.7}$$

which is a statement of Newtons first law that the acceleration of a particle is proportional to the force it experiences. It is clear here that the scalar parameter Φ is interpreted as the gravitational potential due to a massive body near the particle.

The next step of the reduction is to show the explicit form of the force as the inverse-square law. To do this, consider the Einstein field equations

$$G_{\mu\nu} = R_{\mu\nu} - \frac{1}{2}Rg_{\mu\nu} = \frac{8\pi G}{c^4}T_{\mu\nu} \tag{5.8}$$

Where in this case the stress-energy (or energy-momentum) tensor $T_{\mu\nu}$ is defined to be

$$T_{\mu\nu} = \begin{bmatrix} \rho c^2 & 0 & 0 & 0 \\ 0 & 0 & 0 & 0 \\ 0 & 0 & 0 & 0 \\ 0 & 0 & 0 & 0 \end{bmatrix} \tag{5.9}$$

in the low energy limit where the only important component is the matter density ρ as the system is assumed pressure-less with no shear.

The Ricci scalar R is the contraction of the Ricci tensor $R_{\mu\nu}$, where $R = g^{\mu\lambda}R_{\lambda\mu} = R^{\mu}_{\mu}$ and $g^{\mu\nu}$ is the dual metric. The Ricci tensor $R_{\mu\nu}$ is itself a contraction on (here) the first and third indices of the Riemann curvature tensor $R^{\rho}_{\mu\beta\nu}$. $R^{\rho}_{\mu\beta\nu}$ holds a complete description of the curvature of the space under consideration, and it is defined as a function of the connection coefficients (or Christoffel symbols of the second kind), $\Gamma^{\alpha}_{\sigma\rho}$, and their derivatives. The connection coefficients are functions of the dual metric and the derivatives of the metric $g_{\mu\nu}$ for that space.

The Riemann tensor can be written

$$R^{\rho}_{\mu\beta\nu} = \partial_{\beta}\Gamma^{\rho}_{\mu\nu} - \partial_{\nu}\Gamma^{\rho}_{\mu\beta} + \Gamma^{\rho}_{\beta\lambda}\Gamma^{\lambda}_{\mu\nu} - \Gamma^{\rho}_{\nu\lambda}\Gamma^{\lambda}_{\mu\beta} \tag{5.10}$$

and so, after contracting the first and third indices, this becomes

$$R^{\rho}_{\mu\rho\nu} \equiv R_{\mu\nu} = \partial_{\rho}\Gamma^{\rho}_{\mu\nu} - \partial_{\nu}\Gamma^{\rho}_{\mu\rho} + \Gamma^{\rho}_{\rho\lambda}\Gamma^{\lambda}_{\mu\nu} - \Gamma^{\rho}_{\nu\lambda}\Gamma^{\lambda}_{\mu\rho} \tag{5.11}$$

From the symmetry of the connection coefficients ($\Gamma^{\rho}_{\mu\nu} \equiv \Gamma^{\rho}_{\nu\mu}$), the Ricci tensor then can be written

$$R_{\mu\nu} = \partial_{\rho}\Gamma^{\rho}_{\nu\mu} - \partial_{\nu}\Gamma^{\rho}_{\rho\mu} + \Gamma^{\rho}_{\rho\lambda}\Gamma^{\lambda}_{\nu\mu} - \Gamma^{\rho}_{\nu\lambda}\Gamma^{\lambda}_{\rho\mu} \tag{5.12}$$

Terms where the lower indices of the connection coefficients are equal are taken only, and the potentials Φ and Ψ are treated as constant relative to typical orbital times for the particle. Then, since only small perturbations to the metric are being considered, a useful approximation can be

made by keeping only terms which are first order in the potentials, i.e. the metric perturbations. This reduces the components of the Ricci tensor to become

$$\begin{aligned} R_{00} &= \partial_i \Gamma^i_{00} + \Gamma^i_{ii}\Gamma^i_{00} = \frac{1}{c^2}\delta^{jk}\partial_j\partial_k\Phi + \frac{3}{c^2}\partial_0\partial_0\Psi \approx \frac{1}{c^2}\delta^{jk}\partial_j\partial_k\Phi \\ R_{0i} &= R_{i0} = \frac{2}{c^2}\partial_0\partial_i\Psi \approx 0 \\ R_{ij} &= \frac{1}{c^2}\partial_j\partial_i\left(\Psi - \Phi\right) = 0 \text{ (for } \Phi = \Psi \text{ in GR)} \\ R_{ii} &= \frac{1}{c^2}\delta^{jk}\partial_j\partial_k\Psi \end{aligned} \tag{5.13}$$

Summing over the diagonal components of the Ricci tensor yields the Ricci scalar as

$$R = -R^0_0 + R^i_i = -\frac{1}{c^2}\delta^{jk}\partial_j\partial_k\Phi + \frac{3}{c^2}\delta^{jk}\partial_j\partial_k\Psi = \frac{2}{c^2}\delta^{jk}\partial_j\partial_k\Phi \text{ (for } \Phi = \Psi \text{ in GR)} \tag{5.14}$$

Inserting into the '00' component of the Einstein field equations becomes

$$\begin{aligned} R_{00} - \frac{1}{2}\eta_{00}R &= \frac{8\pi G}{c^4}T_{00} \\ \frac{1}{c^2}\delta^{jk}\partial_j\partial_k\Phi - \frac{1}{2}(-1)\frac{2}{c^2}\delta^{jk}\partial_j\partial_k\Phi = \frac{1}{c^2}2\delta^{jk}\partial_j\partial_k\Phi &= \frac{8\pi G}{c^4}\rho c^2 \\ \therefore \frac{1}{c^2}2\delta^{jk}\partial_j\partial_k\Phi &= \frac{8\pi G}{c^2}\rho \end{aligned} \tag{5.15}$$

or $\nabla^2\Phi = 4\pi G\rho$, which is Poisson's equation for a gravitational potential Φ. Note that the assumption $\Psi = \Phi$ has been implemented as GR predicts that the two potentials are indistinguishable. Poisson's equation for the gravitational potential may be solved for a point mass M located at a source position $\vec{r}_M^{\,'}$ using a Green's function $\mathcal{G}(\vec{r} - \vec{r}_M^{\,'})$, where an arrow indicates only the spatial indices are being considered, that satisfies

$$\nabla^2\mathcal{G}(\vec{r} - \vec{r}_M^{\,'}) = \delta(\vec{r} - \vec{r}_M^{\,'}) \tag{5.16}$$

where $\delta(\vec{r} - \vec{r}_M^{\,'})$ is the Dirac delta-function. Using the property that $\nabla^2\left(\frac{1}{|\vec{r}-\vec{r}_M^{\,'}|}\right) = -4\pi\delta(\vec{r} - \vec{r}_M^{\,'})$, the Green's function can be written as $\mathcal{G}(\vec{r} - \vec{r}_M^{\,'}) = \frac{-1}{4\pi|\vec{r}-\vec{r}_M^{\,'}|}$.

A solution using a Green's function, which in this case gives the potential due to a single point mass at a single position, can then be used to solve for the gravitational potential by summing over all infinitesimal contributions to the total mass distribution giving rise to the potential Φ. In other words

$$\begin{aligned}\Phi\left(\vec{r}\right) &= \int_{V_{source}} \mathcal{G}(\vec{r}-\vec{r}\,')4\pi G\rho(\vec{r}\,')\; d^3\vec{r}\,' \\ &= -4\pi G \int_{V_{source}} \frac{\rho(\vec{r}\,')}{4\pi \mid \vec{r}-\vec{r}\,' \mid} d^3\vec{r}\,' = -\frac{GM}{\mid \vec{r}-\vec{r}\,'_M \mid}\end{aligned} \tag{5.17}$$

where the field point $\vec{r}$ and the positions $\vec{r}\,'$ of the volume $d^3\vec{r}\,'$ within the source with volume V_{source} are measured from the same origin, G is Newtonian constant of gravity, and $\int_{V_{source}} \rho(\vec{r}\,')d^3\vec{r}\,' = M$. Note that the point-like nature of the source picks out $\vec{r}\,' = \vec{r}\,'_M$ in the integrand.

For a point-mass M located at the origin of the coordinate system $(\vec{r}\,' - \vec{0})$, Poisson's equation yields $\Phi(r) = -\frac{GM}{r}$. The equipotentials for Φ are therefore concentric spherical shells about the point-mass, and since the Newtonian gravitational acceleration $\vec{a} = -\vec{\nabla}\Phi = -\partial_r(-GM/r)\vec{e}_r$, or $\vec{a} = -(GM/r^2)\vec{e}_r$, where $\vec{e}_r$ is a unit vector in the outward radial direction. This is the familiar inverse-square law of Newtonian gravitational attraction for a particle placed a distance r away from a point-mass M. Note that the limit is a result of the first order estimate for the full result. As such, any modifications to GR that have first order corrections to the connection coefficients would have signatures on the Newtonian limit.

Originally, the formulation of GR used the inversion of this reduction. It started at the inverse square law and worked up from the conservation of energy and momentum, which shows that the Einstein field equations are the simplest form possible for GR that still preserves conservation laws. To see the conservation, consider the covariant derivative of a second rank tensor field $A_{\mu\nu}$ defined as

$$\nabla_\sigma A_{\mu\nu} = \partial_\sigma A_{\mu\nu} - \Gamma^\lambda_{\sigma\mu} A_{\lambda\nu} - \Gamma^\lambda_{\sigma\nu} A_{\mu\lambda} \tag{5.18}$$

which says the derivative in an arbitrary space-time is the normal derivative through the coordinate system, plus a correction to account for changes in the coordinate system due to matter

curving the space-time.

Conservation of energy and momentum can be written as

$$\nabla^{\mu} T_{\mu\nu} = g^{\rho\mu} \nabla_{\rho} T_{\mu\nu} = 0 \tag{5.19}$$

which follows from the simple definition of the energy momentum tensor. The ∇^{μ} used here is still a covariant derivative operator, but its index has been raised in order to ensure metric compatibility. Linking this to the curvature terms of the Einstein field equations

$$\nabla^{\mu} \left(R_{\mu\nu} - \frac{1}{2} R g_{\mu\nu} \right) = 0 \tag{5.20}$$

Only taking terms first order in Γ, which follows from the assumption that the perturbations to the metric are small, the conservation equations become

$$\nabla^{\mu} \left(\partial_{\rho} \Gamma^{\rho}_{\nu\mu} - \partial_{\nu} \Gamma^{\rho}_{\rho\mu} - \frac{1}{2} g_{\mu\nu} g^{\sigma\lambda} \left(\partial_{\rho} \Gamma^{\rho}_{\sigma\lambda} - \partial_{\sigma} \Gamma^{\rho}_{\rho\lambda} \right) \right) = 0 \tag{5.21}$$

where the Ricci scalar has been written as the contraction of indices in the Ricci tensor to first order in the connection coefficients. Then expanding the covariant derivative as only the partial derivative as other terms are second order in the coefficients, the equation becomes

$$\partial^{\mu} \partial_{\rho} \Gamma^{\rho}_{\nu\mu} - \partial^{\mu} \partial_{\nu} \Gamma^{\rho}_{\rho\mu} - \frac{1}{2} g^{\sigma\lambda} \partial_{\nu} \partial_{\rho} \Gamma^{\rho}_{\sigma\lambda} + \partial_{\nu} \partial^{\lambda} \Gamma^{\rho}_{\rho\lambda} = 0 \tag{5.22}$$

The second and last terms are equivalent after relabelling the indices being summed over. The first and third terms are also equivalent, once the symmetry of the connection coefficients are employed so that the only non-zero contribution is when $\mu = \nu$ and when $\sigma = \lambda$. The difference is that the first term picks out specifically when $\mu = \nu$, but the third term sums over the gamma matrices. This gives twice as many entries as the first term after considering the entries in the perturbation to the metric are all the same. Hence energy and momentum conservation follows from the Einstein field equations in the weak field limit.

A property of the metric is that it is locally coordinate invariant, and therefore it can be written as the canonical form with vanishing first derivatives. From this, it can be said that the Lagrange density of general relativity must be some scalar, composed of second derivatives of the metric, multiplied by $\sqrt{-g}$, where $g = \det(g_{\mu\nu})$. The simplest choice in scalar using second derivatives of the metric is the Ricci scalar R. This leads to the Hilbert action in four dimensional space-time

$$S_H = \int d^4x\sqrt{-g}R \tag{5.23}$$

which, when used in the Euler-Lagrange equation to find the motion of a particle perturbed from a stable state, gives the Einstein field equations in a vacuum. When a component of the Lagrange density that couples to matter is included, it is possible to uniquely identify

$$T_{\mu\nu} = \frac{1}{\sqrt{-g}}\frac{\delta S_M}{\delta g^{\mu\nu}} \tag{5.24}$$

where S_M is an extra component of the action relating to the coupling of gravity with matter. It should be noted that the conservation of energy and momentum follow from Noether's theorem by claiming invariance under translation in time and space respectively.

The important message here is that Einstein's equations are the simplest choice for the Lagrange density. This suggests that it is theoretically permissible to choose a different density, so long as the conservation equations still hold and the same weak field limit is reached at laboratory scales. According to this derivation, there are three ways to modify this density: include higher order terms in R, include a small dynamical field, or change the metric.

Adding a dynamical field gives rise to an extra force and the resulting set of actions describe 'fifth force' theories. These are showing some promise and are motivated particularly in string theory, but require a way to hide the new particle from observation. This can be done in many ways, for example by a screening mechanism relative to a characteristic length (Yukawa), acceleration scale (modified Newtonian dynamics), or local matter density (Chameleons). Modifying the metric constitutes a change in the particle that mediates gravity, or adding more particles that couple to gravity. For example bi-gravity splits the metric into two describing a massive and

massless graviton, effectively adding a tensor field to the theory. There are many more ways to modify the action, however outlining them is beyond the scope of this thesis.

Instead, the specific example of a scalar field ϕ perturbation is outlined to show how modifications can be achieved using screening mechanisms. The Hilbert action including a new scalar field becomes

$$S_H = \int d^4x\sqrt{-g}\left(f(\phi)R + \frac{1}{2}g^{\mu\nu}(\partial_\mu\phi)(\partial_\nu\phi) - V(\phi)\right) \tag{5.25}$$

where $V(\phi)$ is a function describing the self interactions of the field and its mass. The function f defines the coupling of the field with the universe, and includes a dynamic gravitational 'constant' G. Note that the component S_m describing the coupling of the theory with matter will also transform. One example takes $S_m = S_m(A^2(\phi)g_{\mu\nu}, \psi_i)$, where ψ_i describe species of matter and $A^2(\phi)g_{\mu\nu}$ is a conformal transformation of the metric $g_{\mu\nu}$, and includes a shielding mechanism to maintain the integrity of laboratory experiments and astronomical observations to date [32].

When the full action $S = S_H/8\pi G + S_M$ is used to derive the equations of motion under coordinate transformation invariance, a modification to the coupling constant G is found. It was mentioned in chapter 4 that it is useful to think of departures from Newtonian theory as a re-scaling of the gravitational constant. Indeed, for the specific example of scalar-tensor gravity G is found to be inversely proportional to the scalar field $G \sim 1/\phi$ [31].

The background material here highlights that the weak field limit can also be used to explore the rich zoo of theories used to explain the remaining conflicts between observations and GR. In the context of Pathfinder, original motivation for testing modified gravity lay in the ultra-low acceleration dynamics. This developed into a measurement of Newton's constant (see chapter 4), which poses the question of how well can gravity gradiometers probe these theories and what can be expected from an experiment that can use fully drag free dynamics? This chapter outlines the development of these ideas.

5.3 Developing Ideas for a Saddle Point Mission

5.3.1 Background

It has been argued that a modification to Newtonian dynamics according to the acceleration regime of the object could give an alternative explanation for the incompatibility between theoretical and measured rotation curves [92] [93]. By incorporating a cut off acceleration in the theory, Newtonian dynamics is recovered in the systems tested at higher accelerations, such as the Hulse-Taylor binary Pulsar system, but a new set of laws is uncovered in the low acceleration limit. The cut off acceleration is usually taken to be around $10^{-10}\,\mathrm{ms}^{-2}$. Theories that segregate the laws of Physics into acceleration limits are usually denoted by MOdified Newtonian Dynamics, or MOND for short.

There are many different flavours of MOND, using various transfer functions that transform Newton's laws into the modified dynamics at varying rates as the acceleration decreases. The most notable ones in the context of Pathfinder are the linear, quadratic and Tensor-Vector-Scalar (TeVeS) theories. These entered a conversation that discussed the ability for Pathfinder to constrain alternative or extension theories of gravity [53] [111] [119] [120]. In particular, for a time there was mention of a mission extension to examine the MONDian parameter space by passing the space craft through the saddle point in the gravitational potential between the Earth and the Sun [54] [119] [120].

The Newtonian Or Modified Acceleration Dynamics (NOMAD) mission suggested sending Pathfinder through the gravitational saddle point between the Earth and Sun, where it had been argued the MOND limit is within sight of the estimated experimental limits at the time [20]. In the development of the idea, there was some disagreement in how far and to what extent Pathfinder could constrain MOND parameter space, which was the specific target for this extension mission. In all cases, it could be agreed that, even in the 'current best estimate' cases for the sensitivity curves at the time, and even for the new reported curves, the extent to which the signal entered into the observable regime was limited, and usually involved very specific transfer functions.

When the proposal was taken to the Science Working Team in a meeting in 2015 it was received with mixed reviews, especially as there had been new constraints on TeVeS theories from timing of a new Pulsar system [57]. It was clear that in order to garner support for a test of fundamental physics using LISA Pathfinder, there would have to be a departure from the MOND specific analyses. The work outlined here is a close copy to the conference proceedings from the fourteenth Marcel Grossmann meeting in July 2015 [19].

5.3.2 Original Motivation for an Experiment to Constrain MOND

The NOMAD proposal looked to demonstrate that Pathfinder could fill a gap in our understanding of how the laws of physics work at various acceleration scales. To do this, it devised a parameter space that quantified the difference between the models for a variety of systems and the measured accelerations. The difference between the theory prediction for acceleration given Newtonian dynamics and the measured acceleration of the system is taken is divided by the measured acceleration to form a fraction residual error. This is plotted against the measured acceleration of the system to form Figure 5.1, which is the plot used in the original proposal [109].

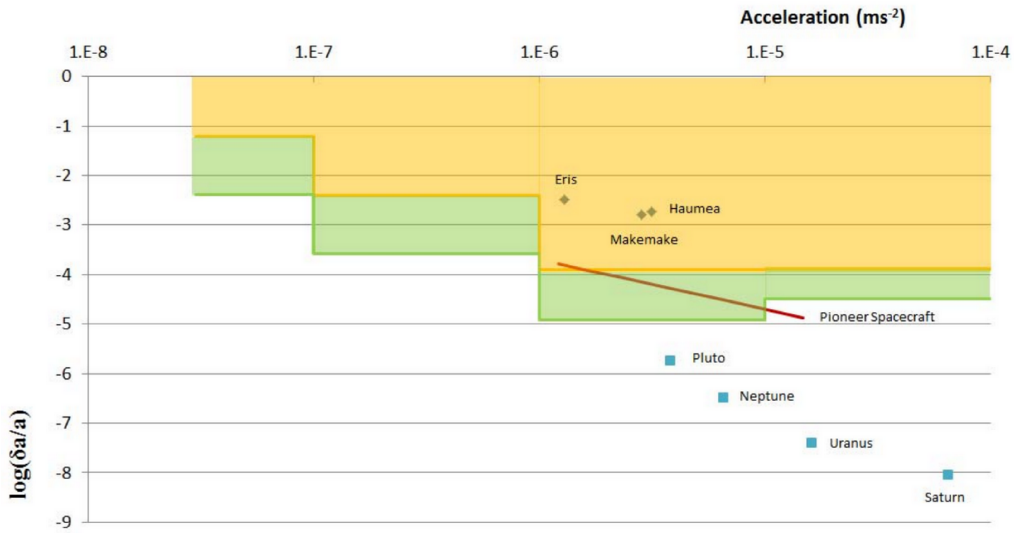

Figure 5.1: Original plot developed for the proposal of an extension mission to investigate the effects of Modified Newtonian Dynamics at the saddle point between the Earth and Sun. The potential constraints from Pathfinder are shown in yellow (for the nominal sensitivity requirements) and green (for the 'current best estimate' of sensitivity as of 2013). [109]

The variable $\delta a/a$ (the fractional residual error, also called $\zeta(a)$ in later calculations) has the additional property that it is equivalent to the fractional residual error in the gravitational potential, assuming a Newtonian model. This first attempts to look at current coverage of this parameter space were calculated by Sumner & Trenkel [109]. This included planetary points, derived from the Ephemerides of the planets and compared with observational data [99] [100], Pioneer measurements of the gravitational acceleration on exiting the solar system [121], and potential contributions from a Pathfinder measurement based on the best estimate and the nominal sensitivity curves for the system at the time of the proposal.

The work here details the additional constraints added to the plot first constructed by Sumner & Trenkel. These investigations included points from pulsar timing, Globular Cluster data, the centre of mass proper motion of the Large Magellanic Cloud and the Sun's orbital motion around the Galactic Centre.

5.3.3 Sources for Constraints on Newtonian Dynamics

One set of points for the plot uses precision pulsar timing data. Catalogues such as that available from the Australia Telescope National Facility (ATNF) [89] and a compilation of data provided by William Johnstone [78], can give the typical separations of objects and a very precise measure of orbit periods P_{data} using Doppler shifts of pulse times. These can be used to calculate the centrifugal acceleration of the object to estimate the 'observed' acceleration assuming a circular orbit (eccentricities $\leq 10^{-4}$ were used). This is, along with the comparative 'model' acceleration, given by

$$|\vec{a}_{data}| = M_{tot} r \frac{4\pi^2}{P_{data}^2} \qquad |\vec{a}_{model}| = \frac{GM_{tot}}{r^2} \tag{5.26}$$

with their difference used in the fractional residual error $\delta a/a$. Masses used in this analysis were estimated using the upper limit for neutron star formation $M \approx 1.35 M_{\odot}$. This is rooted in the theory behind neutron star formation in a binary system, where the mass limit before collapse is reached by mass transfer. The companion mass is estimated using its spectral type.

A second set of points uses Globular Cluster (GC) observations, compiled by William E. Harris [68], where the role of Newton's laws in the Virial Theorem can be tested for relaxed systems. GCs are known to be relaxed systems as their ages are typically an order of magnitude greater than the relaxation time [24]. To do this, the velocity dispersions for a sample of observed GCs are used with their typical core radii to find the averaged core kinetic energy for the system. This can be used to find the 'observed' gravitational potential energy of the GC core. Then the number of stars in the core of the GC can be computed using the core luminosity density (given as $L_\odot$ kpc^{-3}) divided by the Luminosity estimate for the average core star spectral type using the relations derived in Habets & Heintze [66]. Multiplying by an estimate for the average stellar mass based on average spectral type, an estimate for the total mass and therefore gravitational potential energy GM_{tot}/r_{core} can be found. Noting that the fractional error in the acceleration is equivalent to the fractional error in the potential, and using the potential divided again by r_{core} to obtain the model Gravitational acceleration, the resulting fractional error can be extracted.

A third set of points uses a 2011 simulation by Kenji Bekki [21], where the center of mass proper motion (CMPM) of stellar objects within the Large Magellanic Cloud (LMC) are simulated and compared to observational data from the *Hubble Space Telescope*. According to Bekki, the residual error of around 50 kms^{-1} between the simulated and observed CMPM was the result of neglecting the effects of random motion by assuming circular orbits within the LMC. The measured CMPM speed of 380 kms^{-1} is used with the distance to the Milky Way (MW) galactic centre to find the 'measured' acceleration, assuming as a rough estimate a circular motion acceleration $a = \frac{v^2}{r}$, where v is the velocity and r is the distance to the MW. Noting that the fractional error in the acceleration is twice the fractional error in the CMPM speed v, the observed acceleration and fractional error are

$$a = \frac{v_{PM}^2}{R_d} = \frac{(3.8 \times 10^5)^2}{4.5 \times 10^{19}} = 3.21 \times 10^{-9} ms^{-2} \quad \frac{\delta a}{a} = 2\frac{\delta v}{v} = 2\frac{5 \times 10^4}{3.8 \times 10^5} = 0.263 \tag{5.27}$$

A spread of points were created using several estimates of the MW total bound luminous mass. The lower bound was found by 'counting' the number of stars and assuming the mean mass

is one solar mass. The upper bound uses a total mass derived from the orbits of the outer most bound luminous objects of the MW, which therefore includes any unseen or 'dark' mass. Following the large difference in these results, a quick sub-investigation into the role of the MW mass in the LMC acceleration was made and the results shown in Figure 5.2.

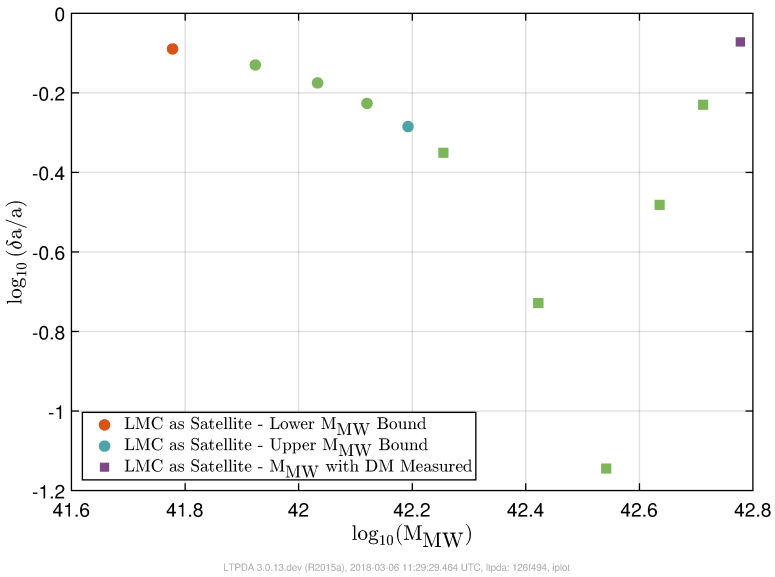

Figure 5.2: Dependence of the fractional residual error on the estimated Milky Way mass. Circles red - cyan increases in Luminous mass, Indigo square uses mass estimate extracted from orbits of most distant, bound objects, other square points fill in between.

The trough showing the MW mass that minimizes the residual is off from that derived using the outermost bound objects in the MW (indigo square) most likely due to assumptions about the LMC orbit. For example, it is assumed that the LMC is only affected by the MW potential and is isolated from interactions with other galaxies. Furthermore, it is assumed that its structure is point-like and not irregular or connected to the MW. These assumptions are oversimplifications [56] [74] [80], but nonetheless provide ball-park data points.

A fourth set of points uses a model outlined by Blum [28] and Vaucouleurs & Pence [45] for the mass distribution of the MW to find the error between the expected and observed galactic rotation curve. The model consists of a galactic bulge and bar, located in the centre of the rotating system, and an exponential disk, which is cited to agree with observational data of internal stellar dynamics. According to Blum, the combined bulge and bar mass is $1.8\times10^{10}M_{\odot}$. Then, using the characteristic radius $R_d = 5.98$ kpc derived by de Vaucouleurs & Pence, which is

consistent with MW disk stellar population luminosities and counts, the remaining parameters for the exponential disk model can be derived using the solar neighbourhood values for the luminous matter density.

The total mass enclosed in the exponential disk to a radius $R > R_{bulge+bar}$ is given by

$$M_{encl}\,(R) = -4\pi\rho_0 H R_d \left(R_d - e^{-R/R_d}\,(R + R_d)\right) \;+\; M_{bulge+bar} \tag{5.28}$$

Then, using the Sun's position ($R_{GC} = 8$ kpc) to estimate the central density, $\rho_0 \approx 3.81\rho_\odot \approx (0.46 - 1.26)$ stars pc^{-3}. Assuming a solar mass for the average stellar mass in the disk, $\rho_0 \approx (0.92 - 2.51 \times 10^{30})$ kg pc^{-3}. An upper limit treats the sun's off-plane position (~ 20 pc, using the lower estimate of disk thickness of ~ 200 pc) as the characteristic height H. A lower limit assumes the Sun is approximately in the galactic plane ($z = 0$, using the upper limit of the disk thickness of ~ 1000 pc).

It is now possible to construct the fractional residual error

$$\frac{\delta a}{a}\,(R) = \frac{G M_{encl}\,(R)}{v^2(R) R} - 1 \tag{5.29}$$

Using the flat rotation curves first observed by Rubin et al [105] to estimate the measured rotational velocities as a function of radius from galactic centre, a locus of constraints can be produced.

In order to further develop the exponential disk model for the MW, the Sun's velocity in the galactic plane was used to produce an upper and lower bound estimate for the locus of constraints. The measured total speed of the Sun with respect to the galactic centre is 220 kms^{-1}. However, the Sun is offset from the galactic plane by around 20 pc. This will split the speed into the rotational and vertical components, thus reducing the observed angular speed by a small amount. The split velocity will be used for the upper bound on the residual, while the larger, total speed observed will be used for the lower bound. The Sun's period around the GC is estimated to be $P_{\odot,\phi} = 240 \times 10^6$ yrs. This gives $v_\phi \approx 2\pi R_{GC}/P_{\odot,\phi} = 205.8$ kms^{-1}. Using the relation $v^2 = v_\phi^2 + v_z^2$, and an estimate for the form of v_z based on an un-

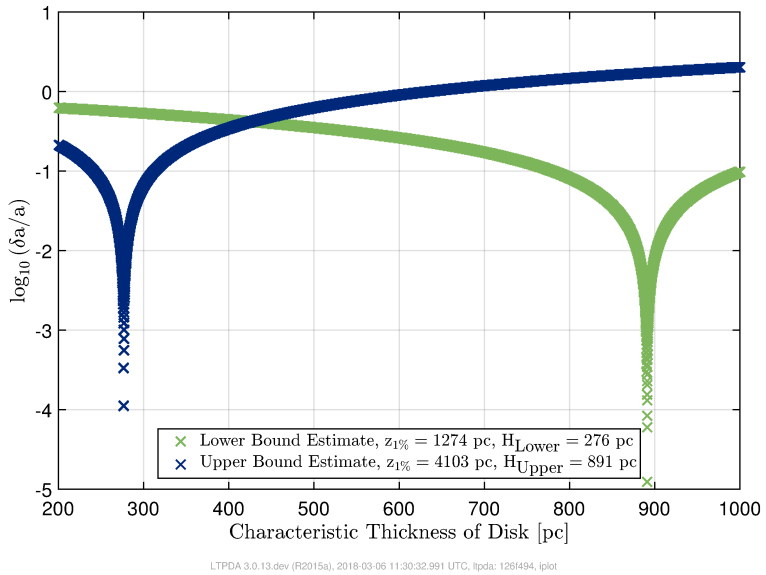

Figure 5.3: Investigation into the characteristic height scale for the exponential disk model of the Milky Way using the total measured velocity and a velocity split into angular and z oscillations of the Sun around the Galactic Center. The legend gives the height z at which the density becomes 1% of that at the central plane, using a scale height H extracted from the minima and shown in the legend.

damped oscillator in the z-direction with 2.7 oscillations per orbit around the galactic centre, $2\pi z_0/P_{\odot,z} \approx \sqrt{220^2 - v_\phi^2}$ which gives $z_0 = 77813 P_{\odot,z}/2\pi = 1124$ pc, where z_0 is the amplitude of the Suns oscillation around the galactic plane. This can be compared to the characteristic thicknesses of 300 pc (thin disk) and 1450 pc (thick disk) [61]. Combining the two velocity estimates with bounds for ρ_0, a range for $M_{encl}(R,H)$ and therefore $\zeta(R,H) = \delta a/a$ can be extracted: $8.9760 \times 10^{-4} H - 0.7998 \leq \zeta(R_{GC},H) \leq 2.7869 \times 10^{-3} H - 0.7711$, where H is in parsecs. Figure 5.3 shows $\log(\zeta(R_{GC},H))$ as a function of H, which can be used to extract optimal characteristic thicknesses H based on upper and lower limits on the enclosed mass of the MW. These are then inserted in equation 5.29 to find and upper and lower limit for the residual as a function of the radius in the range $R = 4$ kpc-16 kpc.

5.3.4 Updating the Plot with the New Constraints

Figure 5.4 shows the constraints extracted in the previous section with the points and bands from Figure 5.1. The yellow and cyan continuous bands illustrate the estimates for a Pathfinder-

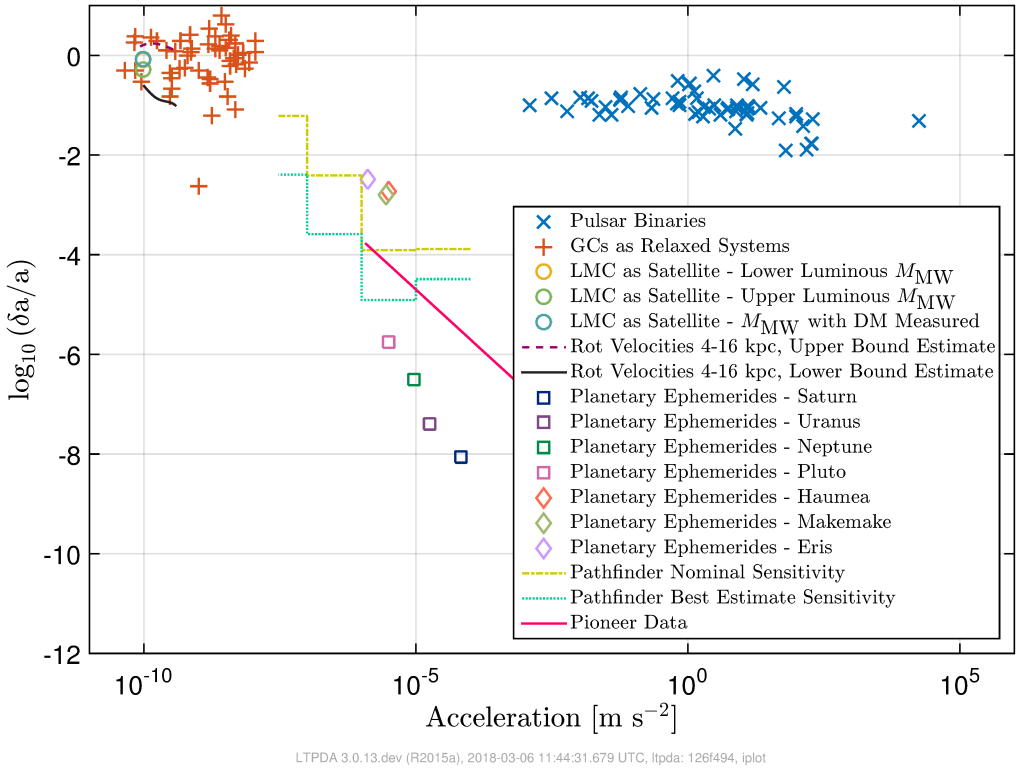

Figure 5.4: Current constraints from models/observed data in the low acceleration limit of GR. Previous points from Planetary Ephemerides, Pioneer measurements and LISA Pathfinder's potential contributions based on two estimates for the sensitivity curve. Added points from Pulsar Binaries, Globular Cluster data, and a simulation for the Centre of Mass Proper Motion for the Large Magellanic Cloud (LMC). MW mass given as a range depending on the definition of disk radius, and a last value to include estimate for luminous + DM mass.

like measurement based on the 'current best estimate' and 'nominal sensitivity' curves, and simulations of a fly-through trajectory [53], from the time of publication of the proposal. The scattered points give the GC and Binary Pulsar system analyses points, while the planetary points and Pioneer data give the most competitive points. The MW rotation curve gives two constraints, with the lower bound correlating with the need for dark matter in the MW structure. Finally, the LMC as a satellite gives a range of points due to the estimate for the total MW mass, again correlating with the need for dark matter.

The plot demonstrates that a Pathfinder measurement could help fill the space between the pulsar/solar system measurements and the galactic-scale measurements. It would bridge the gap between systems that are in good agreement with Newtonian dynamics, and other systems

that are known to diverge from these laws. However, it is noted that no known theories of gravity predict large anomalies in an intermediate acceleration range [71]. These results suggest that a saddle point fly-by mission would only test the agreement between Newtonian dynamics and measured systems in a region that is not known to contain new physics. That is to say that the cut-off acceleration for which the Newtonian dynamics convert into a modified regime is already placed around 10^{-10} ms^{-2} from observations of rotation curves of galaxies.

5.4 Theoretical Measurement of the Gravitational Constant in Drag Free

One of the consequences of the NOMAD mission proposal was a move to model independent probes of weak field violations to GR. As discussed in section 5.2, many theories of gravity include imprints on the gravitational constant, making it a sought after currency when probing gravity. In this section the motivation for attempting this measurement again but in drag free will be shown.

In order to demonstrate the difference when using a full drag free system, a simple modulation experiment is simulated on a LISA-like interferometer. It will be demonstrated that the results improve significantly when using the full sensitivity to measure a change in relative acceleration, rather than using electrostatic suspension forces to measure a change in acceleration.

Since the measurement is performed in drag free, the thrusters would not be turned off. This would mean the SRP force becomes irrelevant, and the space craft could be left in a nominal configuration. An example of the experiment is shown in Figure 5.5. However, as LISA is still in the planning stages, some of the parameters describing the signal are unknown. A scan through the parameter space governing the magnitude of the signal can be made, which also highlights the most significant parameters to optimize when exploring layouts for future gradiometers.

The angle between sensitive axes of test masses within a space craft is taken to be 60°, and the modulation is only allowed in the sensitive axis direction. The separation of the test masses

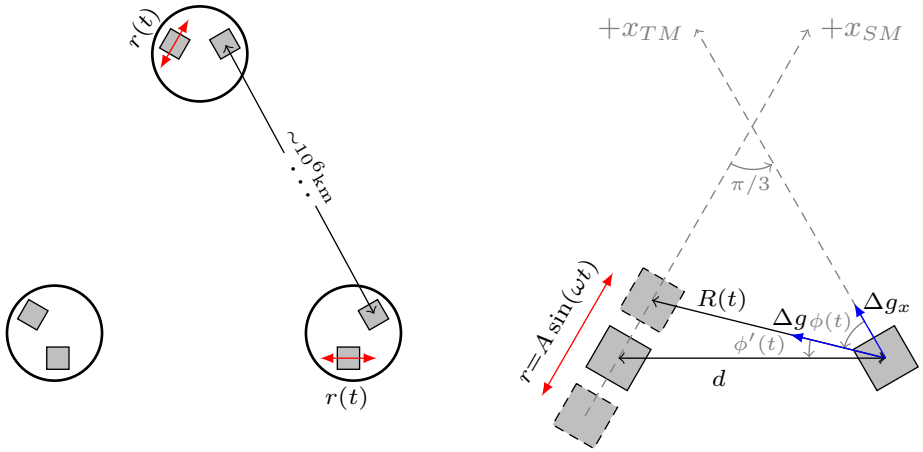

Figure 5.5: Cartoon of a simple modulation experiment to measure G on a LISA-like interferometer to demonstrate the increase in performance when measuring in drag free. A sinusoidal movement $r(t) = a\sin(\omega t)$ (red arrows) of two source masses in two space crafts can double the signal Δg_x measured by the measurement arm. The variable distance between the source mass and adjacent test mass within a single space craft, denoted by $R(t)$, can be used with the variable angle $\phi(t)$ to project the change in acceleration Δg into the x axis.

in their neutral positions in their housings is defined as d, and modulation of the neighbouring source mass in a space craft is given by $r = r(t)$. Putting these together, the variable angle subtended by the line between the test masses from the sensitive axis is

$$\begin{aligned}\phi(t) &= \frac{\pi}{3} - \phi'(t) \\ &= \frac{\pi}{3} - \tan^{-1}\left(\frac{r}{2d - \sqrt{3}r}\right)\end{aligned} \tag{5.30}$$

The variable shortest distance between the two test masses is then defined by

$$R(t) = ((r+d)^2 - (2+\sqrt{3})rd)^{1/2} \tag{5.31}$$

These can be used to calculate the relative acceleration between the two sensitive test masses, due to the in phase motion of the two source masses

$$\Delta g_x = 2\left(\frac{Gm\cos(\phi(t))}{R^2(t)}\right) \tag{5.32}$$

A probable outcome for LISA has a test mass separation of around $40-50$ cm, and a requirement

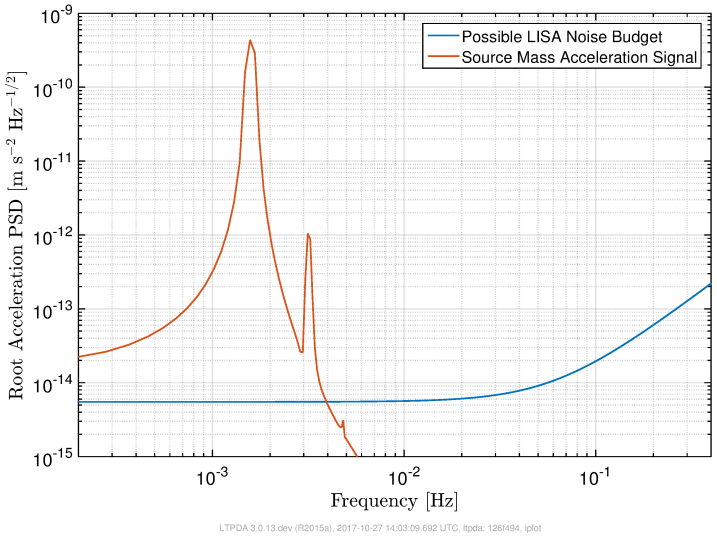

Figure 5.6: Example signal (red) for a large modulation experiment in drag free. The sensitivity used (blue) is based on the current best estimate.

sensitivity of around $5 \times 10^{-15}\,\mathrm{ms}^{-2}\mathrm{Hz}^{-1/2}$ in the millihertz region. For comparison, a toy model for a sinusoidal signal with amplitude 1 mm, and test mass separation of 40 cm gives a relative change in acceleration in the sensitive axis of $\Delta g_x \approx 1.1 \times 10^{-11}\,\mathrm{ms}^{-2}$.

Figure 5.6 shows the potential signal in frequency space for the toy example along with a possible sensitivity curve for LISA. Using a one-dimensional information matrix [131] to look at the error on a measurement of G through a grid in parameter space defined by $0.3\,\mathrm{m} \leq d \leq 0.6\,\mathrm{m}$ and $1 \times 10^{-4} \leq A \leq 1.5 \times 10^{-3}$, where A is the amplitude of the sinusoidal modulation $r(t) = A\sin(\omega_0 t)$, it is possible to extract the relative error on G using an integral over all frequencies f

$$\frac{\delta G}{G} = 2\int_0^\infty |\frac{\Delta\tilde{g}_x}{G^2}|^2 df \tag{5.33}$$

where $\Delta\tilde{g}_x$ is the Fourier transform of $2\Delta g_x$, which accounts for a doubling of the change in acceleration due to a source mass at either end of the measurement arm.

The results of the scan are shown in Figure 5.7. A highlighted point shows the relative error of 7×10^{-4} for a realization of an experiment similar to the toy model. Note the strong dependence on source mass test mass separation, illustrating the need to optimize this in future experiments.

Although both the Pathfinder and theoretical drag free measurements are not in the realm of the most competitive measurements to date, where relative errors can reach as low as parts in 10^5, there exists some inconsistency in these measurements with a scatter around parts in

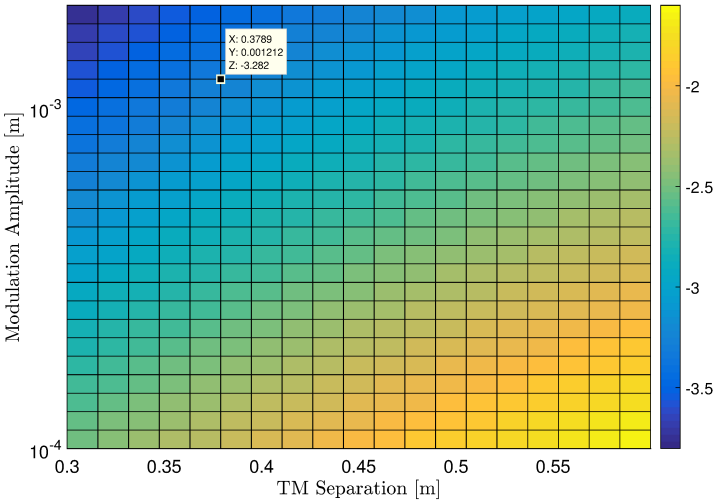

Figure 5.7: Possible relative errors of G using a simple modulation experiment on a LISA-like interferometer. Colour indicates $\log(\delta G/G)$. The highlighted point shows the example signal in Figure 5.6.

$10^4 - 10^3$. More importantly, note the change in relative error when moving from a measurement of DC acceleration to a drag free measurement of relative acceleration. The example here of a simple modulation experiment also shows that, with some fine tuning of the method and layout, it may be possible to access much more competitive measurements with future gradiometers.

5.5 Putting the Results into Context

Now that the Pathfinder mission has come to an end, it is possible to revisit the NOMAD plot with the end sensitivity from the nominal mission. It is also possible to take the example drag free measurement of the gravitational constant and compare it with the result from Pathfinder in the context of two example theories.

5.5.1 Revisiting the NOMAD plot

Given the final Pathfinder sensitivity shown in Figure 1.7 and detailed in the February 2018 results article [14], it is possible to add an additional band to the NOMAD plot according to the Pathfinder 2017 data. The method is outlined in a proposal document from 2017 [110], where the Pathfinder band had been updated using the June 2016 performance [13].

The calculation assumes the space craft is travelling at 1.5 kms^{-1} through the saddle point, and that the lateral gravitational gradient is $a^{'} = 2.3 \times 10^{-11}$ s^{-2}. The Sun facing solar array fixes the space craft orientation so that the measurement of Δg_x samples the lateral gradient only. The integrated time t_{int} in each acceleration band can be estimated from its velocity and the extent of the saddle point region. According to these approximations, it would spend 10200 s between 10^{-4} and 10^{-5} ms^{-2}, 1020 s between 10^{-5} and 10^{-6} ms^{-2}, 102 s between 10^{-6} and 10^{-7} ms^{-2}, and 30 s between 10^{-7} and 3×10^{-8} ms^{-2}. Accelerations below this limit are restricted by the the precision of the trajectory through the saddle point.

Estimating the Pathfinder sensitivity at frequencies equal to the inverse integration time, this gives the noise of the measurement $\sigma_{gg} = S_{gg}(1/\mathrm{t}_{int})$, where S_{gg} is the reported sensitivity curve. Then, using the test mass separation of $d = 0.367$ m, the residual δa/a is given by

$$\frac{\delta a}{a} = \frac{\sigma_{gg}}{a^{'} d} = \frac{S_{gg}(1/t_{int})}{a^{'} d\sqrt{t_{int}}} \tag{5.34}$$

Repeating this for each acceleration bin, the new band can be inserted into the plot as shown in Figure 5.8.

The lowest acceleration reached is determined by the miss distance to the saddle point; closer approaches to the saddle point means closer approaches to zero acceleration. Given this, the Pathfinder bands are not going to extend to accelerations occupied by systems like galactic rotation curves as trajectories are unlikely to pass through bands lower than 3×10^{-8} ms^{-2}. However, a substantial reduction in the Pathfinder residuals can clearly be seen, which provides a more stringent test on accelerations that otherwise are not well constrained.

The importance of testing the gap between solar system scales and galactic scales is paramount to understanding where current models for gravity begin to fail. Although many models place the characteristic scale beyond that reachable by a NOMAD mission, it would have provided further tests of the inverse square law in interim accelerations.

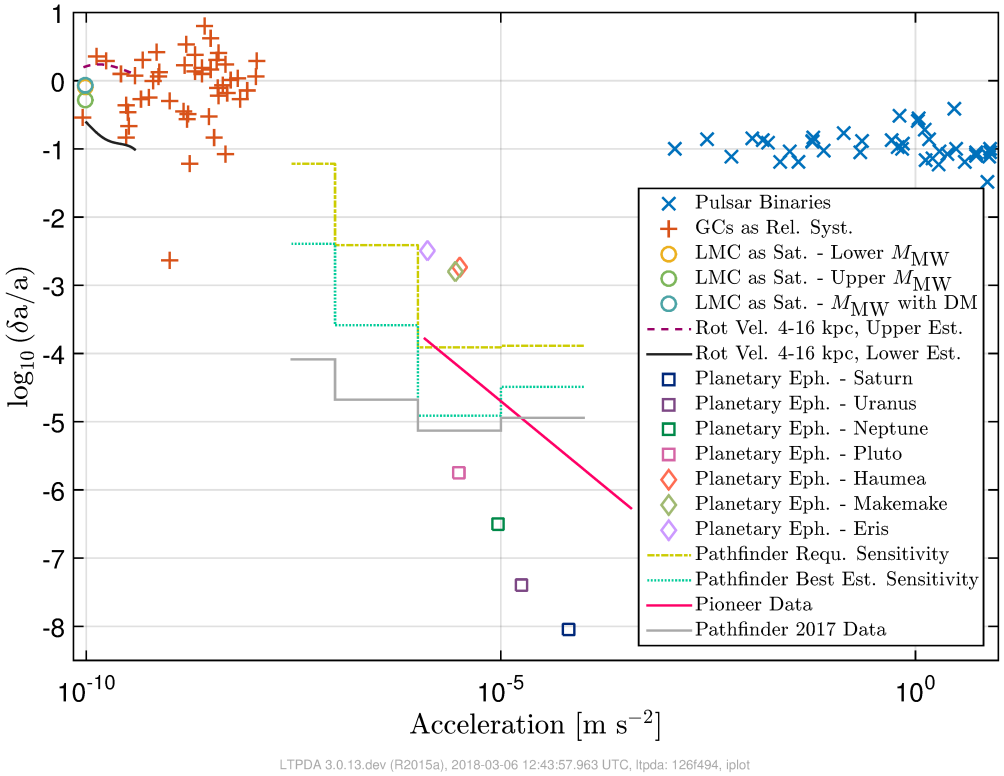

Figure 5.8: Same as Figure 5.4, but with an added Pathfinder band using the February 2018 reported sensitivity [14].

5.5.2 Applying Big G Measurements to Yukawa Gravity

This modification to the inverse square law uses an exponential term to subtly adjust the Newtonian potential, suggesting an infinite order polynomial perturbation. The use of a characteristic length, λ, dilutes the additional terms until a particular scale is reached.

Such a screening mechanism is one possibility to consider when coupling an additional massive particle to the stress energy tensor. Such theories aim to provide a dark matter candidate, for example in the case of spin-0 massive mesons coupling via higher order curvature terms in the Hilbert action [38], or five dimensional gravity [103].

In the low energy limit, the modification to the Newtonian potential used here is given by

$$V_Y = V_N(1 + \alpha e^{-r/\lambda}) \tag{5.35}$$

where α is the strength of the additional term and λ is the characteristic length scale. In the case of five dimensional gravity, the correction would be a factor $1 + \lambda/r$, which to leading order is identical to the correction above. The strength parameter can be further decomposed into a function of the baryon and lepton number [25], however the TMs on pathfinder are designed to be identical, and the case where lepton number is excluded only is assumed here. The modified potential can be used to derive the relative error in a measurement of G using the Pathfinder method and the proposed modulation experiment for LISA, in terms of the parameters describing the theory.

In the case of the Pathfinder experiment, the extreme positions of the source mass modulation relative to the test mass are denoted by x_+ and x_-. Then, relabelling Newton's gravitational constant by G_N, the acceleration on the test mass due to the position of the source mass is given by $a^Y_\pm$ and $a^N_\pm$ for the Yukawa and Newtonian cases respectively, where

$$a^Y_\pm = -\frac{G_N m}{x^2_\pm}\left(1 + \left(1 + \frac{x_\pm}{\lambda}\right)\alpha e^{-x_\pm/\lambda}\right) \qquad a^N_\pm = -\frac{G_N m}{x^2_\pm} \tag{5.36}$$

and m is the mass of the source mass.

Then, the difference in acceleration between these two positions for the Newtonian case is

$$\delta a^N = a^N_+ - a^N_- = -\frac{G_N m(x^2_+ - x^2_-)}{x^2_+ x^2_-} \tag{5.37}$$

and for the Yukawa case is

$$\delta a^Y = a^Y_+ - a^Y_- = \delta a^N - a^N_+\left(1 + \frac{x_+}{\lambda}\right)\alpha e^{-x_+/\lambda} + a^N_-\left(1 + \frac{x_-}{\lambda}\right)\alpha e^{-x_-/\lambda} \tag{5.38}$$

Then noting that the two extreme positions of the source mass are the same but in opposite directions in the x-axis from the central position, the relation can be simplified using

$$x_\pm = d \pm \delta d \qquad G_N = \frac{-\delta a^N x^2_+ x^2_-}{m(x^2_+ - x^2_-)} \qquad G_Y = \frac{-\delta a^Y x^2_+ x^2_-}{m(x^2_+ - x^2_-)} \tag{5.39}$$

where G_Y is what would be measured given a Yukawa like perturbation. The fractional error in the measured and predicted constant is then

$$\begin{aligned}\zeta_{LPF}(\lambda,\alpha) &= \frac{G_Y - G_N}{G_N} \\ &= \frac{\alpha e^{-d/\lambda}}{2d\delta d} \\ &\left[\left(d^2\left(1+\frac{d}{\lambda}\right)+(\delta d)^2\left(1-\frac{\delta d}{\lambda}\right)\right)\sinh\left(\delta d/\lambda\right)+\left(d\delta d\left(2+\frac{d}{\lambda}\right)-\frac{\delta d}{\lambda}(\delta d)^2\right)\cosh\left(\delta d/\lambda\right)\right]\end{aligned} \tag{5.40}$$

where the fractional error of the measurement is used instead of the difference between the CODATA and measured value, as this gives the most conservative estimate for the limit.

Now considering the drag free modulation experiment, the modification uses the distance between the source mass and test mass. Using the notation from before, this is

$$\begin{aligned}\zeta_{DF}(\lambda,\alpha) &= \frac{G_Y - G_N}{G_N} \\ &= \frac{\Delta g_x^Y - \Delta g_x^N}{\Delta g_x^N} \\ &= \alpha\left(\frac{R|_{r=+A}}{\lambda}e^{-R|_{r=+A}/\lambda}\right)\end{aligned} \tag{5.41}$$

where $R(t) = ((r+d)^2 - (2+\sqrt{3})rd)^{1/2}$ and $r = A\sin(\omega t)$.

Using $\zeta_{LPF} = 0.07$ and $\zeta_{DF} \approx 10^{-3}$ as the approximate errors on G, exclusion limits can be drawn in (λ, α) parameter space as shown in Figure 5.9.

Now comparing to the constraints on this theory around these length scales, it can be seen that the simple drag free experiment exclusion limits approach those in place by laboratory experiments. Comparing the results from the Pathfinder measurement of G, the motivation for measuring G using drag free interferometry becomes clear, as even a simple modulation experiment can improve the results of the Pathfinder measurement. Furthermore, this emphasizes the cost of not being able to source a signal using a mass outside of the measurement system.

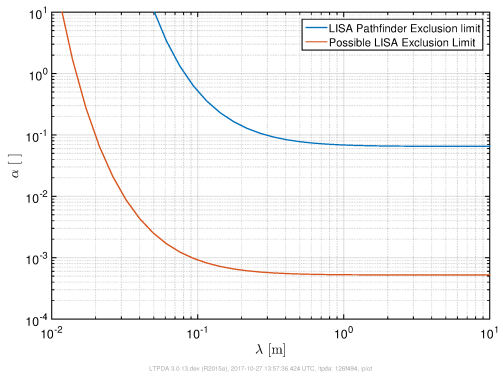

(a) Exclusion limits on Yukawa parameter space by LISA Pathfinder (blue) and an example measurement in drag free (red).

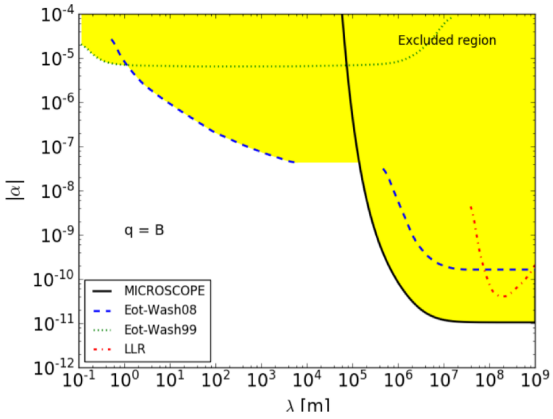

(b) Current solar system exclusion limits on Yukawa parameter space [25].

Figure 5.9: Comparison of the 1σ exclusion limit set by Pathfinder with the measurement of G, a potential 1σ exclusion limit by a drag free modulation experiment with a LISA-like interferometer, and current constraints in the same region of parameter space. Solar system tests include Lunar Laser Ranging (LLR), MICROSCOPE tests of the equivalence principle and Eot-Wash group results.

5.5.3 Applying Big G Measurements to Chameleons

This novel theory suggested that the gravitational force is weak relative to other forces due to shielding by the local density of matter. As such, all laboratory measurements would measure a weak force due to the Earth's density, but bodies far the Earth would experience very different dynamics. Originally this theory predicted an effective big G in space double the value on Earth [81], but more recently it has been developed to provide a number of shielding mechanisms for other theories of modified gravity.

In particular, it can be shown that so called $f(R)$ theories of gravity, where higher orders of the curvature scalar R are included in the action, can be rewritten as GR with an additional scalar field [108]. This kind of theory relies on the diversity of screening mechanisms to survive existing tests of relativity. For a detailed review of many flavours of chameleon shielding, along with the corresponding current constraints, see Burrage & Sakstein [34].

Since the Pathfinder measurement did not observe any change in G from ground measurements, it is possible to construct an exclusion limit on this theory by requiring that the space craft is fully shielded from an interplanetary stable solution for the chameleon, described by a

scalar field ϕ. Using the results in Khoury *et al.* [81] for the predicted change in gravitational constant, with the convention of Burrage & Sakstein [34] for a more modern approach to the parametrization, a conservative, upper limit on the length scale for this modification is given by a change in big G equal to the 1σ error in the Pathfinder measurement. This can then be used with the effective coupling constant, defined as

$$\beta_{eff} = 3\beta\frac{\Delta R_{SC}}{R_{SC}} \tag{5.42}$$

where β is the coupling of the theory, and defined as M_c/M_{pl}, where M_c is the mass scale for coupling and M_{pl} is the plank mass. In the original work by Khoury *et al.*, β was assumed to be order 1, giving a perturbation to the gravitational constant at around 100%. R_{SC} is the dimension of the space craft, and ΔR_{SC} defines a 'thin shell' through which the chameleon force acts. In this shell region, the field changes between the solution for the chameleon inside and outside of the space craft. As long as this shell is 'thin' the forces of gravity will match what is observed on Earth.

Khoury *et al.* found that

$$\frac{\Delta R_{SC}}{R_{SC}} = \frac{\phi_a - \phi_{SC}}{6\beta M_{Pl}\Phi_{SC}} \tag{5.43}$$

where ϕ_a is the value of the chameleon field in interplanetary space, ϕ_{SC} is the value of the field inside the space craft, and $\Phi_{SC} = G_N M_{SC}/R_{SC}^2$ is the Newtonian potential of the space craft. Using the definition of the field inside and outside as the value of the field that minimizes the effective potential

$$V_{eff} = \Lambda^{4+n}/\phi^n + \frac{\beta}{M_{Pl}}\rho e^{\beta\phi/M_{Pl}} \tag{5.44}$$

it is possible to link the measurement of G with the characteristic energy scale Λ through the local density of gas at 1AU. Denoted by ρ, this residual gas density acts as a weak shield for local Chameleons, and therefore should be accounted for when deriving the exclusion limit.

Taking the derivative of equation 5.44 and using a general potential with index n, where n is

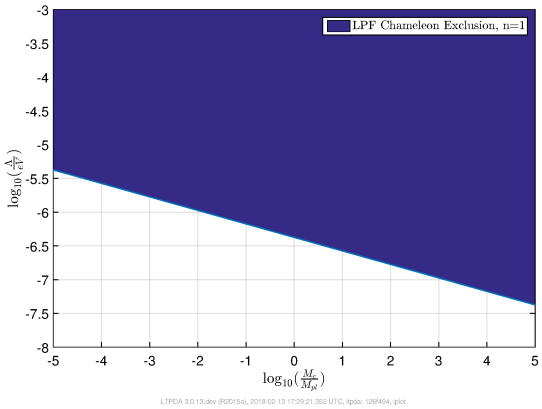

(a) LPF G measurement 1σ exclusion limits as applied to Chameleon theory with $n = 1$.

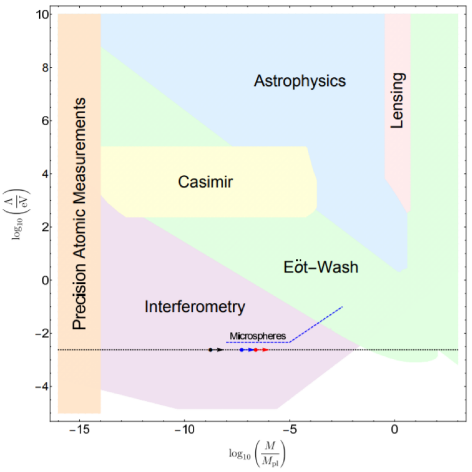

(b) A summary plot of current constraints on Chameleon theories with $n = 1$.

Figure 5.10: Comparison of the LPF G measurement with current constraints on Chameleon theories with $n = 1$. Each experiment is outlined by Burrage & Sakstein [34]. The dotted line denotes current predictions of dark energy in the universe.

any negative odd integer or any positive integer,

$$\Lambda^{4+n} = \frac{n\beta\rho}{M_{Pl}}\phi^{n+1}e^{\beta\phi/M_{Pl}} \tag{5.45}$$

Assuming that all of the potential deviation from Newtonian physics can hide within the 1σ error of G as measured by Pathfinder, then assume that the density difference between the outside and inside of the space craft are stark enough to approximate $\phi_a - \phi_{TM} \approx \phi_a$ only, then

$$\begin{aligned}\zeta = \frac{\delta G}{G} \geq 2\beta_{eff}^2 = 18\beta^2\left(\frac{\Delta R_{TM}}{R_{TM}}\right)^2 \\ \zeta \geq 18\beta^2\left(\frac{\phi_a}{6\beta M_{Pl}\Phi_{TM}}\right)^2 \\ \phi_a \leq \frac{G_N m_{TM} M_{Pl}}{R_{TM}}\sqrt{2\zeta}\end{aligned} \tag{5.46}$$

Implementing this in equation 5.45, the upper limit on the chameleon energy scale is

$$\Lambda^{4+n} \leq \frac{n\rho}{M_c}\left(\sqrt{2\zeta}M_{pl}\Phi_{TM}\right)^{n+1} e^{\sqrt{2\zeta}\Phi_{TM}M_{pl}/M_c} \tag{5.47}$$

Putting in the values for the space craft properties, $\zeta = 0.07$, and assuming an interplanetary

density of around $\rho_a \approx 10$ protons cm^{-3} at 1AU, the resulting exclusion limit for the special case $n = 1$ can be shown in Figure 5.10a. This exclusion limit is equivalent to the parameter values required to ensure the space craft is adequately shielded so that the TMs do not measure a departure from GR. Compared with the value of $m_G \leq 10 - 10^4$AU from Khoury *et al.* [81] using laboratory measurements and the earth's atmosphere, this places a much more strict limit on the theory.

A more recent review of Chameleons and their current constraints as of 2017 is given by Burrage & Sakstein [34]. Figure 5.10b shows the corresponding current constraints for this particular parameter space, highlighting that a measurement of Newton's constant in space is a powerful tool to explore theories of modified gravity that include screening mechanisms.

5.6 Discussion

Although the saddle point mission did not go ahead, there could have been a reasonable contribution from Pathfinder to fill a gap between relatively well modeled and not so well understood systems. However, *a priori*, the working sensitivity of the instrument was not known, making the motivation for the mission a question of risk for time with the space craft and fuel allowance.

The better than expected nominal performance on Pathfinder saw a deepening of the potential exclusion limit Pathfinder could have place were the NOMAD mission to have flown. The lowest acceleration reached by this limit, however, depends heavily on the miss distance to the saddle point. Closer approaches will etch the Pathfinder bands closer to the limits set by rotation curves of galaxies, globular clusters, the LMC as a satellite, and, most importantly, the set transition acceleration of 10^{-10} ms^{-2}. However, the more stringent tests of the interim accelerations would verify GR in a region that otherwise is poorly understood. This is important for understanding how the dynamics at these two scales approach each other.

Turning to a more model independent approach to exploring fundamental physics with Pathfinder, the Big G experiment proved difficult for a number of reasons. It was shown that even a simpler modulation experiment by a LISA-like interferometer could provide a near competitive mea-

surement, highlighting that one of the primary difficulties of the Big G experiment was working outside of the drag free system.

The next limiting factor for any future gravity gradiometer wishing to make a similar measurement is the knowledge in the absolute distance between a source mass and measurement mass, which was known at parts in 10^4 for Pathfinder. This would need to be calibrated both on ground and in flight to lift the underlying limit on the measurement and adjust for a drift as the TM reaches the electrostatic equilibrium position. More importantly, using a scan through a two parameter space it was shown that reducing the distance between source mass and test mass would improve the overall measurement substantially.

Although the example drag free measurement used a layout defined by the LISA experiment, the derivation is similar for a general interferometer. In fact, it is possible to apply the derivation here to the layout of SMART-2, an early version of the Pathfinder experiment where two pairs of test masses were proposed instead of one. In essence, the results apply to any experiment with drag free interferometry and source mass independent of the measurement axis.

Two example theories were used with the Pathfinder measurement and the example modulation experiment to illustrate the improvements on exclusion limits possible when in drag free, and the motivations for pursuing these measurements. In the case of Yukawa gravity, a simple drag free modulation experiment provided an improvement in exclusion limit proportional to the improved relative error of the gravitational constant measurement. In the case of Chameleons, the limit placed by Pathfinder was close to current constraints, emphasizing that measuring this constant in space is a powerful tool to explore the parameter spaces of theories with screening mechanisms.

This chapter briefly discusses one aspect of the role gravity gradiometers could play in addressing some of the problems faced in fundamental physics. With the better than expected performance of Pathfinder it is hoped these experiments could begin to help shape the theoretical landscape, providing new exclusion limits in the foreseeable future.

Chapter 6

Conclusion

In the next few decades, the field of Gravitational Wave Astronomy will see several ground-breaking experiments approach operations. LISA Pathfinder, a proof of concept mission to test the technology available for a large scale interferometer in space, has successfully surpassed its sensitivity requirements and those set for LISA. This thesis presents some of the contributions made toward the experiment relating to space weather at the first Lagrange point and fundamental physics.

A model was outlined for the radiation monitor on Pathfinder. It assumed a Gaussian electronic noise with parameters fitted using weekly test pulses. Three different plausible models for the threshold distributions were tested using two sets of calibration data. Of the three models, a single Gaussian with mean μ_T and standard deviation σ_T was found to reproduce the data well, best re-produce the expected singles count to coincident count ratio behaviour and even suggest a global model. However, the best fit threshold parameter values suggested the assumptions in the initial fit for ϕ were flawed.

Also tested was a double Gaussian model which included a single standard deviation σ_T determined by a technical report and two free parameters, μ_{Front} and μ_{Back}, denoting the mean offset from the nominal threshold in the front and back diodes. This did not fair as well as the single Gaussian model with no global parameter values available. The final model tested was a single Gamma distribution for both thresholds described by parameters $\kappa\theta$ and θ for the mean

and shape. This was the worse of the three distributions, with no global model available and the highest tension between predicted and measured spectra. Furthermore, when the front and back diode thresholds were set at different values, the results suggested that there was more happening than was captured by the model.

The fits performed suggested that a single Gaussian distribution best described the threshold characteristics for the nominal data, but the model required further scrutiny to fully describe the monitor's full range of energies. Future designs for radiation monitors on LISA are advised to more extensively test the individual shapes of the thresholds using an oscilloscope, especially considering the cases where the deposited energy is close to the nominal threshold. This will improve the quality of analyses with this data as the vast majority of deposited energy in the Pathfinder RM resides in the main peak just a few bins above the nominal threshold.

In order to remove the redundancy between the initial fit for ϕ and the threshold parameters, the single Gaussian model was adopted but the parameters μ_T and σ_T were set to the values determined for the electronics noise. The model was then applied to daily coincident spectra through the Pathfinder mission to extract estimates for solar attenuation of cosmic rays. The daily estimates recovered a variation at integer fractions of the 27 day solar rotation period, indicating a link to heliospheric current sheet crossings. Ground work was made to project test mass charging to the LISA mission by correlating the ϕ estimates with charging rate measurements at several configurations of TM potential and actuation voltage.

A measurement of the gravitational constant in space was made by Pathfinder. The value was found to be $6.93 \times 10^{-11} \pm 0.36 \times 10^{-11} \mathrm{m^3 kg^{-1} s^{-2}}$, although further refinement of the analysis is expected. The difficulties encountered so far have highlighted obstacles to be addressed by future gradiometers wishing to improve on this value.

A toy model of a simple modulation experiment with a LISA-like interferometer showed that a measurement using drag-free relative acceleration greatly improves the result. It also suggested that the most efficient way to decrease the relative uncertainty is to minimize the distance between the test mass(es) and source mass. Optimizing this in layouts of future gradiometers is essential in order to reach a competitive measurement of the gravitational constant.

The motivation for a saddle-point fly-by mission on MOND was also developed. It was found that Pathfinder could bridge the gap and test accelerations between well modelled solar system dynamics and relatively not-well understood dynamics above this scale. The impact of this kind of measurement depends on the miss distance between the satellite and the saddle point, which determines the lowest acceleration reached.

The success of Pathfinder has demonstrated that space based interferometers are well within the scope of current technology, and as detections by ground based experiments mount it is clear that there are numerous sources in the universe waiting to be heard. As Gravitational Wave Astronomy continues to expand, the addition of lower frequency detectors will broaden the field and enrich the knowledge gained from the gravitational universe.

Bibliography

[1] LISA, Laser Interferometer Space Antenna. `https://www.elisascience.org/files/publications/LISA_L3_20170120.pdf`, Jan. 2017. Accessed: 20-02-2018.

[2] M. G. Aartsen et al. Probing the origin of cosmic rays with extremely high energy neutrinos using the IceCube Observatory. *Physical Review D*, 88(11):112008, Dec. 2013.

[3] B. P. Abbott et al. Binary Black Hole Mergers in the First Advanced LIGO Observing Run. *Physical Review X*, 6:041015, Oct 2016.

[4] B. P. Abbott et al. GW151226: Observation of Gravitational Waves from a 22-Solar-Mass Binary Black Hole Coalescence. *Physical Review Letters*, 116:241103, Jun 2016.

[5] B. P. Abbott et al. Observation of gravitational waves from a binary black hole merger. *Physical Review Letters*, 116:061102, Feb 2016.

[6] B. P. Abbott et al. GW170104: Observation of a 50-Solar-Mass Binary Black Hole Coalescence at Redshift 0.2. *Physical Review Letters*, 118:221101, Jun 2017.

[7] B. P. Abbott et al. GW170608: Observation of a 19 Solar-mass Binary Black Hole Coalescence. *The Astrophysical Journal Letters*, 851(2):L35, 2017.

[8] B. P. Abbott et al. GW170814: A Three-Detector Observation of Gravitational Waves from a Binary Black Hole Coalescence. *Physical Review Letters*, 119:141101, Oct 2017.

[9] B. P. Abbott et al. GW170817: Observation of Gravitational Waves from a Binary Neutron Star Inspiral. *Physical Review Letters*, 119:161101, Oct 2017.

[10] M. Ando and TAMA Collaboration. Current status of TAMA. *Classical and Quantum Gravity*, 19:1409–1419, Apr. 2002.

[11] F. Antonucci et al. Interaction between Stray Electrostatic Fields and a Charged Free-Falling Test Mass. *Physical Review Letters*, 108(18):181101, May 2012.

[12] H. M. Araújo et al. Detailed calculation of test-mass charging in the LISA mission. *Astroparticle Physics*, 22:451–469, Jan. 2005.

[13] M. Armano et al. Sub-Femto-g Free Fall for Space-Based Gravitational Wave Observatories: LISA Pathfinder Results. *Physical Review Letters*, 116:231101, Jun 2016.

[14] M. Armano et al. Beyond the Required LISA Free-Fall Performance: New LISA Pathfinder Results down to 20μHz. *Physical Review Letters*, 120:061101, Feb 2018.

[15] M. Armano et al. Measuring the Galactic Cosmic Ray flux with the LISA Pathfinder radiation monitor. *Astroparticle Physics*, 98:28–37, Feb. 2018.

[16] P. Astone et al. Analysis of 3 years of data from the gravitational wave detectors EXPLORER and NAUTILUS. *Physical Review D*, 87(8):082002, Apr. 2013.

[17] S. Babak, J. R. Gair, and R. H. Cole. Extreme mass ratio inspirals: perspectives for their detection. *ArXiv e-prints*. arXiv:1411.5253, Nov 2014.

[18] S. Babak et al. Science with the space-based interferometer lisa. v. extreme mass-ratio inspirals. *Physical Review D*, 95:103012, May 2017.

[19] J. T. Baird, D. Hollington, T. J. Sumner, and P. J. Wass. *A fundamental test of gravity with LISA pathfinder*, pages 3203–3209. WORLD SCIENTIFIC, Dec. 2017.

[20] J. Bekenstein and J. Magueijo. Modified Newtonian dynamics habitats within the solar system. *Physical Review D*, 73(10):103513, May 2006.

[21] K. Bekki. On the Interpretation of Recent Proper Motion Data for the Large Magellanic Cloud. *The Astrophysical Journal Letters*, 730:L2, Mar. 2011.

[22] A. R. Bell. The acceleration of cosmic rays in shock fronts. I. *Monthly Notices of the Royal Astronomical Society*, 182:147–156, Jan. 1978.

[23] A. R. Bell. The acceleration of cosmic rays in shock fronts. II. *Monthly Notices of the Royal Astronomical Society*, 182:443–455, Feb. 1978.

[24] M. J. Benacquista. Relativistic binaries in globular clusters. *Living Reviews in Relativity*, 9(2), 2006.

[25] J. Bergé et al. MICROSCOPE first constraints on the violation of the weak equivalence principle by a light scalar dilaton. *ArXiv e-prints*. arXiv:1712.00483, Dec 2017.

[26] J. Bieber. Perpendicular Diffusion of Charged Test Particles in Magnetostatic Slab Turbulence. *International Cosmic Ray Conference*, 7:61, 1999.

[27] D. Bisschoff and M. S. Potgieter. New local interstellar spectra for protons, helium and carbon derived from PAMELA and Voyager 1 observations. *Astrophysics & Space Science*, 361:48, Feb. 2016.

[28] R. D. Blum. Figure rotation and the mass of the galactic bulge. *The Astrophysical Journal*, 444:L89–L91, May 1995.

[29] C. Boatella. Lisa pathfinder radiation monitor prototype design s2-ifae-ddd-3002. Technical report, Institut de Ciències de l'Espai, Oct. 2006. Version 2.1.

[30] M. Bouhmadi-López, R. Maartens, and D. Wands. Gravitational waves from brane-world inflation with induced gravity. *Physical Review D*, 70(12):123519, Dec. 2004.

[31] C. H. Brans. The roots of scalar-tensor theory: an approximate history. *ArXiv General Relativity and Quantum Cosmology e-prints*, June 2005.

[32] P. Brax et al. Chameleons with field-dependent couplings. *Physical Review D*, 82(8):083503, Oct. 2010.

[33] R. A. Burger, M. S. Potgieter, and B. Heber. Rigidity dependence of cosmic ray proton latitudinal gradients measured by the Ulysses spacecraft: Implications for the diffusion tensor. *Journal for Geophysical Research*, 105:27447–27456, Dec. 2000.

[34] C. Burrage and J. Sakstein. Tests of Chameleon Gravity. *ArXiv e-prints*. arXiv:1709.09071, Sep 2017.

[35] B. Caron et al. The Virgo interferometer. *Classical and Quantum Gravity*, 14:1461–1469, June 1997.

[36] S. Carroll. Lecture notes on general relativity. Enrico Fermi Institute, University of Chicago, Dec. 1997. `https://ned.ipac.caltech.edu/level5/March01/Carroll3/Carroll_contents.html`. Accessed: 2017-12-02.

[37] H. Cavendish. Experiments to determine the density of the earth. *Philosophical Transactions of the Royal Society of London*, 88:469–526, Jan 1798.

[38] J. L. Cervantes-Cota, M. A. Rodríguez-Meza, and D. Nuñez. Flat rotation curves using scalar-tensor theories. In *Journal of Physics Conference Series*, volume 91 of *Journal of Physics Conference Series*, page 012007, Nov. 2007.

[39] S. Chandrasekhar. The maximum mass of ideal white dwarfs. *The Astrophysical Journal*, 74:81–82, Aug. 1931.

[40] P. Chatterjee et al. Full-sphere simulations of a circulation-dominated solar dynamo: Exploring the parity issue. *Astronomy & Astrophysics*, 427:1019–1030, Dec. 2004.

[41] G. M. Clemence. The Relativity Effect in Planetary Motions. *Reviews of Modern Physics*, 19:361–364, Oct. 1947.

[42] F. Combes. The Square Kilometer Array: cosmology, pulsars and other physics with the SKA. *Journal of Instrumentation*, 10:C09001, Sept. 2015.

[43] K. Danzmann. LISA and LISA Pathfinder: laser interferometry in space. In *Society of Photo-Optical Instrumentation Engineers (SPIE) Conference Series*, volume 10566 of *Society of Photo-Optical Instrumentation Engineers (SPIE) Conference Series*, page 1056610, Nov. 2017.

[44] A. de Rújula, H. Georgi, and S. L. Glashow. Hadron masses in a gauge theory. *Physical Review D*, 12:147–162, July 1975.

[45] G. de Vaucouleurs and W. D. Pence. An outsider's view of the Galaxy - Photometric parameters, scale lengths, and absolute magnitudes of the spheroidal and disk components of our Galaxy. *The Astronomical Journal*, 83:1163–1173, Oct. 1978.

[46] M. Diaz-Aguilo et al. Estimation of the Magnetic Noise Contribution to LISA Pathfinder Differential Acceleration. In G. Auger, P. Binétruy, and E. Plagnol, editors, *9th LISA Symposium*, volume 467 of *Astronomical Society of the Pacific Conference Series*, page 257, Jan. 2013.

[47] F. W. Dyson, A. S. Eddington, and C. Davidson. A Determination of the Deflection of Light by the Sun's Gravitational Field, from Observations Made at the Total Eclipse of May 29, 1919. *Philosophical Transactions of the Royal Society of London Series A*, 220:291–333, 1920.

[48] A. Einstein. Die Feldgleichungen der Gravitation. *Sitzungsberichte der Königlich Preußischen Akademie der Wissenschaften (Berlin), Seite 844-847.*, 1915.

[49] A. Einstein. Die Grundlage der allgemeinen Relativitätstheorie. *Annalen der Physik*, 354:769–822, 1916.

[50] European Space Agency. Lisa pathfinder orbit. `https://www.elisascience.org/multimedia/image/lpforbit`. Accessed: 2015-07-23.

[51] European Space Agency. LISA technology package. `www.esa.int/spaceinimages/Images/2008/06/LISA_Technology_Package`. Accessed: 2015-03-15.

[52] C. W. F. Everitt et al. Gravity Probe B: Final Results of a Space Experiment to Test General Relativity. *Physical Review Letters*, 106(22):221101, June 2011.

[53] E. Fabacher et al. Multiple Sun-Earth Saddle Point flybys for LISA Pathfinder. *Advances in Space Research*, 52:105–116, July 2013.

[54] B. Famaey and S. S. McGaugh. Modified Newtonian Dynamics (MOND): Observational Phenomenology and Relativistic Extensions. *Living Reviews in Relativity*, 15:10, Sept. 2012.

[55] D. Finkelstein. Past-future asymmetry of the gravitational field of a point particle. *Physical Review*, 110:965–967, May 1958.

[56] B. Q. For et al. The Magellanic Stream and Debris Clouds. *The Astrophysical Journal Letters*, 792:43, Sept. 2014.

[57] P. C. C. Freire et al. The relativistic pulsar-white dwarf binary PSR J1738+0333 - II. The most stringent test of scalar-tensor gravity. *Monthly Notices of the Royal Astronomical Society*, 423:3328–3343, July 2012.

[58] A. Gelman and D. B. Rubin. A single series from the gibbs sampler provides a false sense of security. *Bayesian Statistics*, 4:625–631, 1992.

[59] J. Geweke et al. *Evaluating the accuracy of sampling-based approaches to the calculation of posterior moments*, volume 196. Federal Reserve Bank of Minneapolis, Research Department Minneapolis, MN, USA, 1991.

[60] F. Gibert et al. Thermo-elastic induced phase noise in the LISA Pathfinder spacecraft. *Classical & Quantum Gravity*, 32(4):045014, Feb. 2015.

[61] G. Gilmore and N. Reid. New light on faint stars. III - Galactic structure towards the South Pole and the Galactic thick disc. *Monthly Notices of the Royal Astronomical Society*, 202:1025–1047, Mar. 1983.

[62] S. L. Glashow. The renormalizability of vector meson interactions. *Nuclear Physics A*, 10:107–117, Feb. 1959.

[63] L. J. Gleeson and W. I. Axford. Solar Modulation of Galactic Cosmic Rays. *The Astrophysical Journal*, 154:1011, Dec. 1968.

[64] X. Gong et al. Descope of the ALIA mission. In *Journal of Physics Conference Series*, volume 610 of *Journal of Physics Conference Series*, page 012011, May 2015.

[65] C. Grimani et al. LISA Pathfinder test-mass charging during galactic cosmic-ray flux short-term variations. *Classical & Quantum Gravity*, 32(3):035001, Feb. 2015.

[66] G. M. H. J. Habets and J. R. W. Heintze. Empirical bolometric corrections for the main-sequence. *Astronomy & Astrophysics Supplement*, 46:193–237, Nov. 1981.

[67] W. Hajdas et al. Radiation environment along the INTEGRAL orbit measured with the IREM monitor. *Astronomy & Astrophysics*, 411:L43–L47, Nov. 2003.

[68] W. E. Harris. A Catalog of Parameters for Globular Clusters in the Milky Way: The Database. *The Astrophysical Journal*, 112:1487, 1996 (2010 Edition). *http://www.physics.mcmaster.ca/ harris/mwgc.dat*. Accessed 12 jun 2015.

[69] O. Heaviside. *Electromagnetic Theory*, volume 1. 1893.

[70] B. Heckel. Distortion of space from a gravitational wave. `https://www.learner.org/courses/physics/unit/text.html?unit=3&secNum=7`. Accessed: 2018-04-05.

[71] A. Hees et al. Combined Solar system and rotation curve constraints on MOND. *Monthly Notices of the Royal Astronomical Society*, 455:449–461, Jan. 2016.

[72] A. Hewish et al. Observation of a Rapidly Pulsating Radio Source. *Nature*, 217:709–713, Feb. 1968.

[73] G. Hobbs et al. The International Pulsar Timing Array project: using pulsars as a gravitational wave detector. *Classical and Quantum Gravity*, 27(8):084013, Apr. 2010.

[74] G. Indu and A. Subramaniam. H I kinematics of the Large Magellanic Cloud revisited: Evidence of possible infall and outflow. *Astronomy & Astrophysics*, 573:A136, Jan. 2015.

[75] B. Iyer. LIGO-India: expanding the international network of gravitational wave detectors. In *APS Meeting Abstracts*, page J13.001, Apr. 2015.

[76] S. Jabbari. Literature review on the formation of active regions. `http://people.kth.se/~sarahjab/publication/lit_review/notes.pdf`, 2013. Accessed: 2016-12-21.

[77] S. Jabbari. *Origin of Solar Surface Activity and Sunspots.*, volume 4 of *10*. Holmbergs, Malmö, 2016.

[78] W. R. Johnstone. List of pulsars in binary systems. `http://www.johnstonsarchive.net/relativity/binpulstable.html`, Mar. 2005. Accessed: 2015-06-05.

[79] M. Jordan. Lecture 7: Jeffreys priors and reference priors. Electrical Engineering and Computer Science, University of California, Berkeley, Feb. 2010. `https://people.eecs.berkeley.edu/~jordan/courses/260-spring10/lectures/lecture7.pdf`. Accessed: 2018-02-21.

[80] Y. C. Joshi and S. Joshi. Population I Cepheids and star formation history of the Large Magellanic Cloud. *New Astronomy*, 28:27–34, Apr. 2014.

[81] J. Khoury and A. Weltman. Chameleon Fields: Awaiting Surprises for Tests of Gravity in Space. *Physical Review Letters*, 93(17):171104, Oct. 2004.

[82] G. Kopp and G. Lawrence. The Total Irradiance Monitor (TIM): Instrument Design. *Solar Physics*, 230:91–109, Aug. 2005.

[83] M. Kramer and D. J. Champion. The European Pulsar Timing Array and the Large European Array for Pulsars. *Classical and Quantum Gravity*, 30(22):224009, Nov. 2013.

[84] M. D. Kruskal. Maximal Extension of Schwarzschild Metric. *Physical Review Journals Archive*, 119:1743–1745, Sept. 1960.

[85] LIGO Scientific Collaboration et al. Advanced LIGO. *Classical and Quantum Gravity*, 32(7):074001, Apr. 2015.

[86] J. Lilley. *Nuclear Physics, Principles and Applications*. John Wiley & Sons, 2001.

[87] H. Lück et al. The upgrade of GEO 600. In *Journal of Physics Conference Series*, volume 228 of *Journal of Physics Conference Series*, page 012012, May 2010.

[88] J. Luo et al. TianQin: a space-borne gravitational wave detector. *Classical and Quantum Gravity*, 33(3):035010, Feb. 2016.

[89] R. N. Manchester et al. VizieR Online Data Catalog: ATNF Pulsar Catalog (Manchester+, 2005). http://www.atnf.csiro.au/people/pulsar/psrcat/. *VizieR Online Data Catalog*, 7245:0, Aug. 2005.

[90] E. W. Maunder. The sun and sun-spots, 1820-1920. *Monthly Notices of the Royal Astronomical Society*, 82:534–543, June 1922.

[91] N. Metropolis et al. Equation of State Calculations by Fast Computing Machines. *Journal of Chemical Physics*, 21:1087–1092, June 1953.

[92] M. Milgrom. The MOND paradigm. *ArXiv e-prints*. arXiv:0801.3133, Jan 2008.

[93] M. Milgrom. A modification of the Newtonian dynamics as a possible alternative to the hidden mass hypothesis. *The Astrophysical Journal*, 270:365–370, July 1983.

[94] P. J. Mohr, D. B. Newell, and B. N. Taylor. Codata recommended values of the fundamental physical constants: 2014. *Reviews of Modern Physics*, 88:035009, Sept. 2016.

[95] C. J. Moore, R. H. Cole, and C. P. L. Berry. Gravitational-wave sensitivity curves. *Classical and Quantum Gravity*, 32(1):015014, Jan. 2015.

[96] I. Newton. *Philosophiae naturalis principia mathematica*. J. Societatis Regiae ac Typis J. Streater, 1687.

[97] E. N. Parker. The passage of energetic charged particles through interplanetary space. *Planetary and Space Science*, 13:9–49, Jan. 1965.

[98] J. D. H. Pilkington et al. Observations of some further Pulsed Radio Sources. *Nature*, 218:126–129, Apr. 1968.

[99] E. V. Pitjeva. High-Precision Ephemerides of Planets - EPM and Determination of Some Astronomical Constants. *Solar System Research*, 39:176–186, May 2005.

[100] E. V. Pitjeva. Updated IAA RAS planetary ephemerides-EPM2011 and their use in scientific research. *Solar System Research*, 47:386–402, Sept. 2013.

[101] H. Poincaré. Sur la dynamique de l' electron. *Note, l'Académie des Sciences*, 1:1504âĂŞ1508, 1905.

[102] M. Punturo, H. Lück, and M. Beker. A Third Generation Gravitational Wave Observatory: The Einstein Telescope. In M. Bassan, editor, *Advanced Interferometers and the*

Search for Gravitational Waves, volume 404 of *Astrophysics and Space Science Library*, page 333, 2014.

[103] L. Randall and R. Sundrum. An alternative to compactification. *Physical Review Letters*, 83:4690–4693, Dec 1999.

[104] A. G. Riess et al. Observational Evidence from Supernovae for an Accelerating Universe and a Cosmological Constant. *The Astronomical Journal*, 116:1009–1038, Sept. 1998.

[105] V. C. Rubin, N. Thonnard, and W. K. Ford, Jr. Extended rotation curves of high-luminosity spiral galaxies. IV - Systematic dynamical properties, SA through SC. *The Astrophysical Journal Letters*, 225:L107–L111, Nov. 1978.

[106] Y. Sakakibara et al. Progress on the cryogenic system for the KAGRA cryogenic interferometric gravitational wave telescope. *Classical and Quantum Gravity*, 31(22):224003, Nov. 2014.

[107] A. Salam and J. C. Ward. Weak and electromagnetic interactions. *Il Nuovo Cimento*, 11:568–577, Feb. 1959.

[108] T. P. Sotiriou. f(R) gravity and scalar tensor theory. *Classical and Quantum Gravity*, 23:5117–5128, Sept. 2006.

[109] T. Sumner and C. Trenkel. personal communication, May 2015.

[110] T. Sumner, C. Trenkel, and J. Baird. NOMAD (Newtonian or Modified Acceleration Dynamics). personal communication, May 2017.

[111] T. J. Sumner. Science with LISA Pathfinder. In G. Auger, P. Binétruy, and E. Plagnol, editors, *9th LISA Symposium*, volume 467 of *Astronomical Society of the Pacific Conference Series*, page 129, Jan. 2013.

[112] G. Szekeres. On the singularities of a Riemannian manifold. *Publicationes Mathematicae Debrecen 7, 285 (1960)*, 7, 1960.

[113] R. J. Tayler. *The Stars: their structure and evolution.* Cambridge University Press, Cambridge, 2 edition, 1994.

[114] J. H. Taylor and J. M. Weisberg. A new test of general relativity - Gravitational radiation and the binary pulsar PSR 1913+16. *The Astrophysical Journal*, 253:908–920, Feb. 1982.

[115] The LISA-Pathfinder Team. General design and interface requirements specification s2.asu.rs.2031. Gdir, EADS Astrium ltd., under ESA contract, Dec. 2005. Version 2.1.

[116] U. Tortermpun, D. Ruffolo, and J. W. Bieber. Galactic Cosmic-Ray Anistropy During the Forbush Decrease Starting 2013 April 13. *The Astrophysical Journal Letters*, 852:L26, Jan. 2018.

[117] P. Touboul et al. MICROSCOPE Mission: First Results of a Space Test of the Equivalence Principle. *Physical Review Letters*, 119(23):231101, Dec. 2017.

[118] C. Trenkel. LPF G Outline. Personal communication, Apr. 2016.

[119] C. Trenkel and D. Wealthy. Effect of LISA Pathfinder spacecraft self-gravity on anomalous gravitational signals near the Sun-Earth saddle point predicted by quasilinear MOND. *Physical Review D*, 90(8):084037, Oct. 2014.

[120] C. Trenkel et al. Testing MOND/TEVES with LISA Pathfinder. *ArXiv e-prints.* arXiv:1001.1303, Jan 2010.

[121] S. G. Turyshev et al. Support for Temporally Varying Behavior of the Pioneer Anomaly from the Extended Pioneer 10 and 11 Doppler Data Sets. *Physical Review Letters*, 107(8):081103, Aug. 2011.

[122] A. J. Tylka et al. Temporal Evolution in the Spectra of Gradual Solar Energetic Particle Events. *AIP Conference Proceedings*, 528:147–152, Mar. 2001.

[123] I. G. Usoskin, G. A. Bazilevskaya, and G. A. Kovaltsov. Solar modulation parameter for cosmic rays since 1936 reconstructed from ground-based neutron monitors and ionization chambers. *Journal of Geophysical Research (Space Physics)*, 116:A02104, Feb. 2011.

[124] I. G. Usoskin et al. A physical reconstruction of cosmic ray intensity since 1610. *Journal of Geophysical Research (Space Physics)*, 107:1374, Nov. 2002.

[125] A. Vecchio, E. D. Wickham, and I. R. Stevens. LISA observations of intermediate mass black hole binary systems. In J. Hough and G. H. Sanders, editors, *Gravitational Wave and Particle Astrophysics Detectors*, volume 5500 of *Society of Photo-Optical Instrumentation Engineers (SPIE) Conference Series*, pages 183–193, Sept. 2004.

[126] S. Vitale and LISA Pathfinder Team. The LISA Pathfinder Mission. In *AAS/High Energy Astrophysics Division*, volume 13 of *AAS/High Energy Astrophysics Division*, page 302.02, Apr. 2013.

[127] P. J. Wass et al. Test-mass charging simulations for the LISA Pathfinder mission. *Classical & Quantum Gravity*, 22:311, May 2005.

[128] J. Weber. Detection and Generation of Gravitational Waves. *Physical Review Journal Archive*, 117:306–313, Jan. 1960.

[129] S. Weinberg. A Model of Leptons. *Physical Review Letters*, 19:1264–1266, Nov. 1967.

[130] C. M. Will. The Confrontation between General Relativity and Experiment. *Living Reviews in Relativity*, 9:3, Mar. 2006.

[131] C. M. Will and N. Yunes. Testing alternative theories of gravity using LISA. *Classical & Quantum Gravity*, 21:4367–4381, Sept. 2004.

[132] K. Yagi and N. Seto. Detector configuration of DECIGO/BBO and identification of cosmological neutron-star binaries. *Physical Review D*, 83(4):044011, Feb. 2011.